Droplet Coalescence on Surfaces of Various Wettabilities

Percival Graham

A Thesis
In
The Department
Of
Mechanical and Industrial Engineering

Presented in Partial Fulfillment of the Requirements
for the Degree of Master of Applied Science (Mechanical Engineering)
At
Concordia University
Montreal, Quebec, Canada

August 2012

CONCORDIA UNIVERSITY

SCHOOL OF GRADUATE STUDIES

This is to certify that the Thesis prepared,

By: **Percival Graham**

Entitled: **"Droplet Coalescence on Surfaces of Various Wettabilities"**

and submitted in partial fulfillment of the requirements for the Degree of

Master of Applied Science (Mechanical Engineering)

complies with the regulations of this University and meets the accepted standards with respect to originality and quality.

Signed by the Final Examining Committee:

_____ Chair
Dr. H.D. Ng

_____ Examiner
Dr. L. Kadem

_____ Examiner
Dr. S. Li External
Building, Civil and Environmental Engineering

_____ Supervisor
Dr. A. Dolatabadi

Approved by: _____
Dr. S. Narayanswamy, MASc Program Director
Department of Mechanical and Industrial Engineering

_____
Dean Robin Drew
Faculty of Engineering & Computer Science

Date: _____

Abstract

Droplet Coalescence on Surfaces of Various Wettabilities
Percival J Graham

The study of droplet impingement is a vast field with diverse applications. Recently, superhydrophobic surfaces have shown great promise in reducing water accumulation. Studying the coalescence behaviour of water droplets on surfaces of various wettabilities can allow for a deeper understanding of how water repellant surfaces can effectively remain dry. Since the droplets coalesce and deform in a matter of milliseconds and are the size of a few millimeters, high speed imaging at high magnification is used. The experimental rig developed allows the camera, lighting and droplet generator to be mounted together to prevent any disturbances which can interfere with the imaging. Furthermore, MATLAB image processing toolbox is used to track the boundaries and a simple algorithm is used to remove the background prior to boundary tracking. Five types of surfaces are studied for both head on and offset cases. These surfaces include one hydrophilic, three hydrophobic and one superhydrophobic. The interplay between surface wettability, offset between droplets, droplet size and droplet speed is studied quantitatively by examining the free surfaces and qualitatively by examining the spread diameter. Morphology of the coalescing droplets is compared and the receding contact angle is seen to have a major role in the outcome of the droplet coalescence process. An extreme example of the effect of receding angle is seen on superhydrophobic surfaces. On a superhydrophobic surface, the impinging droplet will remove the sessile droplet should they succeed in coalescing. Increasing the size of the impinging droplet and the offset between the droplets decreases the effectiveness of the detachment mechanism. The maximum spread diameter reached is an important parameter. For a case of no offset, an analytical model is developed based on conservation of energy. Due to the complexity of offset cases, a unified regression model is developed. Lastly, at small inertias the impinging droplet may bounce or slide off of the sessile droplet. As inertia increases, the droplets coalesce sooner. The bouncing and delay in coalescence is attributed to the dissipation of air trapped between the two droplets.

Acknowledgements

First of all, I would like to thank you for taking the time to read my work. Hopefully you will enjoy or appreciate something in the coming 100+ pages, preferably my results and not ones cited, unless those are also my results.

This work was financially supported by the Natural Sciences and Engineering Research Council of Canada (NSERC), Bombardier Aerospace, Pratt and Whitney Canada and CRIAQ. Concordia University overall has provided me with a very important education as both an undergraduate a graduate student. This education will help me to achieve as much as possible. A major part of what made my graduate studies possible and fruitful is the support staff and technicians.

Further support came from my colleagues, Neil Roy Chowdhury, Mehran Farhangi, Hanny Gomma and Carole El Ayoubi, Hadi Alaee, Dennis DePauw, Navid Sharifi and Alfredo Martinez. Mixing guidance, structure and freedom is a difficult task and was well done by my supervisor Dr. Dolatabadi, who taught me many of the aspects of being a researcher.

Funding, guidance, supervision, technical help and editing are all important contributors to this thesis; however, support to start the day is invaluable and is what all other support is built upon. Thus, I would lastly like to thank my friends and family whose contribution is most important. Particularly Erica Corbeil, who always disagrees with me when I think I can't do something, I should listen to her more often.

Contents

I. Nomenclature

Basic properties

Symbol	Description	Unit typically used
D_0	Initial droplet diameter	[mm]
R_0	Initial droplet radius	[mm]
U_0	Impinging droplet velocity	[mm/s]
D_y	Wetted length of droplet	[mm]
D_{max}	Maximum wetted length of droplet	[mm]
L	Offset between droplets	[mm]
R_{eff}	Effective Radius of truncated sphere	[mm]
h	Droplet thickness while spreading	[mm]
b	Half thickness of dissipative region during merging	[mm]
δ	Thickness of boundary layer during spreading	[mm]
$(A_{ls})_0$	Initial liquid-solid interfacial area	[mm^2]
$(A_{ls})_f$	Final liquid-solid interfacial area	[mm^2]
$(A_{lv})_0$	Initial liquid-vapour interfacial area	[mm^2]
$(A_{lv})_f$	Final liquid-vapour interfacial area	[mm^2]
U_d	Detached droplet velocity	[mm/s]
V	Volume	[mm^3]
θ_S	Static contact angle	[°]
θ_A	Advancing contact angle	[°]
θ_R	Receding contact angle	[°]
$\theta_{sliding}$	Sliding Angle	[°]
$\Delta\theta$	Contact angle hysteresis	[°]
γ_{lv}	Liquid-vapour interfacial energy	[J/m^2]
γ_{ls}	Liquid-solid interfacial energy	[J/m^2]
γ_{sv}	Solid-vapour interfacial energy	[J/m^2]
t	Time, general	[ms]
t_s	Spreading time	[ms]
t_m	Merging time	[ms]
t_c	Contact time	[ms]
t_{dm}	Delayed coalescence time	[ms]
ϕ	Work done by viscous dissipation	[J]
ϕ_m	Viscous dissipation during merging	[J]
ϕ_s	Viscous dissipation during spreading	[J]
E_k	Kinetic Energy	[J]
E_{lv0}	Initial liquid-vapor interfacial energy	[J]
E_{lvf}	Final liquid-vapor interfacial energy	[J]
E_{ls0}	Initial liquid-solid interfacial energy	[J]
E_{lsf}	Final liquid-solid interfacial energy	[J]
ρ	Density	[kg/m^3]
μ	Viscosity	[kg/sm]

Dimensionless terms

Symbol	Description	Expression
λ	Dimensionless offset	$\frac{L}{D_0}$
ξ	Spread factor	$\frac{D_y}{D_0}$
ξ_{max}	Maximum spread factor	$\frac{D_{max}}{D_0}$
ξ	Spread factor	$\frac{D_y}{D_0}$
ξ_{max}	Maximum spread factor	$\frac{D_{max}}{D_0}$
Ψ	Spread effectiveness	$\frac{D_y}{L + D_0}$
Ψ_{max}	Maximum spread effectiveness	$\frac{D_{max}}{L + D_0}$
We	Weber number	$\frac{\rho {U_0}^2 D_0}{\gamma_{lv}}$
Re	Reynolds number	$\frac{\rho U_0 D_0}{\mu}$
We_{sl}	Surface Weber number	$\frac{\rho {U_0}^2 D_0}{\gamma_{sl}}$
τ	Dimensionless time, general	$\frac{tU_0}{D_0}$
τ_c	Dimensionless contact time	$\frac{t_c U_0}{D_0}$
τ_{dm}	Dimensionless delayed coalescence time	$\frac{t_{dm} U_0}{D_0}$
ε	Restitution coefficient	$\frac{U_d}{U_0}$

II. List of figures

III. List of tables

1 Introduction

"The splash of a drop is a transaction which is accomplished in the twinkling of an eye, and it may seem to some that a man who proposes to discourse on the matter for an hour must have lost all sense of proportion. If that opinion exists, I hope this evening to be able to remove it, and to convince you that we have to deal with an exquisitely regulated phenomenon, and one which very happily illustrates some of the fundamental properties of fluids."- A.M. Worthington, 1895 [1]

1.1 The study of droplets

The study of droplet dynamics began over 100 years ago with the works of Arthur M. Worthington [(1)], [(2)] in "The Splash of a Drop" and "A Study of Splashes", using what at the time was considered high speed photography. By studying the behaviour of water and milk droplets impinging in liquid pools he was able to formulate intuitive understanding of the behaviour of droplets. The observed behaviour included bouncing, resting of the droplet on a liquid pool, different types of splashes and jetting due to cavity collapse. Over the past 100 years, many researchers have pursued work related to droplets impinging in liquid pools, colliding together, impacting surfaces and coalescing. An extensive body of knowledge has been obtained; however, many more questions regarding droplet behaviour have been formulated than resolved. Information and discoveries related to droplet impingement dynamics continue to progress despite the age of this topic. In 2011, Thoroddsen et al. [(3)] presented a mechanism for droplet splashing on a liquid pool characterized by a slingshot type mechanism characterized by the rupture of a sub micrometer thick liquid sheet [(3)]. The difference in obtained results is illustrated in Figure 1, which compares the work of Worthington and Thoroddsen. A water droplet is seen to impinge in a pool of milk in the works of Worthington, while the ejecta sheet and ensuing micro/nano droplets are shown in the works of Thoroddsen. (The author has great interest if an individual should succeed in obtaining funding from the dairy industry for research related to milk droplet impingement.)

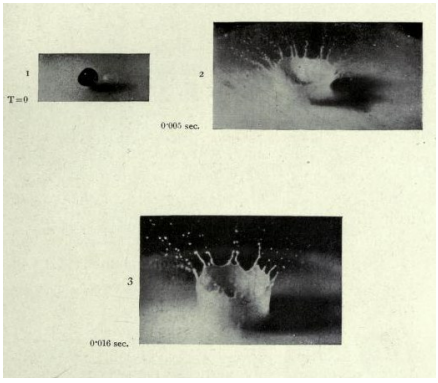

(a)

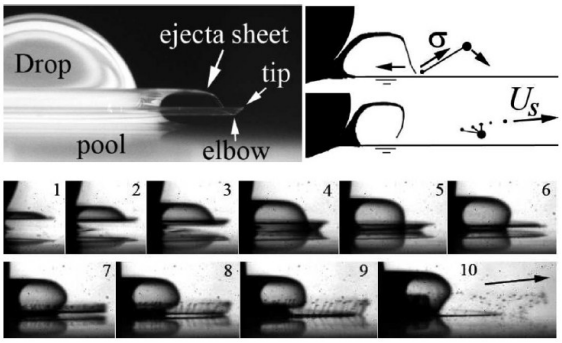

(b)

Figure 1: The study of droplets, then and now. (a) Water Droplet impacting into milk from page 63 of "A study of Splashes" [(2)] and (b) the presence of a sub micrometer ejecta sheet and the ensuing slingshot break-up mechanism [(3)]

In addition to presenting interesting images and fascinating phenomena, the study of droplets has remarkably diverse practical applications. Firstly, falling from the sky, rain droplet and wind driven rain are important parameters for pollution accumulation on building facades and erosion [4]. Furthermore, erosion caused by water droplets occurs on a much larger scale, for example soil erosion [5] and smaller scales such as the inside of gas turbine engines. Pollution accumulation and the dilution of paint are increased by more total mass of water accumulated, as opposed to erosion which is more based on total droplet impacts and droplet inertia. The first step in water accumulation, the impact of a single droplet on a dry surface has received substantial study; however, the subsequent steps of rivulet and film formation have received less attention. It is possible that droplet coalescence is a building block for these phenomena.

Droplet accumulation is not always a negative thing, since it is required for spray coating, painting and ink-jet printing. Studies related to ink-jet printing are geared towards understanding how the interplay between impact conditions can cause a decrease in line uniformity and continuity. [6], [7], [8], [9] Painting also requires an understanding of both droplet impact and droplet coalescence. Furthermore, spray coating requires the behaviour of molten metal droplets impacting, deforming and solidifying on a substrate. Extensive studies have been performed related to metal droplet deposition to better understand the quality associated with spray coating. [10], [11], [12], [13] These studies typically look at the interplay between the droplet's morphological changes and the thermal and solidification changes, for example the works of Dhiman and Chandra, [10] showed that the solidification of a metal droplet may cause a ridge, which in turn causes splashing. Lastly, knowledge regarding the coalescence of droplets has also been developed in the interest of combustion, since minimizing droplet size tends to increase combustion efficiency [14], [15], [16], [17], [18]. These studies have focused on both droplet colliding together in a gaseous medium [14], [15], [16], [17] and droplets collecting on a surface[18].

When considering freezing conditions, water accumulation takes on the additional threat of ice accumulation. In addition to power failures associated with collapses of electrical transmission lines, power generation by wind turbines can also suffer due to decreased aerodynamic performance. The aerospace industry also needs to consider ice accumulation, since the decreased aerodynamic performance may result in catastrophic events [19], [20], [21]. Typically aircrafts are designed for icing conditions consisting of droplets under 100 μm; however, super-cooled large droplets, which are up to a millimeter in size, are such a substantial threat that aircrafts avoid those icing conditions entirely. The threat from these droplets is their large size and low temperatures which allow them to rapidly freeze

on contact with the airfoil [20]. Therefore; there is a vast array of droplet sizes that need to be studied related to ice formation.

1.2 Motivation

As previously mentioned, a vast array of industrial applications can benefit from a deeper understanding of droplet dynamics, such as ink-jet printing, spray coating, water and ice accumulation and erosion among many others. [6], [7] , [8], [9], [10] The current investigation is motivated by the result presented in Figure 2 where a surface which actively repels water is seen to have no ice accumulation, in contrast to a surface that is not water repellant has accumulated a substantial amount of ice. Common industry standard is to study water and ice accumulation on a macro scale through the use of sprays and ice sheet thickness over a time scale of several minutes, which fails to yield in depth understanding of how some surfaces prevent accumulation of ice and water. [19] A lack of full understanding of droplet mechanics will not yield with certainty correct design methodologies and ultimately not deliver optimized systems.

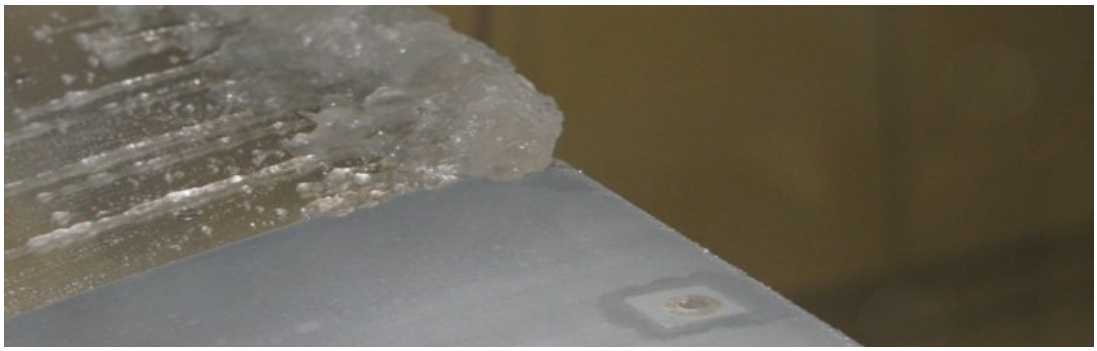

Figure 2: Performance of a superhydrophobic surface as compared to hydrophilic surface in icing conditions [19].

This study is dedicated towards understanding the onset of droplet accumulation on surfaces of various wettabilities, by studying the dynamics related to a sessile droplet being impacted by an oncoming droplet. Coalescence of droplets could be considered the first step in film and rivulet formation, for which an understanding would greatly benefit the aerospace industry. The experiments performed only deal with isothermal cases. The complexity of droplet accumulation requires understanding of surface wettability; droplet impact dynamics; droplet coalescing mechanics; among many others.

1.3 Surface wettability

The two surfaces used in Figure 2 are hydrophilic and superhydrophobic. Water droplet behaviour on surfaces can be characterized by two surface properties: repellency and mobility [22], [23], [24]. The repellency of a surface is manifested as the static contact angle, θ_S, whereas the advancing, θ_A, and receding, θ_R, contact angles are associated with mobility. The static contact angle can express the water repellency of a surface and is used to distinguish between hydrophilic and hydrophobic surfaces, it is measured while the droplet is not moving and is indicated in Figure 3. A hydrophilic surface has a contact angle less than 90° and a hydrophobic surface has a contact angle larger than 90°, [25] the distinction is shown in Figure 3. One method of measuring droplet mobility involves tilting the plate until the droplet is resting on until the droplet begins to slide. Three angles are obtained from this experiment, the advancing contact angle; the receding contact angle; and the sliding angle. These three angles are shown in Figure 4, by displaying a tilted plate experiment. The sliding angle is the angle of the substrate required for the droplet to begin sliding. A smaller sliding angle indicates a more mobile droplet. The sliding angle is heavily sensitive to boundary conditions such as droplet size; droplet deposition method and manner of inclining the substrate[24]. Receding and advancing angles are also measured when the contact line is about to move. Together, the advancing and receding angles can be used to determine contact angle hysteresis, $\Delta\theta = \theta_A - \theta_R$. Surfaces with small hysteresis are considered more mobile.

(a) (b)

Figure 3: Distinction between (a) hydrophilic and (b) hydrophobic surfaces.

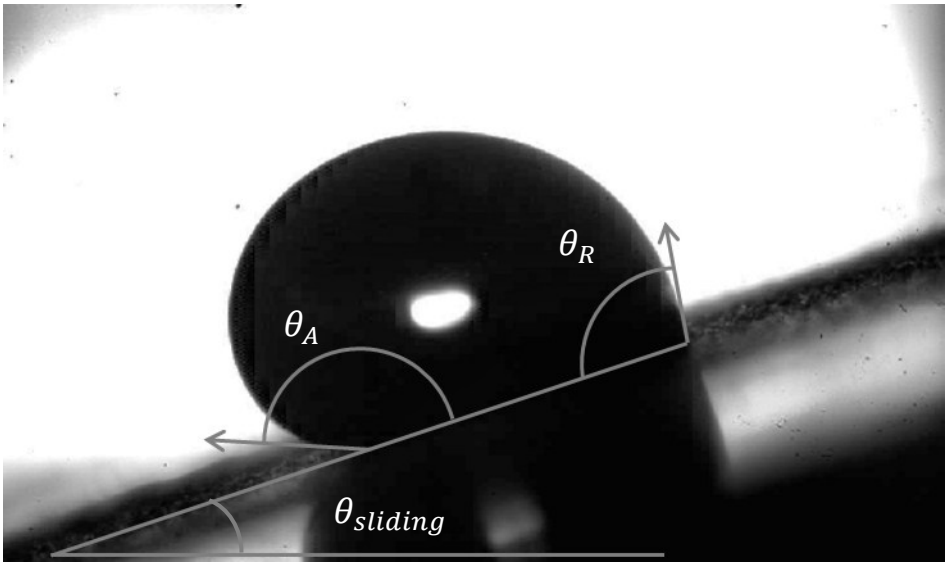

Figure 4: Advancing, receding and sliding angles of a droplet on a tilted plate.

Based on the previously defined surface characteristics, it is possible to define up to four types of surfaces, which are superhydrophylic, hydrophilic, hydrophobic and superhydrophobic. It is not uncommon to see some literature use the term ultrahydrophobic, but they are typically referring to superhydrophobic surfaces [(25)]. As previously mentioned, the distinction between hydrophilic and hydrophobic surfaces is the static contact angle. Superhydrophylic surfaces are also distinguished based on their static contact angle, which is nearly zero. A water droplet on a superhydrophylic surface will spread until it becomes a film. In contrast, a superhydrophobic surface has exceptional repellency and mobility. The distinction between hydrophobic and superhydrophobic is attributed to the mobility of the droplet. Both superhydrophylic and superhydrophobic surfaces have been successfully applied for commercial applications where water accumulation is not desired [(26), (27)]. The superhydrophylic surfaces were found practical for buildings since droplets would form thin films then evaporate, [(27)] while superhydrophobic surfaces do not accumulate water since the droplets themselves can be easily removed, or bounce off of the surface instead of adhering to the surface [(28) , (29), (30), (31)].

Table 1: Different types of surfaces and their water repellency and mobility [32], [33].

Surface type	Static contact angle	Contact angle Hysteresis
Superhydrophylic	<10°	<10°
Hydrophylic	10-90°	>10°
Hydrophobic	90-150°	>10
Superhydrophobic	>150°	<10°

Even older than the study of splashing on surfaces, is the study of wettability: two hundred years ago, Young presented an equation, which relates liquid-solid (γ_{ls}), solid-vapour (γ_{sv}) and liquid-vapour (γ_{lv}) interfacial energies to the contact angle of a three phase line, as shown in equation (1) [34]. Young's equation is schematically depicted in Figure 5. The contact angle is the result of the balance of the three forces. Wetting of a surface is understood by two aspects, molecular interaction between the liquid and the surface and the effect of micro and nano structures on the surface interacting with the liquid in question. Oil and water are known not to mix since the bonds inside oil molecules are covalent, whereas the bonds in water molecules are substantially more polar. Similarly, surfaces that are made with fluorocarbons [35] or coated with molecules containing non-polar functional groups will also be hydrophobic [36], [37].

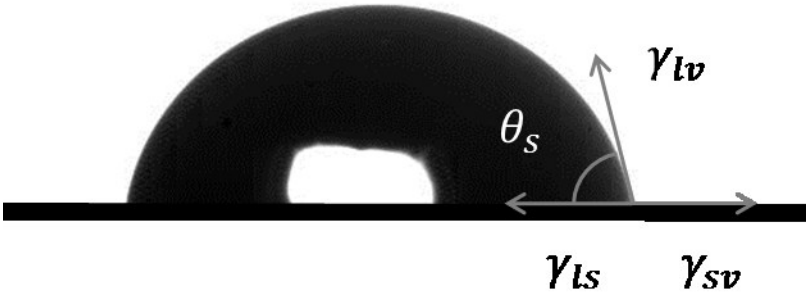

Figure 5: Depiction of the three tension forces present at the three phase line.

$$\cos\theta_s = \frac{\gamma_{sv} - \gamma_{sl}}{\gamma_{lv}} \qquad (1)\ [34]$$

The manner in which a droplet interacts with a rough surface can be understood through the works of three different researchers: Cassie, Wenzel and Pease, where Cassie and Wenzel have garnered most of the attention. [38] The models presented by Cassie and Wenzel relate the wetted area to the contact

angle, while other works of Pease study the actual contact line. A droplet on a rough surface can either sit on top of the roughness elements (Cassie state), or penetrate into the elements (Wenzel state) as shown in Figure 6 [28), (38), (39), (40)]. Partial penetration of the liquid into the roughness of the surface is referred to as a mixed regime [(41)]. The Cassie regime is considered to cause superhydrohpobic surfaces, which have both high mobility and high water repellency, whereas the Wenzel state droplet suffers from a lack of mobility [(22), (41)]. It was found, by Gao and McCarthy [(38)] that the wettability at the three-phase line controls the contact angle and not the entire area beneath the drop. This was unveiled by creating hydrophobic surfaces with a hydrophobic spot, or vice versa, and depositing a droplet on them, their results were published with the provocative title "How Cassie and Wenzel were wrong." The disagreement between Cassie and Wenzel models and the findings of Gao and McCarthy [(38)] does not refute the importance of the penetration of liquid into the roughness elements of a surface, but confines the importance of this transition to the three phase line. Surfaces used in the current experimental works are homogeneous unlike the works of Gao and McCarthy [(38)]. Therefore the discussions presented by Wenzel and Cassis are suitable for the cases presented throughout this thesis.

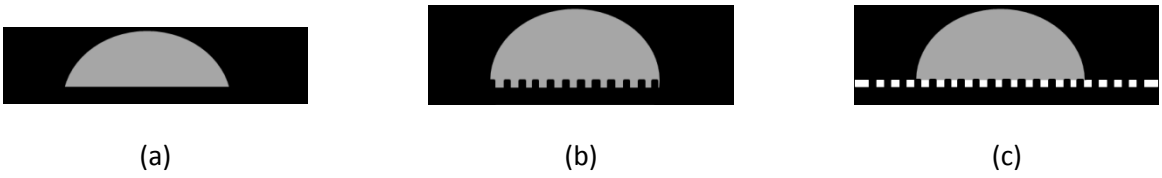

(a) (b) (c)

Figure 6: A droplet on a (a) smooth surface, (b) rough surface in the Wenzel state, and (c) rough surface in the Cassie state

Changes in apparent contact angle with varying roughness was qualitatively studied by Johnson and Dettre, [(42)] who varied the roughness of wax and measured the resulting advancing and receding contact angles. As roughness was increased from a smooth surface to a rougher surface, the advancing contact angle increased, while the receding angle decreased, until a point where the receding angle increased drastically [(42)]. This behaviour switch could be attributed to a switch from a Wenzel to a Cassie state. Many studies exist relating surface morphology, droplet size, impinging velocity and time expose to wetting and whether the droplet exits in either a Cassie or Wenzel state [(41), (43), (44)]. Overall, larger droplets on surfaces with roughness elements with greater spacing between them are more likely to behave in the Wenzel mode than in the Cassie mode [(22), (41), (44), (45)] It is important to not limit hysteresis to rough surfaces, since hysteresis is also possible on smooth surfaces[(32)].

Johnson and Dettre [42] displayed a very important discovery relating the roughness to a decrease in contact angle hysteresis and such a revelation greatly helped advancing water repellant surfaces. However; nature was far ahead of them: lotus leaves and the legs of water spiders have elaborate micro and nano structures allowing them to be superhydrophobic [28], [46], [47]. The lotus leaf is depicted in Figure 7 as having micro structure roughness elements, which in turn are coated in nanostructures, resulting in a Cassie state droplet and a superhydrophobic surface [46]. Creating similar structured surfaces and determining the optimal micro and/or nano structure has become an emerging field [48].

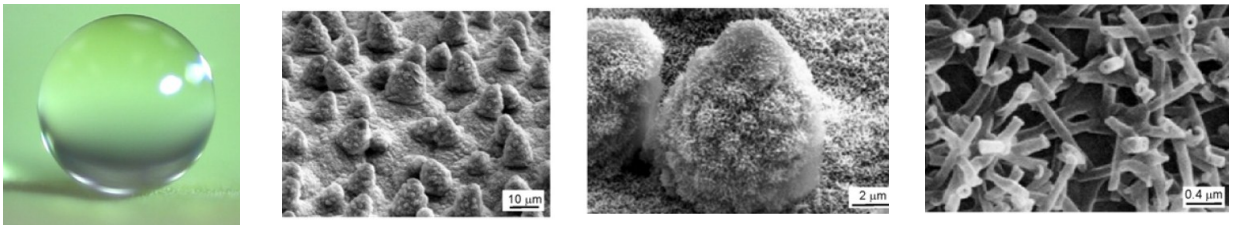

(a) (b) (c) (d)

Figure 7: Hierarchical superhydrophobic structures in nature, (a) A droplet resting on a lotus leaf and (b-d) increasing magnification of surface topography.

1.4 Droplet impact

1.4.1 Experimental studies

As presented at the onset of the introduction, the study of the dynamics of droplets is vast and continuously unveiling new aspects of nature encountered in a variety of applications. A strong review of droplet impingement on both wetted and dry surfaces using numerical and experimental techniques is done in the works of Yarin. [49] For various impact conditions, liquid properties and surface properties, Rioboo et al. [50] summarized six different regimes of droplet behaviour. These regimes are shown in Figure 8 and include deposition for low inertia cases on non superhydrophobic surfaces; different types of splashes for increased inertia; and rebound of partial rebound in the case of hydrophobic surfaces. More details regarding droplet impingement on superhydrophobic surfaces will be discussed in later sections.

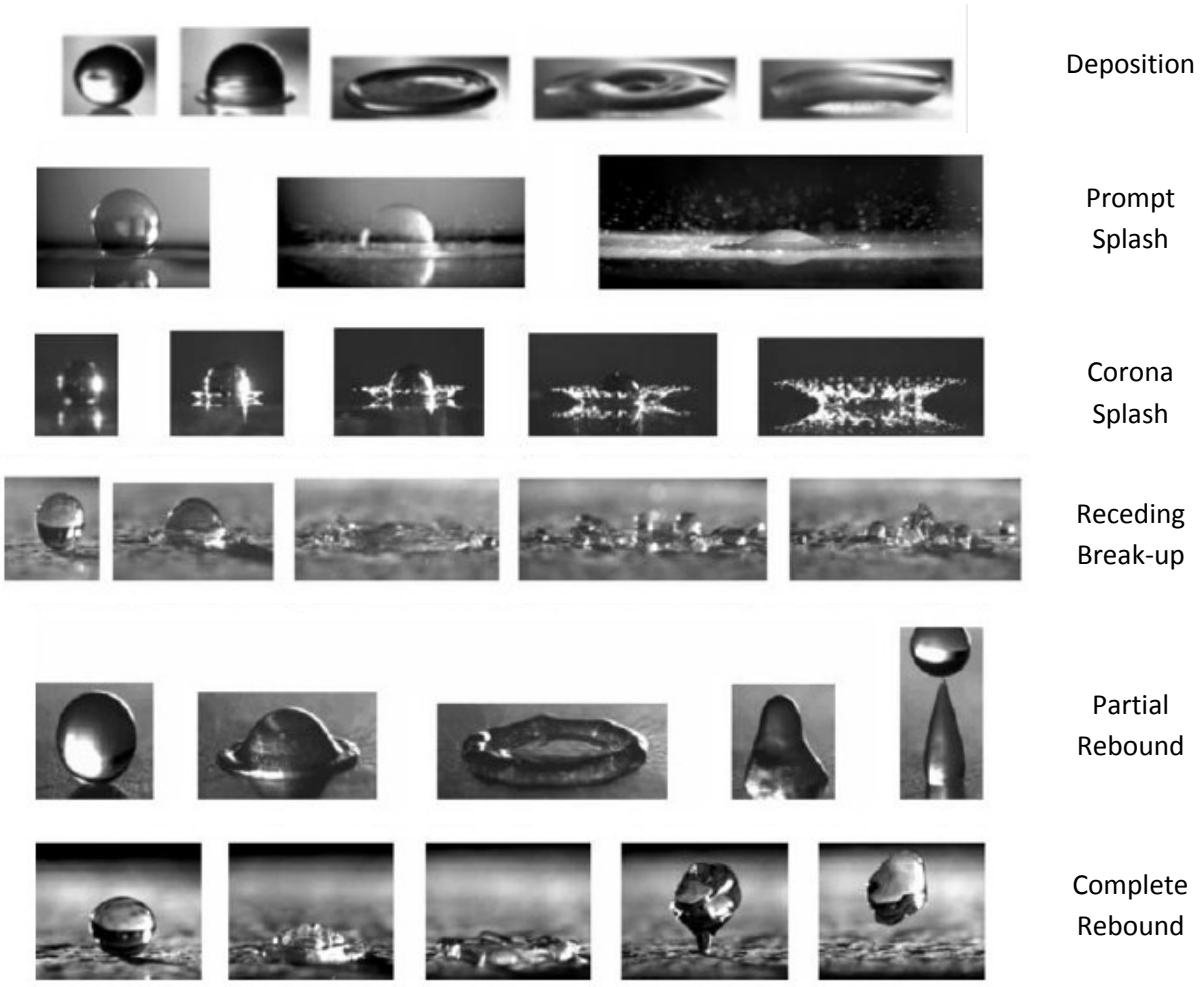

Figure 8: The various regimes of droplet impact [50].

Droplet impingement can be divided into four stages: the kinematic phase, the spreading phase, the relaxation phase and the wetting/equilibrium phase, as seen in Figure 9 [51].The initial phase is known as the kinetic phase, during such a phase the temporal evolution of the spread diameter is identical for all cases when normalized with droplet properties and impact parameters. During such a phase, the droplet resembles a truncated sphere and will experience an internal shock wave [52]. The spreading phase follows the kinematic phase and is defined by the presence of a thin lamella being ejected from the periphery of the contact line. This lamallae grows in thickness and diameter until the droplet becomes fully spread. During the spreading phase, the effects of inertia, viscosity, surface tension and surface wettability begin to play a role, where velocity and droplet diameter increase the spreading rate, whereas inertia and surface tension reduce the spreading rate [51]. The spreading phase can be simplified

to a shrinking sphere and a growing cylindrical disk [53], [51], [54], [55]. Should the inertia prove sufficiently high, a rim with a thickness greater than the lamellae is formed [54]. Once the droplet has reached its maximum spread diameter, the spreading phase has stopped. Surface wettability and roughness have a more serious effect during the receding and relaxation phase than they do on the spreading phase, as seen in Figure 9. A highly wettable surface such as glass will have little recoiling, whereas non-wettable surfaces can exhibit substantial recoiling as well as partial if not full detachment [28], [51], [53], [54].The droplet then oscillates until it reaches an equilibrium state with a contact angle somewhere in between the advancing and receding contact angles.

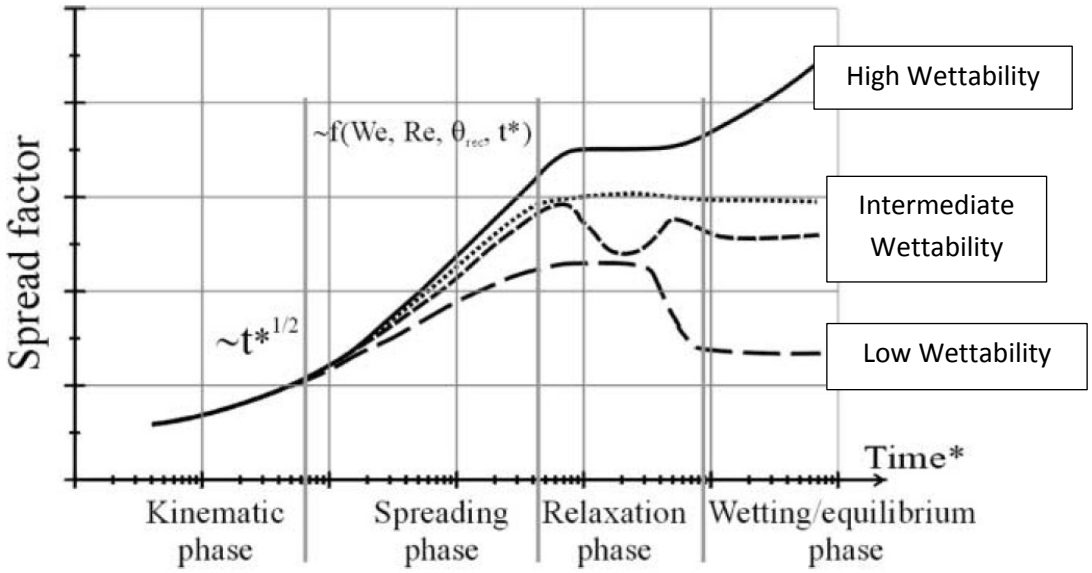

Figure 9: Phases of a droplet impinging a non-superhydrophobic surface [51].

When a droplet impacts a superhydrophobic surface the regimes change substantially from what was previously discussed as summarized in Figure 10. At low velocities, the droplets do not bounce from the surface [28], [56]. As impinging velocity is increased, bouncing in various forms can occur with different degrees of deformation, unless a sufficiently high velocity for splashing to occur is achieved. The morphologies of the bouncing take the following forms: bouncing with slight deformation; bouncing with jetting; bouncing with partial pinning; pinning and partial detachment. Changes from one domain to another depend on both droplet inertia and surface characteristics [28], [56] . During the recoiling of the droplet, a Worthington jet can be formed due to cavity collapse and strong radial contraction, which

drives radial momentum into axial momentum [57]. As this cavity collapses air can be trapped, this can result in a high pressure jet.

Another possible feature of droplet impingement and recoiling on superhydrophobic surfaces is pinning. Pinning is said to have occurred when a portion of the droplet sticks to the surface, which can prevent rebound or change the morphology of the detached droplet. This sticking phenomenon could be understood as a change from Cassie to Wenzel state due to the inertia of the droplet forcing the liquid to penetrate into the roughness elements. Inertia is manifested as either dynamic pressure or effective water hammer pressure of the droplet [22), 58), 59]. Another way to look at this phenomenon is as an energy barrier, where a droplet with sufficient kinetic energy can overcome the energy barrier to penetrate into the roughness elements [56]. In either understanding, if the droplet size and speed are high enough, the droplet can penetrate into the roughness elements, entering a Wenzel state rather than resting on top of the roughness elements and behaving in a Cassie state.

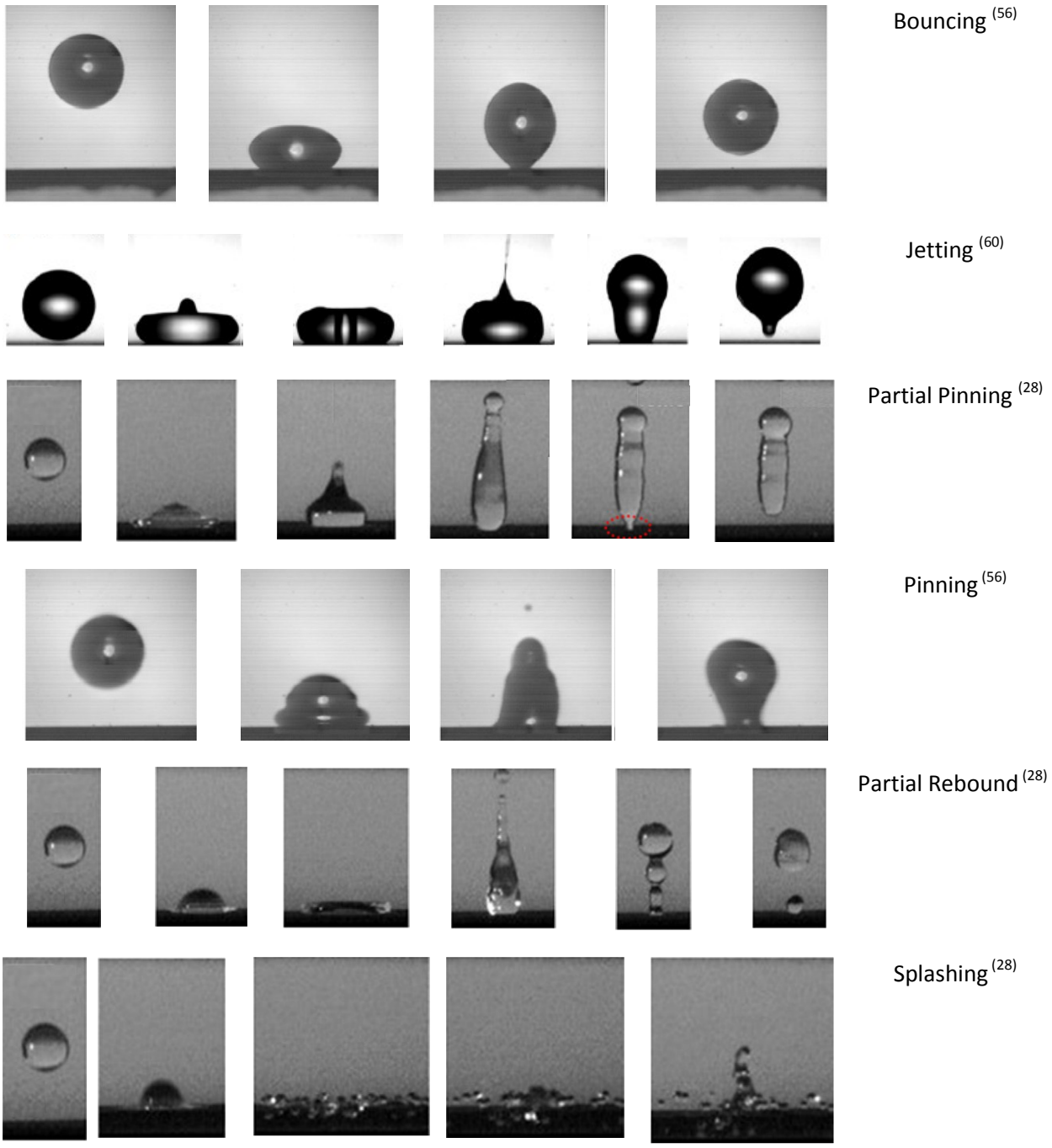

Figure 10: Droplet behaviour on a superhydrophobic surface [28] , [60].

1.4.2 Modelling droplet impact

Measurements and detailed imaging of droplet morphology during impact is of great interest; however, being able to predict or model the deformation of a droplet is highly practical for industry. This is typically accomplished by analytical and numerical models. Numerical modelling is frequently used by scientist and engineers and has become very accurate, reasonable and cost effective. However, some details related to droplet dynamics are difficult to capture using numerical modelling, particularly at the three phase line. The contact angle measured and previously discussed could be interpreted as an apparent or macro scale contact angle; in contrast to an actual or micro contact angle [(32), (61)]. The contact angle measured from a droplet at the millimeter scale is the average of the many micro contact angles which are too small to visualize [(32)]. For their numerical work, Sikalo et al. [(61)] used grid sizes larger than the micro contact angle scale to ensure accuracy of their results. In this case, it is interesting to note that decreasing the mesh size may have a negative effect on numerical accuracy.

By coupling numerical and experimental data, studies have succeeded in presenting meaningful insight into droplet dynamics. By validating the profiles and details of the free surface, the internal velocity fields from numerical results can be validated to yield a deeper understating or justify assumptions for analytical models. This is more cost effective than using techniques such as particle image velocimetry. Similar collaborations are present when studying merging droplets.

A great deal of work has been done on determining the spreading and recoiling of a single droplet impinging on a solid surface by analytical methods. The conservation of mass, energy and momentum are used in addition to geometrical simplifications [(53), (55), (54), (62)]. Ukiwe and al. [(63)] presented four models from literature for the maximum spreading length then improved upon the most accurate model they found, which was presented by Pasandideh-Fard et al., [(55)] by changing how the liquid-solid interfacial energy is determined. Interfacial energy is the energy associated with the interface between two phases, in this case, the interface between the liquid and the substrate. Pasandideh-Fard et al. [(55)] used the contact angle of the droplet once it is fully spread; in contrast, Ukiwe and al. [(63)] used the equilibrium contact angle. In the more recent work of Vadillo et al. [(64)], a dynamic contact angle during the experiment was used to obtain the liquid-solid interfacial energy. The use of such an angle was more accurate for high viscosity fluids, i.e. μ =100mPas and highly wettable surfaces. It is important to note that the surfaces prepared by Ukiwe and al. [(63)] and Vadillo et al. [(64)] have a roughness on the order of nanometers, which makes the assumptions of homogeneity valid. In the works of Chibowski [(32)] the

interfacial energy is calculated based on both the advancing and receding contact angles as opposed to the various angles used by Vadillo et al. [64], Pasandideh-Fard et al. [55] or Ukiwe and al. [63]

The model developed in the works of Pasandideh-Fard et al. [55] is based on conservation of energy and enables the prediction of the maximum spreading diameter. It is an improvement on the works of Chandra and Avedisian [53] by adjusting the amount of viscous energy dissipated during the spreading process. Both previously mentioned papers simplified the viscous dissipation using a quasi-steady state analysis, and assuming the deformation to be approximated by a spherical cap draining into an expanding disk, Figure 11 shows the assumed shape. The energy lost (ϕ) due to viscous dissipation can be simplified as done in equation (2) [53].

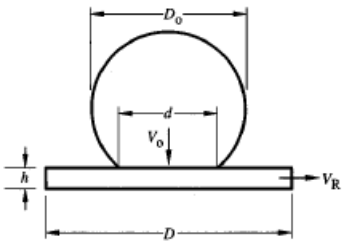

Figure 11: Approximation of droplet spreading on a surface [53], [55].

$$\phi = \int_0^{t_s} \int_V \mu \left(\frac{\partial v_i}{\partial x_j} + \frac{\partial v_j}{\partial x_i} \right) \frac{\partial v_i}{\partial x_j} dV dt \approx \mu \left(\frac{dU}{dx} \right)^2 V \, t_s \qquad (2)$$

Improvements between the works come from adjusting the time required for dissipation, internal velocity profile, and volume of dissipating fluid. The key element unveiled in the works of Pasandideh-Fard et al. [55] was determining the thickness of the boundary layer inside the droplet based on the stream-function of a stagnation point flow as opposed to assuming a linear velocity distribution across the entire thickness of the droplet, as done by Chandra and Avedisian. [53] This improvement affected both the volume of dissipative fluid and the velocity gradient and was validated by numerical results, which are shown in Figure 12. In addition the time required was improved by noting the dimensionless time based on the maximum spread diameter and velocity required to reach maximum spreading is

independent of velocity; [53] whereas in the works of Chandra and Avedisian [53] the time is assumed to be the ratio between droplet size and velocity.

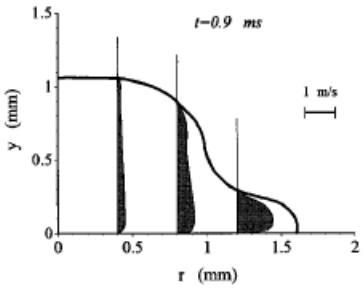

Figure 12: Numerical Results for the internal velocity field of a spreading droplet from the works Pasandideh-Fard et al. [55].

Their resulting analytical model shows the dependency of Weber number, Reynolds number and substrate wettability on maximum spreading diameter. Equation (3) [55] presents their result, yet generalized to reflect the various angles used by Ukiwe and al. [63] and Vadillo et al. [64] by using the notation θ_x.

$$\xi_{max} = \frac{D_{Max}}{D_0} = \sqrt{\frac{We + 12}{3(1 - cos\theta_x) + 4\left(\frac{We}{\sqrt{Re}}\right)}} \quad (3)$$

Pasandideh-Fard et al. [55] noted that the term related to surface wettability, $1 - cos\theta_x$, could be at most 2 and considered negligible for extremely high Weber numbers. A similar change in spreading behaviour was observed experimentally in the works of Clanet et al. [65] As inertia is increased, a transition from a capillary regime to a viscous dominated regime. In the capillary regime, the maximum spreading depends on surface tension; in contrast, to a viscous regime where maximum spreading is dependant more on fluid viscosity. The simplified expression is shown in Equation (4), which is the expression for maximum spreading in the viscous regime [55].

$$\xi_{max} = 0.5\, Re^{0.25} \quad (4)$$

Roisman et al. [51] used conservation of momentum approach to determine the evolution of the spread diameter over time for high inertia cases. At such high inertias, the droplet can be approximated by two sections: (1) a lamellae surrounded by (2) a rim. As the droplet spreads, liquid from the lamellae fills into the rim. The Navier-Stokes equations for each section of the droplet were solved together, to give the spread diameter over time. For the onset of droplet impact, conservation of energy was used to determine the initial size of lamellae. Similar approaches were done for the cases of binary droplet collisions at high inertia cases by Roisman. [66] Despite the accuracy of these models to predict the spread diameter over time, they fall short in predicting the maximum spreading diameter, as was summarized by Ukiwe et al. [63]

1.5 Droplet coalescence

After the impact of a first droplet, the effect of the second droplet would help provide insight into the accumulation of water droplets, as it may pertain to rivulet formation or film formation. Coalescence of droplets can easily be encountered by aircrafts flying into clouds or building during rainstorms. In addition to the accumulation of water droplets, the dynamics of droplet coalescence on a substrate is important for printing industries [7], [9], [8], [67]. Furthermore, coalescence of droplets without the presence of a substrate is important for spray technology, nuclear fusion, combustion, rain drop formation to name a few [14], [17], [68]. Experimental results from literature related to binary droplet collisions and bouncing droplets will first be presented, followed by a summary of analytical models.

1.5.1 Binary droplet collisions

A discussion on binary droplet collision without the presence of a substrate is helpful for understanding basic aspects of droplet coalescence. Binary droplet collisions can be categorized into five regimes based on the Weber number and offset between the droplets. These regimes include coalescence after minor deformation, bouncing, coalescence after substantial deformation, coalescence followed by separation for near head-on collisions and coalescence followed by separation for off-centre collisions. These regimes are depicted in Figure 13, which were obtained by colliding hydrocarbon droplets in air at atmospheric pressure [14], [17], [68]. As seen in Figure 13, increasing the inertia causes regimes to switch from coalescing to bouncing then back to coalescence, then ultimately separation.

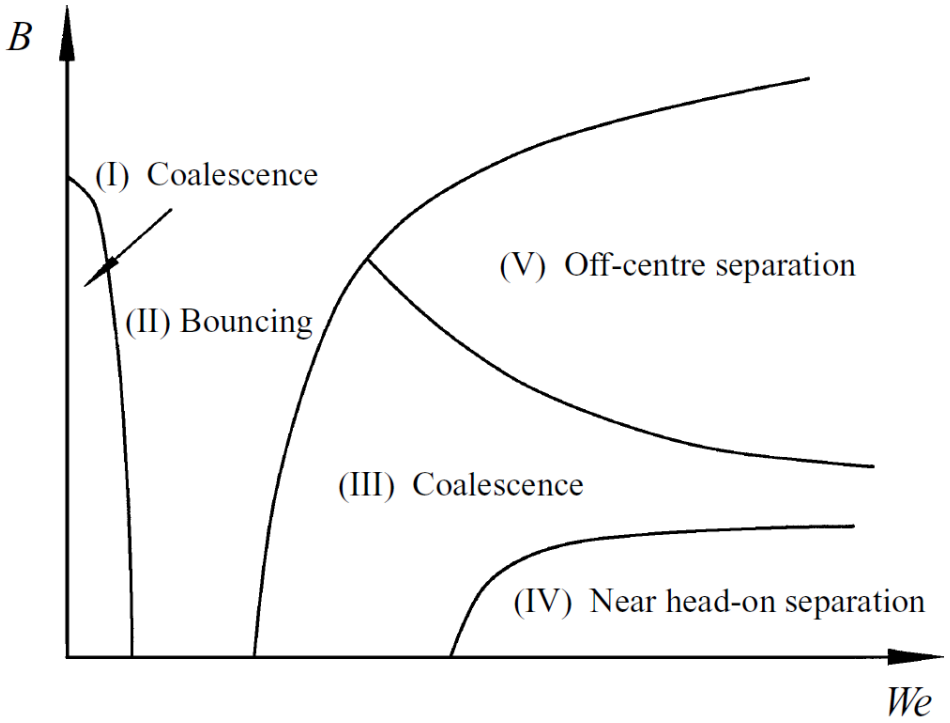

Figure 13: Regimes of binary droplet collisions in a gaseous medium [71].

Qian and Law [17] also performed experiments with water in different gas pressures and noted that the bouncing regime does not exist for water droplets at atmospheric pressures. The bouncing regime is attributed to small layers of air entrapped between the two droplets [15],[17], [68], [69], [70] and depends highly on both the mediums' viscosity and density; and the droplet's surface tension and inertia. A more elaborate discussion on bouncing droplets is presented in Section 1.5.2.

The coalescence of droplets on substrates with small amounts of inertia has been studied by increasing the volume of one droplet until it reaches the other; increasing humidity until droplets condense on a surface; or in the case of superhydrophobic surfaces with a gentle airflow to cause the droplet to displace. Surface tension driven coalescence was studied by Sellier et al. [71], Kapur et al. [72], Menchaca-Rocha et al. [73] and Thoroddsen et al. [74]. The results present a rapid neck growth between droplets promoted by surface tension and obstructed by viscosity. Ristenpart et al. [75] measured the growing connection between the two droplets and found it is heavily influenced by the droplet height and radius. A similar mechanism has been observed by Boreynko et al. [76] where condensing droplet coalesce on a

superhydrophobic surface, then as a result the potential energy associated with the merging is enough to detach the droplet from the surface.

Ink-jet printing and similar technologies that require the formation of lines from sequential deposition of droplets benefit from a greater understanding of coalescence dynamics. Parameters such as droplet size, spacing between droplets, temperature of droplets, and surface wettability all affect the printed line width and quality [6], [7], [67], [77]. Both uniformity of the thickness and continuity of the line are required in order to claim that a printed line is of quality. Uniformity of the thickness was studied by Stringer and Derby, [6] Soltman and Subramanian, [7] Duineveld, [67] Gao and Sonin [77] while Li et al. [9] studied the continuity of a printed line. Large spacing will cause broken lines, or a series of individual droplets. As spacing is decreased the line goes from scalloped to uniform, with increasing thickness as spacing is decreased [6], [7], [67], [77]. Due to surface tension forces, the sessile droplet is capable of pulling the impinging droplet towards it during the recoiling process, resulting in discontinuity of the printed line[8], [9].

1.5.2 Bouncing droplets

As previously mentioned, for low inertia cases it is possible for droplets to rebound off each other [16]. Furthermore, it was also observed for droplets to bounce off of pools of liquid [69], [70], [78], [79], [80] and other sessile droplets [80], [81]. The effect of an intervening air layer is the cause of this bouncing behaviour as discussed in the relevant works. In both cases, the air layer must be drained in order for the droplets to merge. These works did not study the effect of humidity, which may play some role in bouncing or delayed coalescence. Higher humidity may promote coalescence due to the increased presence of water molecules in the gas. Zero humidity environments and air were both studied and show bouncing is possible; however the degree of humidity and the time required for coalescence were not studied. [17]

The effect of the intervening air layer was studied in a joint numerical and experimental study in the works of Pan et al. [68]. Experimental data was used to enhance the numerical results by imposing an artificial interface between the two droplets to represent the intervening air layer. In the experimental results, a concavity switch at the interface can be observed, this change in concavity is considered the moment where the intervening air layer has been dissipated. Two cases from the works Pan et al. [68], one of merging and one of bouncing are shown in Figure 14. The similarity between the experimental and numerical results for both the bouncing case and the merging case validates both the numerical results and the assumption regarding the moment of merging.

Bouncing, Tetradecane in 1atm air, We = 2.27 Merging, Tetradecane in 1atm air We = 13.63

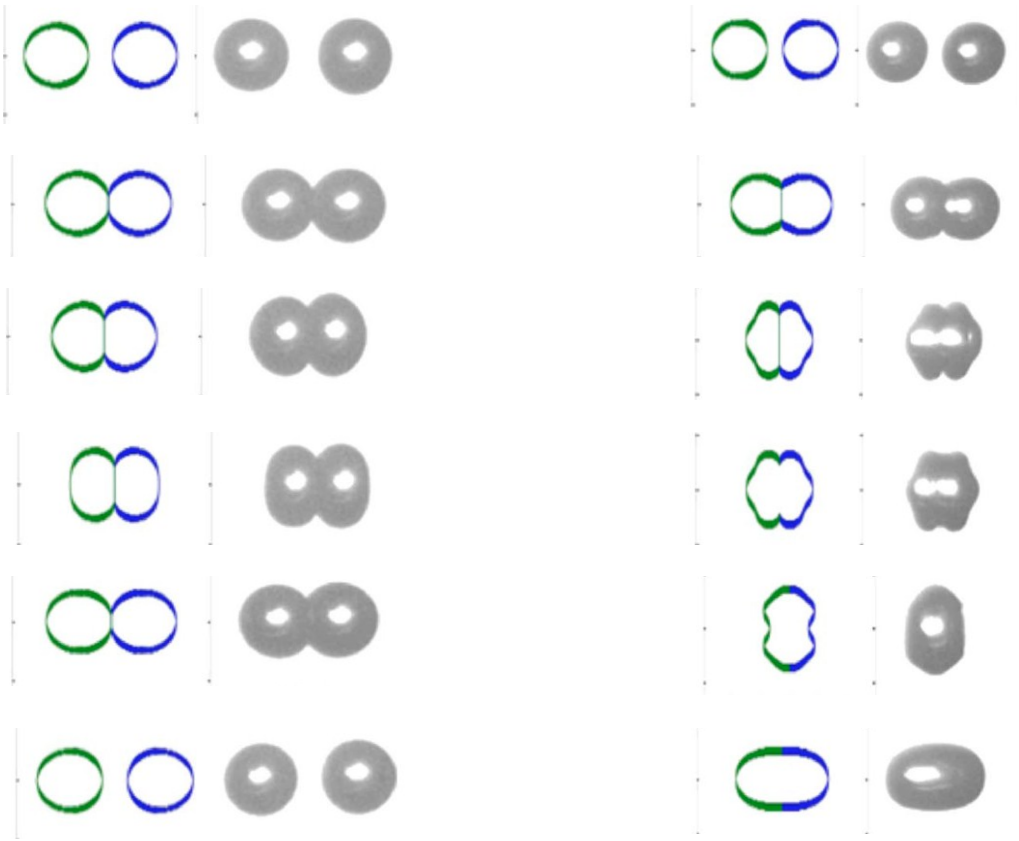

Figure 14: Comparison of experimental and numerical results of a binary droplet collision with an artificially imposed interface [68].

When a droplet impacts a liquid pool or liquid layer it has been shown to not merge if the velocity is low enough or if the surface is vibrating. In fact, some researchers have been able to maintain a droplet resting on a liquid pool for thirty minutes by oscillating the base of the liquid pool [70]. In order to capture the presence of the intervening air layer Terwagne et al. [69], [79] used white light interferometry to approximate the thickness of this intervening air layer to be between 100nm and 10µm. A model based on the droplet deformation and lubrication theory was developed to explain these results and can predict air bubble entrapment [79]. Work related to droplets merging on sessile droplets as opposed to a liquid pool which is similar to the current works was performed for water and soap-water mixtures by Wang et al. [81]. Four regimes were noted: bouncing, conglutination with and without separation and merging, these regimes are shown in Figure 15[81]. Low speeds resulted in bouncing, high speeds resulted in merging and intermediate velocities resulted in the conglutination effects. Conglutination

could be considered as merging during the receding phase of the droplet, its morphology is similar to that of a bounce; however the droplets merge while recoiling.

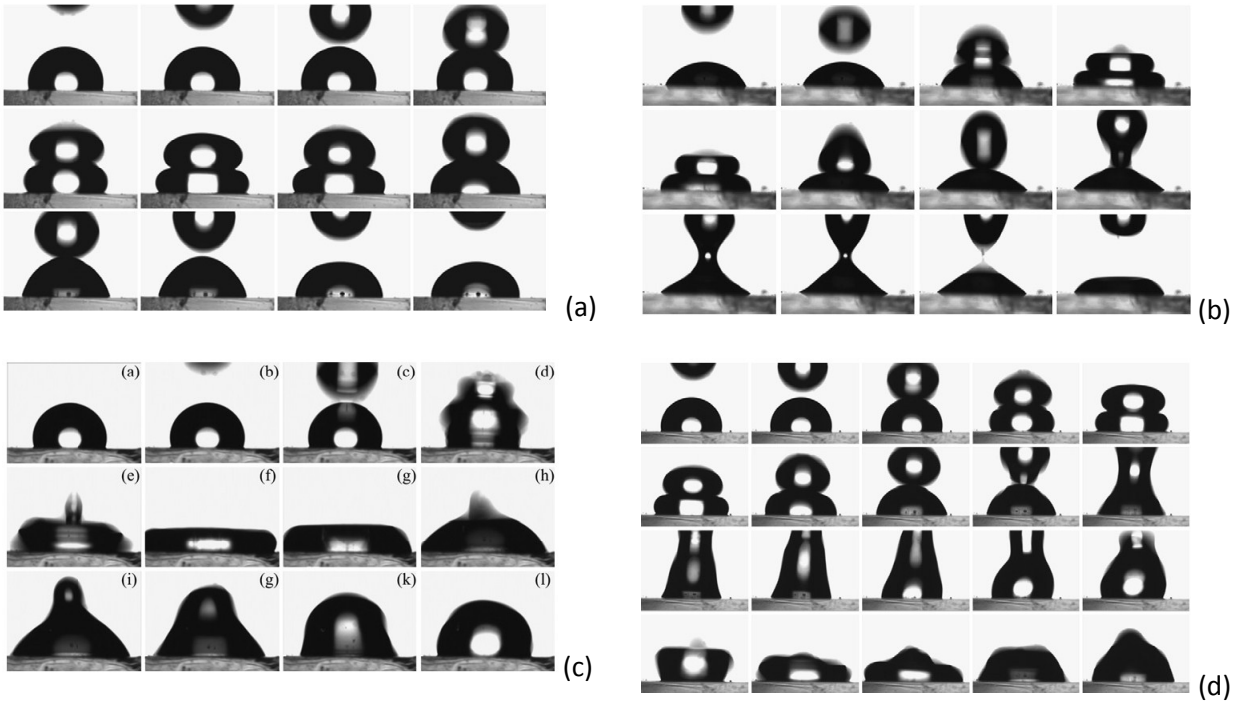

Figure 15: Regimes of droplet coalescence presented by Wang et al. [81] (a) bouncing, (b) conglutination with separation, (c) merging,(d) conglutination with merging.

1.5.3 Analytical work related to merging droplets

Analytical investigations into the spreading of droplets coalescing in air have been investigated by both conservation of momentum [66], [82] and conservation of energy approaches. [14], [15], [17], [83], .The use of conservation of momentum was focused on high inertia situations, where the droplet can be described by a rim and thin film [66], [82]. By using conservation of momentum and mass the evolution of features of the droplet are determined over time. In contrast, the use of conservation of energy is targeted to find thresholds for different regimes such as separation after coalescence [14].

When using conservation of energy approach, the shape and internal flow field of the droplet must be simplified. Figure 16 depicts the various stages of droplets merging and then rupturing. The internal flow field associated with period 1 in Figure 16 is shown in Figure 17. Notation was adjusted to reflect to nomenclature throughout the rest of the text. To determine the amount of energy lost a quasi-steady state analysis is performed, similar to the approach of single droplet impact, where the time of

dissipation, velocity field and volume of associated dissipation are required. For the merging droplet, the volume of dissipation and the velocity field are both determined by equating the dynamic pressure of the droplet to the shear stress needed to convert the axial velocity to radial velocity. The strain rate in the region of dissipation should be comparable to U_0/b resulting in a shear stress of $\mu(U_0/b)$. By equating this shear stress to the dynamic pressure, $^1/_2\,\rho {U_0}^2$ the thickness of the merging region is determined as $2\mu/\rho U_0$ [14].The time required for this spreading was approximated as D_0/U_0. These assumptions result in the following expression for viscous dissipation,

$$\phi \sim \mu\left(\frac{U_0}{b}\right)^2 \left(\frac{1}{4}\pi b {D_0}^2\right)\left(\frac{D_0}{U_0}\right) \sim \frac{1}{4}\pi\rho {D_0}^3 {U_0}^2 \tag{5}$$

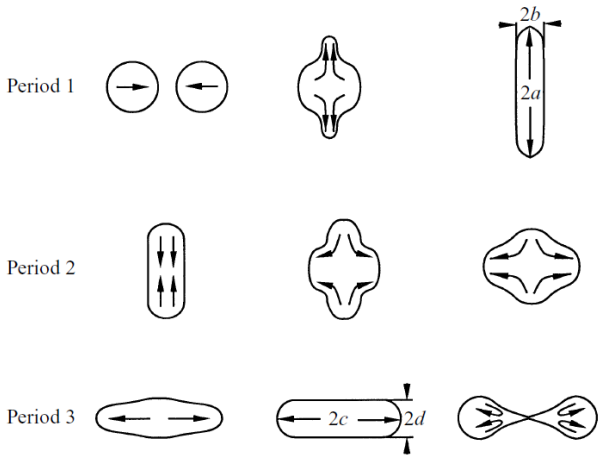

Figure 16: Schematic of the three periods of droplet coalescence and separation from Jiang et al. [14].

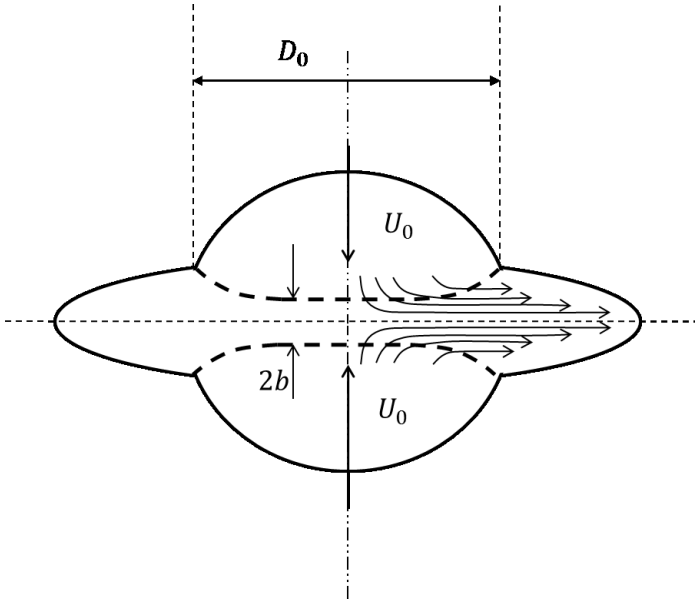

Figure 17: Schematic of viscous dissipation from Jiang et al. [(14)].

It is interesting to note that based on the analytical model, the losses do not explicitly depend on the viscosity of the fluid, which agrees with the experimental results [(14)] . This approximation was not used to determine the losses, but to understand the important parameters. In order to determine the actual amount of energy lost during the spreading phase, Jiang et al. [(14)] assumed the shape at maximum spreading was ellipsoidal and compared the surface energy of the ellipsoid that the initial kinetic and surface energy of the droplets. By correlating the final and initial surface energy, it was revealed that roughly half the kinetic energy is dissipated during spreading, which corresponds to roughly a third of what the above approximation corresponds to. One method to alleviate this discrepancy would be to assume the time required corresponds to R_0/U_0 as opposed to D_0/U_0, which allows for a closer approximation to what was unveiled in the empirical results.

1.6 Objectives

This study aims to delve into the understanding of droplet coalescence using predominantly experimental analysis and enhancing the understanding by developing analytical models. Specifically, this study will explore what occurs when a second droplet impacts an initially sessile droplet resting on surfaces ranging from hydrophilic to hydrophobic and ultimately superhydrophobic. The task at hand can be categorized into the following.

- Provide a qualitative understanding of the effect of surface wettability, droplet size, offset and droplet speed on the morphology of coalescing droplets.
- Quantify the coalescence behavior and develop correlations relating the maximum spreading of the merged droplet to the impact parameters.
- Study the effectiveness of water repellency of superhydrophobic surfaces under coalescing conditions.
- Examine bouncing and delayed merging, caused by micro/nano air films on the coalescence mechanics at low Weber numbers.

1.7 Thesis organization

- **Chapter 2** will present the hardware and techniques used. The required equipment of the experiments consists of a droplet generator, some synchronization electronics, a high speed camera, lighting and a frame to hold these components together. The techniques used to perform the experiments relate to the positioning of the pieces of equipment and the parameters used. Furthermore, the image processing techniques are discussed.

- The results related to the effect of wettability are presented in **Chapters 3** and **4**. To begin the discussion, **Chapter 3** presents the general merging, spreading and recoiling behaviour of droplets merging for the case of a head-on impact. The maximum spreading diameter is modeled using conservation of energy for head-on impact. Furthermore, **Chapter 4** studies the effect of offset for all surface presented. In order to quantify the behaviour across all surfaces a regression model is proposed to unify the previously mentioned impact parameters. This model covers both the merging dynamics for hydrophilic to superhydrophobic surfaces with various offsets.

- Superhydrophobic surfaces are the focus of **Chapter 5**, where the induced detachment of coalescing droplets is presented. The effect of spacing, droplet size and droplet velocity on droplet morphology, spreading and detachment are studied experimentally. Detachment is quantified based on the contact time and restitution coefficient.

- **Chapter 6** presents an interesting phenomenon, that has been seen in various forms in literature: droplet bouncing. The current works furthers this understanding by supplying, more details regarding the temporal morphology; presenting common points between bouncing and non-bouncing droplets; and studying the effect of offset.

- Results of the previous chapters are summarized and discussed in **Chapter 7.**

- Observations related to large offsets and delayed merging are presented in **Chapter 8**, to give the reader potential future research topics related to droplet coalescence.

2 Methodology

The images of deforming droplets are obtained through the use of high speed photography. This section will discuss the experimental apparatus, image processing used, substrates studied and error estimation. The development of this setup could be seen as a first step in the continued success of Concordia's Multiphase flow lab related to the study of droplet impingement.

2.1 Experimental apparatus

2.1.1 Droplet generator

In order to produce droplets for experimentation, the droplet must be generated in a controlled way that is synchronized to the high speed camera. The current work uses a controlled flow: a droplet is formed at the tip of syringe by momentarily allowing the liquid to flow through a solenoid valve. As liquid flows through the solenoid valve, the droplet swells until it is large enough for gravity to overcome surface tension, which will cause it to detach from the needle and fall to the substrate. If the timing and flow rate are correct, the solenoid valve closes and no other droplets are generated. A pressurized water tank drives the flow of water. The size of the droplet generated depends on the size of the syringe's diameter. In order to control the solenoid valve, a function generator and solid state relay were used. When the solenoid valve is charged, it is in the open position. The relay is used to control interrupt current flow from a 12 VDC source: when the relay receives a pulse from the function generator, it closes the switch allowing current to flow to the solenoid, which in turn opens the valve. In addition to controlling the solenoid valve the function generator sends a pulse to the high speed camera, signalling it to begin recording. This setup is schematically represented in Figure 18. The velocity of the impinging droplet is varied based on the height the droplet falls from. Table 2 presents a summary of the droplet sizes and speeds for 534 runs. These cases involved the use of three different syringes while held at five different heights (10, 20, 30, 40 and 50mm). The table attests to the repeatability of the droplet size. Droplet size is based on the height and width of the droplet. Velocity is based on the average height of the droplet between successive frames.

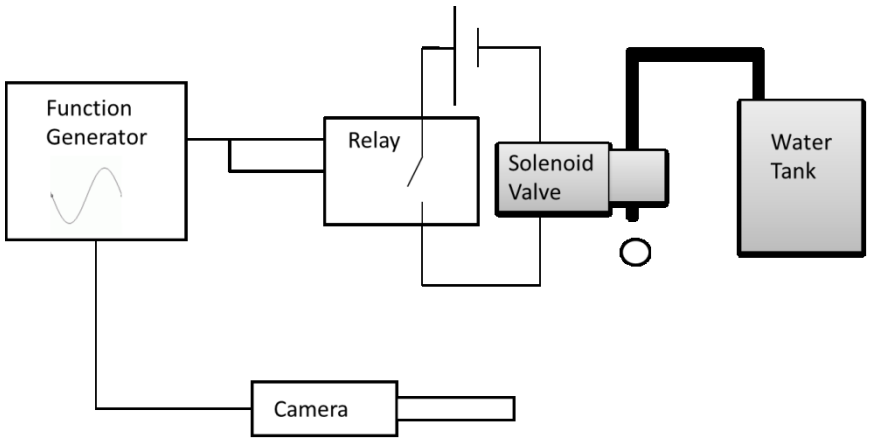

Figure 18: Schematic of droplet generator and synchronization

Table 2: Droplet properties.

Diameter (mm)			Velocity (mm/s)		
Mean	**Standard Deviation**	**Number of Runs**	**Mean**	**Standard Deviation**	**Number of Runs**
3.64	0.15	145	622	16	8
			673	45	44
			709	46	35
			876	68	9
			932	27	49
2.58	0.07	290	583	33	45
			733	30	123
			848	21	55
			961	37	53
			1015	21	14
2.27	0.06	99	603	27	46
			808	24	23
			948	15	30

2.1.2 High speed imaging

The coalescence of droplets is a dynamic process and many important features occur in a small time frame, for example the droplet reaches a maximum spreading in less than 10ms and by 100ms the wetted length reaches a steady state. For successful high speed imaging, there are two major components, the camera and the light source. Lighting is a very important issue, since low exposure times and high magnifications decrease the illumination experienced by the camera sensor. When using microscope lenses, illumination is even more of a challenge. In addition, slight oscillations of objects at high magnification are very noticeable. As will be discussed throughout the coming sections, the full capacity of the equipment was not used, but should the reader be interested in continued experimentation with this equipment, some discussion of possible improvements are presented.

2.1.2.1 Camera used

The camera used to record images of the droplet dynamics is a Photron SA1.1 (Photron, California USA) high speed camera. For detailed explanation to its function the users should refer to the manual [84]. When using any high speed camera, the two major parameters are the frame rate and the exposure

time. The frame rate is the frequency of recording images, while the exposure time, or shutter speed, is the period of time during which the camera's chip records light. The main compromise associated with increasing the recording rate relates to limitations in data speed transfer. At higher speeds, only sections of the camera chip can be saved quickly enough. Memory limitation also reduce the period of time recorded when recording at higher rates, though this may be somewhat offset by recording a smaller section of the camera chip. Recording at a higher frame rate will increase the smoothness of a series of images. Decreasing the exposure time will decrease the blurs associated with the motion of the object, at the expense of brightness. An example of works with a too large exposure time is seen in Figure 15. The recording rate was slow enough to use the full resolution of the camera sensor.

2.1.2.2 Optics

A Navitar UltraZoom 6000 lens (Navitar, New York USA) is used throughout the experiments presented [(85)]. This lens is modular and can be easily upgraded to achieve even higher magnifications. All details related to performance and assembly and are mentioned in the brochure, but are briefly summarized here for the reader's convenience. Using a 105mm macro lens provides comparable magnification to what was used in the current study, but is capable of better illumination.

Criteria used to assess the performance of the lens, the definition of the criteria and the ability of the UltraZoom 6000 are presented in Table 3. Required illumination of a lens is associated to the aperture. Two scales of measurement exist, F-number and Numerical Aperture. F-number (F#), or focal ratio is the ratio between the focal length of a lens to the diameter of the lens [(80)]. Large F# lenses require more illumination. Aperture of a lens could also be presented based on the Numerical Aperture (N.A.), which is standard for microscopy. N.A. relates to the angle light makes with the viewing axis [(81)]. Equation (6) relates two different scales of aperture, the F# to N.A. The aperture and depth of field are linked to each other: increasing the aperture decreases the depth of field. The relation between aperture and depth of field is presented in equation (7). For the experiments performed, it was found that a fully open aperture was the most desirable option for the profile of the droplets, while a more closed aperture was preferred for the angled view of a droplet; however a decrease in shutter speed was required for the angled view, to compensate for the decrease in light that would reach the camera chip. A greater depth of field was required for the angle view in order to capture the features of the droplet. In contrast, capturing the profile theoretically requires no depth of field, since only the information of one plane is required.

Table 3: Lens performance

Criteria	Description	UltraZoom 6000 configuration performance
Working distance	The distance from the tip of the lens to the viewed object required, to allow for the object to be in focus	113mm
Magnification	The ratio between the size of the object on the camera chip to the actual size	1.05x – 6.75X
Depth of Field	The distance between two planes normal to the camera, outside of which a sharp image is not possible	1.73-0.18 mm
Aperture	Ratio between focal length and minimum diameter of tube. Relates to both depth of field and amount of light let in.	Scales vary. NA# 0.017-0.053,

$$F\# = \frac{1}{2\,N.A.} \tag{6}$$

$$Depth\ of\ field = \frac{0.0005}{N.A.^2} \tag{7}$$

2.1.2.3 Lighting

In order to illuminate the droplet impact process, an LED light with a fiber optic bundle is used (Schott, California USA) [88]. The major benefit of this product is the fiber optic bundle, which allows light to be transmitted away from the actual light engine; this allows increased flexibility of the usage of the product and allows the light to be emitted in the area of interest, while the heat is dissipated at the light engine itself. The LED used has the optional feature of strobing, which was not used, but should be considered for future use. By supplying 30VDC power instead of 24VDC, it is possible to strobe the light source, yielding flashes of light more than twice the brightness that can be delivered in continuous lighting mode. The drawback is the maximum rate of these flashes is 1000Hz, and the rate at full light intensity is less [89] . A practical use for the strobing function was not used, but future researchers should check for its applicability to their work.

Two light and camera arrangements were used, one with the light behind the droplet allowing for the profile of the droplet to be seen and the other an inclined or top view allowing the free surface to be observed. When placing the light directly in face of the camera to observed the shape of the droplet should be referred to as back lighting (sometimes mistakenly referred to as shadowgraphy) and placing the light alongside the camera is considered as front lighting. When performing back lighting experiments, the light from the LED enters the lens directly, allowing for a brighter image, as opposed to the case of front lighting, where light is reflected from the object, and then enters the camera. Front lighting would require a brighter light than back lighting to achieve a similar exposure time.

2.1.2.4 Summary of camera and lens features used

The parameters used for the cases of front lighting and back lighting are summarized in Table 4. Should the reader be interested in pursuing further experimentation, it is wise to review the previous section and the associated hardware manuals in order to make a well informed decision, other than blindly following the contents of the table.

Table 4: Summary of recording parameters

Parameter	Back lighting	Front Lighting
Frame Rate	5400 fps	2000 fps
Exposure Time	1/50 000 s	1/4000 s
Aperture	Fully open	Mostly closed
Camera chip resolution	1024 x 1024 (full resolution)	1024 x 1024 (full resolution)
LED intensity	100%	100%

2.1.3 Layout and frame

Two styles of imaging are used, a back lighting technique to yield the profile of the merging droplets and a front lighting arrangement to display the free surface in more details. Sketches of the back lighting and front lighting layouts used are shown in Figure 19 and Figure 20, respectively. An isometric view of the camera being mounted horizontally and angled is show in Figure 21. The camera, droplet generator, light source and substrate are all mounted together on a breadboard and optical bench. To vary the droplet velocity, the droplet generator is fastened on a horizontal beam of adjustable height as seen in Figure 21. Support beams which hold up the structure are supplied by 80/20. Fastening all components securely on a breadboard damped any vibrations from the room, preventing the relative position between the droplet, substrate, camera and light to be disrupted. In addition, the substrate being securely fastened to the bread board allowed the sessile droplet to be accurately displaced by using a micrometer driven stage.

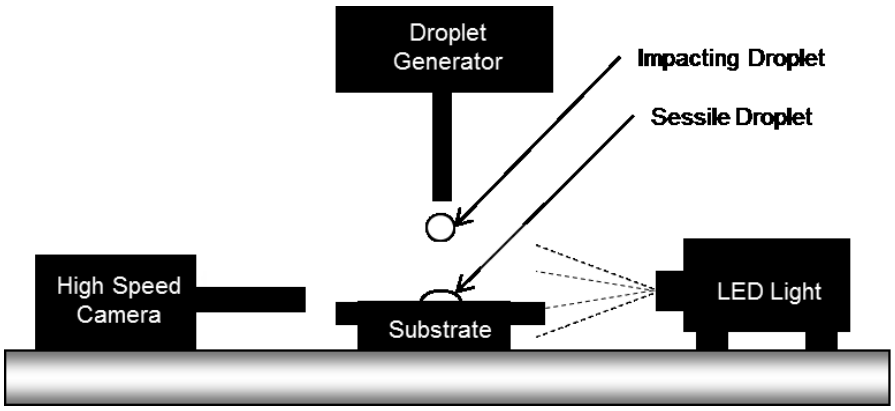

Figure 19. Schematic of the experimental setup for back lighting.

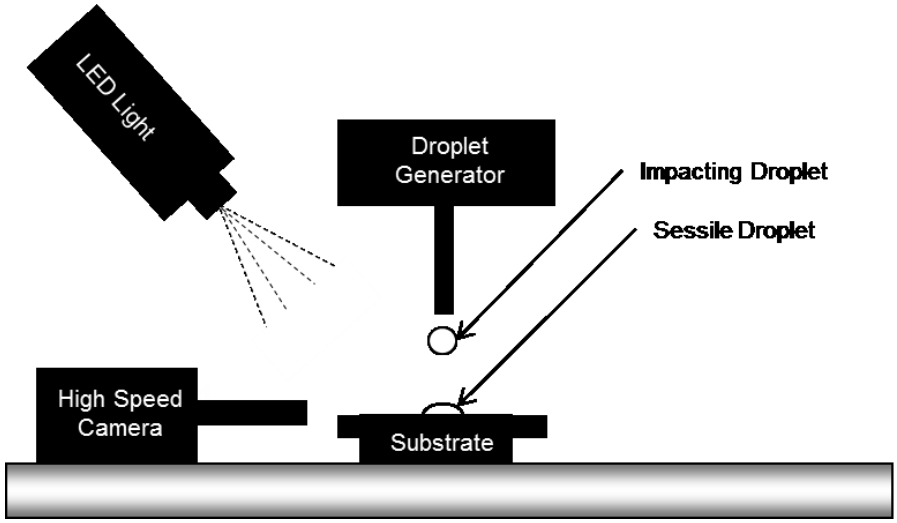

Figure 20: Schematic of angled view with front lighting.

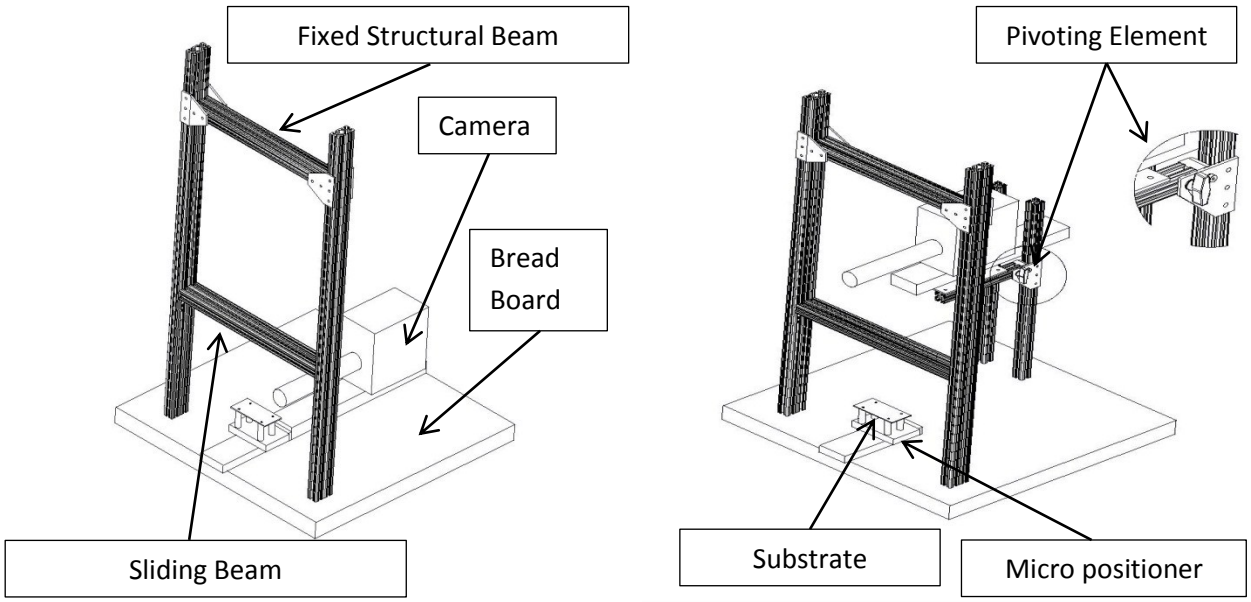

Figure 21: Schematic of frame, substrate and camera mount on breadboard for angled view setup.

The sessile droplet was deposited by the droplet generator then allowed to come to rest, before being displaced by the micro-positioner. When performing experiments on a superhydrophobic surface, the optical bench was highly important, since the droplet is highly mobile and can slide along the surface readily, should it have an inclination of a few degrees. Furthermore, the droplet rebounds from the superhydrophobic surface. To remedy this, a laser pointer was used as reference to align the droplet with the original point of impact. The droplet was easily displaced on a superhydrophobic surface by gently dragging it with a syringe. Once realigned, the droplet was displaced using the micro positioner.

2.2 Image processing

In order to obtain quantitative values or droplet shape and spread diameter, MATLAB image processing toolbox was used. Image processing is an extensive domain, and only a minor part of its capacity was used throughout these works. The major use of the use of MATLAB, was to automate the measuring of the hundreds of thousands of images of droplets recorded by the high speed camera; and collect this data in an organized fashion for interpretation. In terms of actual image processing, the functions used include brightness adjustment, conversion to binary and boundary tracking. The script developed also includes the removal of the background image as well as features used to identify the falling droplet, the impinging velocity, spread diameter, size and contact angle.

Background removal was done by comparing the actual image to a background image recorded after the removal of the merged droplets. Based on the comparison a new image, which ideally only shows the

droplet, is created. The light intensity of each individual pixel of the recorded image is compared to the intensity of the background image. If the light intensities are within 2% of each other, i.e. a difference of 5 out of 256 counts, that pixel is assumed to be part of the background and the corresponding pixel in the new image is assigned a numerical value equivalent to white (typically 256), if not, the new image is assigned the pixel value of the recorded image. Typically, the use of background removal is excessive for well-lit images and images with reflective substrates. It was found that the light capacity was sufficiently strong for the current study to have well-lit images; however, surfaces such as WX2100 relied heavily on the background removal near the contact line. Figure 22, shows a raw image, an image with the background remove and the traced boundary. When comparing series (a) and (b) in Figure 22, the reader should note that the substrate has been removed from the image. The newly created image is then converted to a binary image and the boundaries traced and stored as arrays. These arrays are then used to measure the size of the geometry of the droplet(s). In order to determine the size of the actual size of the droplets, the size a pixel represents is required. The image is calibrated by recording the size of a sapphire washer of known size. The diameter of the nozzle is 1.99mm and was measured using a vernier caliper.

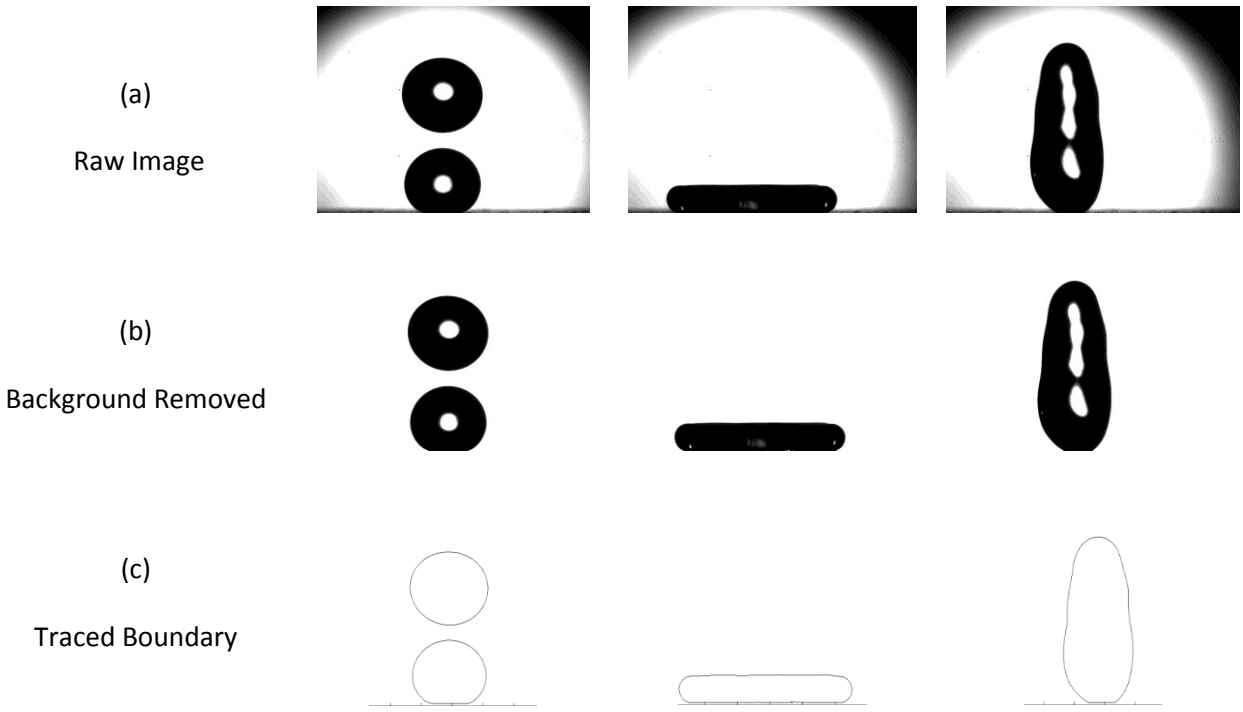

Figure 22: Example of background removal and boundary tracking on a superhydrophobic surface. The a) raw image, (b) background removed image and (c), the traced boundaries at three instances: prior to impact, maximum spreading and nearly detached state.

Converting a grayscale image to binary is done by setting all light intensities above a threshold to white (1) and all those below that threshold to black (0). In order to approximate the error associated with conversion to binary, the 50% threshold is compared to using a 90% and a 10% threshold. Figure 23 compares the effect of the different thresholds for binary conversion. The gray zone in image (b) of Figure 23 shows the region that is considered to be a droplet if a threshold between 10% and 90% is used. This region is roughly five pixels in size which could be considered as a pessimistic uncertainty associated with converting an image to binary.

(a) Raw Image (b) 90% and 10% Thresholds (c) 50% threshold

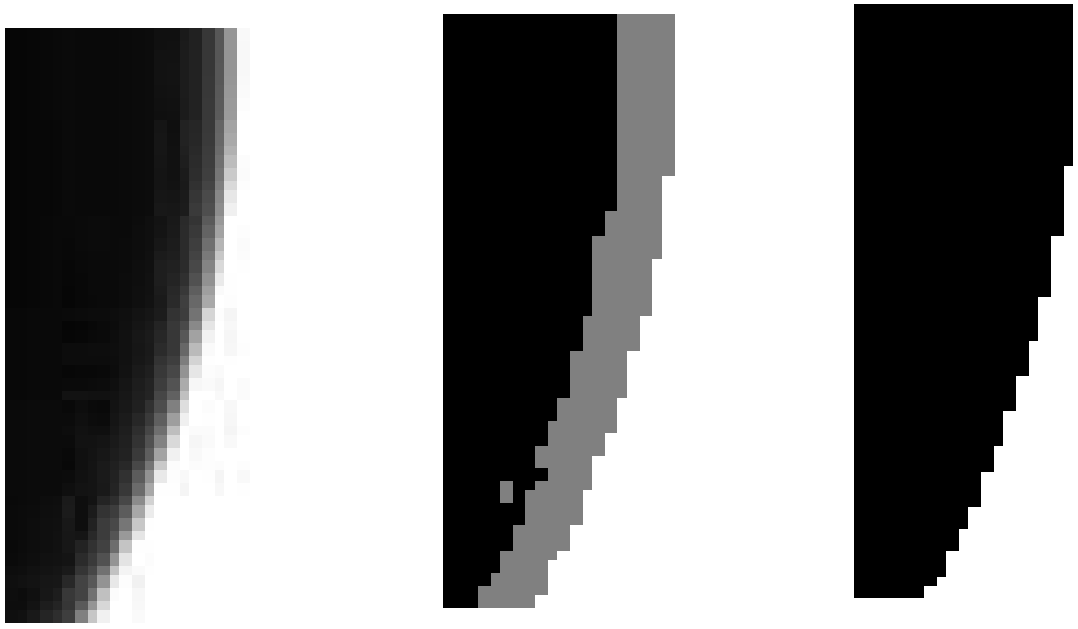

Figure 23: Binary conversion in detail

2.3 Substrate characteristics

Five different substrates were used for experimentation in this work: aluminum, Teflon, aluminum coated with Fluoropel, Teflon sanded with 320 grit sand paper and aluminum coated with WX2100. Both the aluminum and Teflon were purchased from McMaster-Carr (USA). Virgin Electrical Grade Teflon® PTFE was used. Hydrophobicity was enhanced on the aluminum substrates by coating with either Fluoropel or WX2110, available from Cytonix (Maryland, USA). The WX2100 is a spray on solution while the Fluoropel is applied by dipping. Spin coating and spraying are also possible for the Fluoropel, should the hardware be readily available. Lastly, the Teflon's wettability was decreased by increasing its roughness. The wettability of each surface is summarized in Table 5, by presenting the static, advancing and receding contact angles. Furthermore, if the droplet exists as either a smooth, wenzel or cassie state is also presented in Table 5 and the reasoning for these assertions is the following sections. Approximately ten measurements were performed per value.

Table 5. Surface properties.

Material	Static	Advancing	Receding	State
Aluminum	73° ± 3°	90° ± 5°	50° ± 5°	Smooth
Teflon	93° ± 3°	108° ± 5°	71° ± 5°	Smooth
Fluoropel	108° ± 3°	121° ± 5°	86° ± 5°	Smooth
Teflon320	135° ± 3°	151° ± 5°	108° ± 5°	Wenzel
WX2100	154° ± 3°	162° ± 5°	148° ± 5°	Cassie

2.3.1 Smooth surfaces

The aluminum surface used is 5052 and has a #8 Mirror finish; it is quoted as having a roughness in between Ra 4-8 microinches[(90)]. Typically such a smooth surface is produced by extensive honing and lapping [(91)].Both the aluminum and the aluminum coated with Fluoropel are understood to behave based on this roughness number. Since a precise morphology is not known, it is assumed based on the contact angle hysteresis and the low roughness, that the droplet behaves as smooth state, as shown in Figure 6.

2.3.2 Rough surfaces

Two rough surfaces were used; Teflon sanded with 320 girt sandpaper and WX2100. Teflon was sanded using 320 grit sandpaper based on the works of Nilsson et al. [(92)] to create a surface with a large advancing contact angle and large hysteresis, hence a surface with good repellency and low mobility. According to the works of Nilsson et al. [(92)] who performed SEM on their prepared surfaces, sanding Teflon with 320 grit sandpaper resulted in a surface with an RMS roughens of 11 um (or 433 micro-inch), which is comparable to a roughness of 450 µinch on the Ra scale [(91)]. Based on the contact angle hysteresis and the increased roughness, the sanded Teflon likely behaves in a Wenzel state. WX2100 is a spray consisting of a hydrophobic resin and micro particles. The resin itself is comparable to Fluoropel and the micro particles increase the roughness, allowing the surface to be superhydrophobic. Qualitatively Figure 24 shows that the droplet should behave in a Cassie state, since the ratio between spacing to feature size is much less than one[(22), (93), (94)].

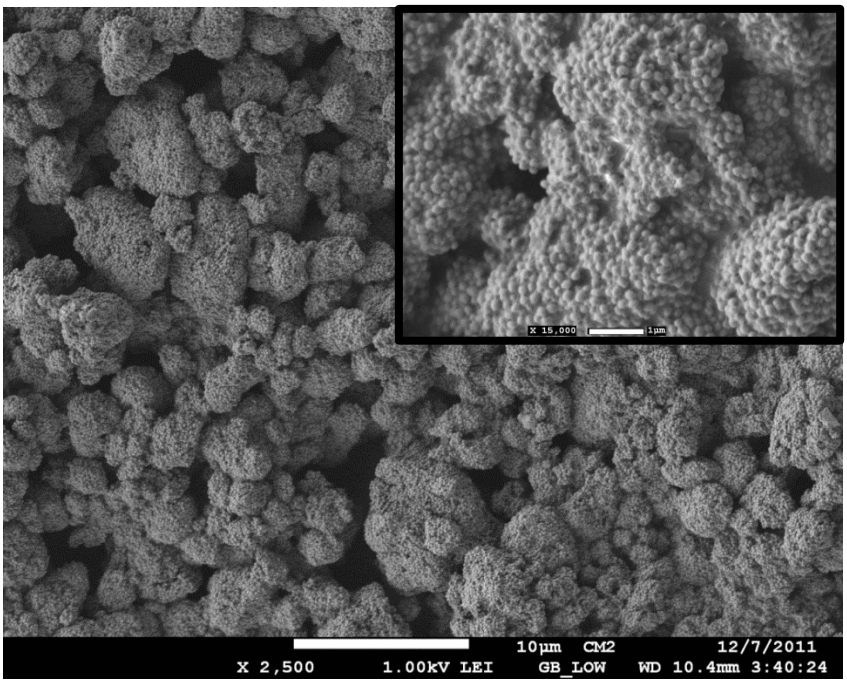

Figure 24: SEM micrographs of the tested superhydrophobic surface. The insert picture shows the micro particles in detail. [94]

2.4 Dimensionless terms

This section outlines some important dimensionless terms used throughout the subsequent chapters. These terms are summarized in Table 6. The two fundamental dimensionless terms are the Reynolds and Weber numbers, which measure the inertia to viscosity and surface tension, respectively. Spacing and spreading are non-dimensionalized similar to the works of Li et al. [8] such as *Non-Dimensional Offset* and *Spread effectiveness* which are defined with the help of Figure 25. The definition of *Spread effectiveness* has been a contentious issue among reviewers, despite its precedence in the works of Li et al. [8] *Spread effectiveness* is the result of normalizing wetted length with respect to an ideal length. This ideal length is defined by the summation of the droplet size and length. Scaling with both offset and droplet diameter allows for better comparison between surfaces of different wettability which may have slightly different offsets. When discussing the behaviour on one type of surface and studying only the effect of offset, the *Spread factor* will be used. The *Spread factor* does not account for offset. Time is non-dimensionalized with droplet size and velocity. A new Weber number is defined by replacing the surface tension of the liquid with the liquid-solid interfacial energy. This *Surface Weber number* accounts for the effect of the substrate's wettability and mobility, since the contact angle hysteresis is included.

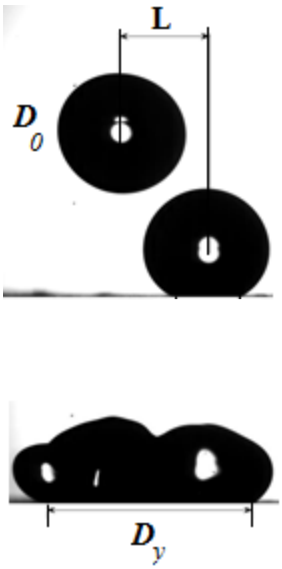

Figure 25: Schematic of merging parameters.

Table 6: Dimensionless terms

Expression	Term
$\lambda = \frac{L}{D_0}$	Non-dimensional Offset
$\xi = \frac{D_y}{D_0}$	Spread factor
$\Psi = \frac{D_y}{D_0 + L}$	Spread effectiveness
$\tau = t\frac{U_0}{D_0}$	Non-Dimensional time
$We = \frac{\rho {U_0}^2 D_0}{\gamma_{lv}}$	Weber number
$Re = \frac{\rho U_0 D_0}{\mu}$	Reynolds number
$We_{SL} = \frac{\rho {U_0}^2 D_0}{\gamma_{sl}}$	Surface Weber number

2.5 Error approximation

Quantities measured from experiments are all based on time and distances. Temporal error is based on the frame rate, which is typically 5400 frames/second; therefore the temporal error is roughly 0.2ms. Effects related to faulty timing of the camera circuitry have been assumed to be negligible. Spatial errors come from any faulty calibration. As previously mentioned, the size of a pixel is calibrated based on measuring an object of 1.99mm; therefore the size of a pixel has a 1% uncertainty. In addition, conversion to binary has an uncertainty corresponding to roughly five pixels, as previously discussed. A droplet is typically 250 pixels in size; therefore this error is roughly 2%. Errors related to measurement of time and space are reduced when non-dimensionalizing, since the calibration errors cancel each other. This is not the case with the Reynolds and Weber numbers.

In addition to measurement errors, repeatability issues are present with the droplet generating system. One source of this error comes from the nature of the droplet generating method. While detaching from the needle, the droplet stretches and becomes somewhat ellipsoidal. Due to this ellipticity at detachment, oscillations are present while it descends towards the substrate and are caused by the droplet attempting to return to a spherical state. These oscillations are a potential source of error when measuring the droplet's diameter. In order to measure the droplet diameter, the average of the height and width is taken in each of the 5 frames prior to impact, and then those five values are in turn averaged. This tactic was used to minimize measurement error associated with droplet oscillations. Oscillations are less prominent in the higher velocity cases, since a greater period of time has elapsed prior to their impact upon a substrate. Smaller droplets are also less prone to oscillations. These oscillations can be viewed as an error or source of non-repeatability of the experimental system; however, their effect will be considered as negligible and will not be discussed. This assumption is likely valid, since these experimental results were used to validate numerical work, in which oscillations and ellipsoidality of the droplet was not considered [(94), (95)]. Lastly, when studying the profile of the coalescence of droplets, it is important to determine if the droplets are both in the same plane, i.e. equal distance from the camera lens. Since the depth of field is 170μm, droplets would appear out of focus if not in the same plane. In order to further scrutinize this, the initial frames of droplet impingement can be investigated to see if the droplet passes behind the sessile droplet without deforming it.

The substrate can present two sources of error, inhomogeneity in morphology and a dependence on temperature and humidity. Inhomogeneity was treated similar to variations in droplet shape during

impingement, by repeated measurement. Variations are presented in Table 5. Experiments were performed at 20°C and a relative humidity of 25 percent. As seen in the works of Yin et al. [96] and Mockenhaupt et al. [97] humidity and temperature can have a significant impact when environmental conditions deviate significantly from standard room temperature conditions. However, these works show that in the range of 30 to 60 percent relative humidity and temperatures ranging from 10 to 30°C the wettability of superhydrophobic surfaces does not show a substantial change.

3 Head-on coalescence of droplets

This chapter presents the fundamental case of a nearly axisymmetric collision of droplet on surfaces of various wettability. Experimental results are presented and an analytical model is proposed to capture the maximum spread diameter.

3.1 Experimental results of head-on impact

An isometric view of the impact of 2.58 mm diameter droplet with an impact velocity of 0.733 m/s, resulting in a Reynolds number of 2020 and a Weber number of 22 on an aluminum substrate with an offset of approximately zero (head-on), is shown Figure 26. The droplet impacts the sessile droplet, merges with it and the resulting axial momentum is transferred into radial momentum causing the merged droplet to expand. During the expansion kinetic energy is dissipated due to viscous effects and the surface forces increase as the droplet deviates from an equilibrium state. The expansion continues until inertial effects have been diminished by viscous dissipation, and can be overcome by capillary effects. Once the surface tension forces are dominant, the droplet then recoils. The droplet should eventually reach an equilibrium shape, if it were kept in the correct environment for an adequate period of time. Humidity, temperature and contaminants would need to be controlled to high precision and it may require hours or days to reach equilibrium. [98] For the experiments performed, defining equilibrium state of the droplet is awkward, since the droplet will ultimately evaporate. Nonetheless, once the droplet's free surface and wetted length are not experiencing any perceivable changes, the droplet will be deemed to be in a static state.

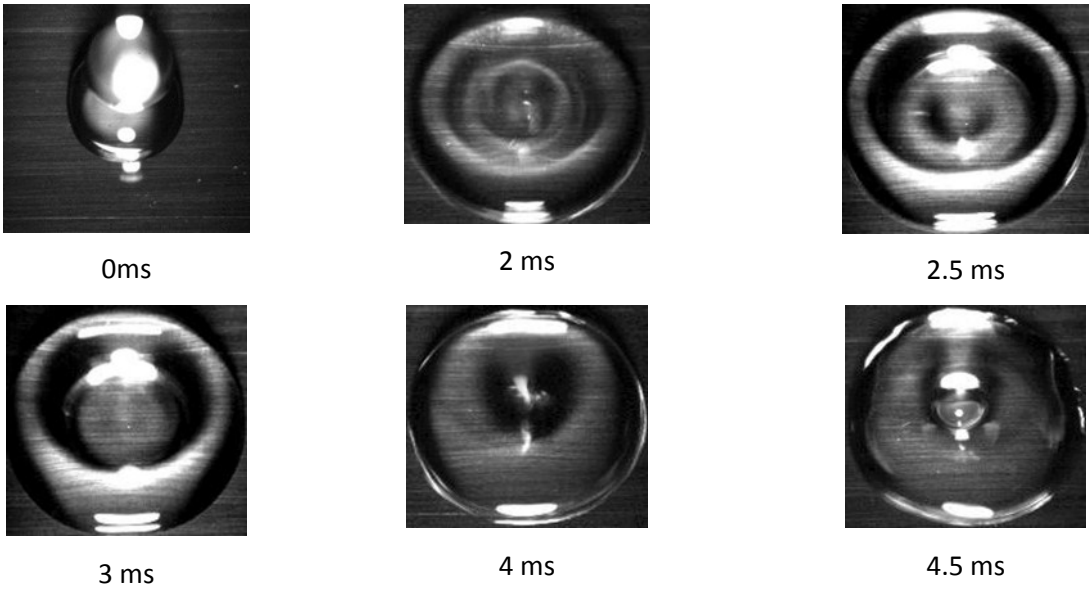

Figure 26: Top View of head-on impact and coalescence of two water droplets, with *We*= 22 and *Re* =2020 on a polished aluminum surface.

By examining Figure 27, the effect of surface wettability can be seen qualitatively by the profiles of droplets of similar size and velocity of those shown in Figure 26. Figure 27 presents cases of droplets

impacting aluminum, aluminum coated with Fluoropel and aluminum coated with WX2100. Teflon and Teflon320, are not shown in the interest of brevity. To complement the qualitative discussion, Figure 28 presents quantitative understanding by showing the spread factor, $\xi = D_y/D_0$, over time. Firstly, the droplets merge and bulge before spreading; the difference in shape between theses surfaces can be attributed to the initial shape of the sessile droplet. The bulge formed in the case of the hydrophilic surface is not as prominent as in the case of the hydrophobic or superhydrophobic case, as seen at times 2.4ms for the aluminum and Fluoropel, and 3.3ms for the WX2100. The droplet then descends to the surface and spreads until it reaches a pancake like shape between 6 and 8ms, the major difference amongst the surfaces is the diameter reached, as seen in Figure 28. As wettability is decreased the spread diameter decreases; in fact, the aluminum surface reaches a spread diameter forty percent greater than the superhydrophobic surface.

A major difference in the behaviour in response to surface hydrophobicity occurs during the recoiling process. The contact line of aluminum remains pinned and the droplet thins near the edges and fills in the center as the contact angle switches from its advancing angle to its receding angle, as seen at 15.3ms after impact. As hydrophobicity is increased the contact line moves more easily and the droplet recoils instead of the edges thinning, as seen for the case of Fluoropel at 13.5ms in Figure 27. Furthermore, the droplet on a superhydrophobic surface recoils much more readily until it reaches an elliptical shape with a vertical major axis at 15.6ms. This discrepancy in recoiling behaviour can be attributed to the large discrepancy in contact angle hysteresis, particularly the receding contact angle. Since aluminum's receding contact angle is relatively small compared to the others, the contact angle changes drastically while the contact line is still pinned, causing a large change in recoiling behaviour, as opposed to WX2100 which has a receding contact angle only 10° less than its advancing angle. More details regarding the detachment which occurs on the superhydrophobic surface are presented in Chapter 5.

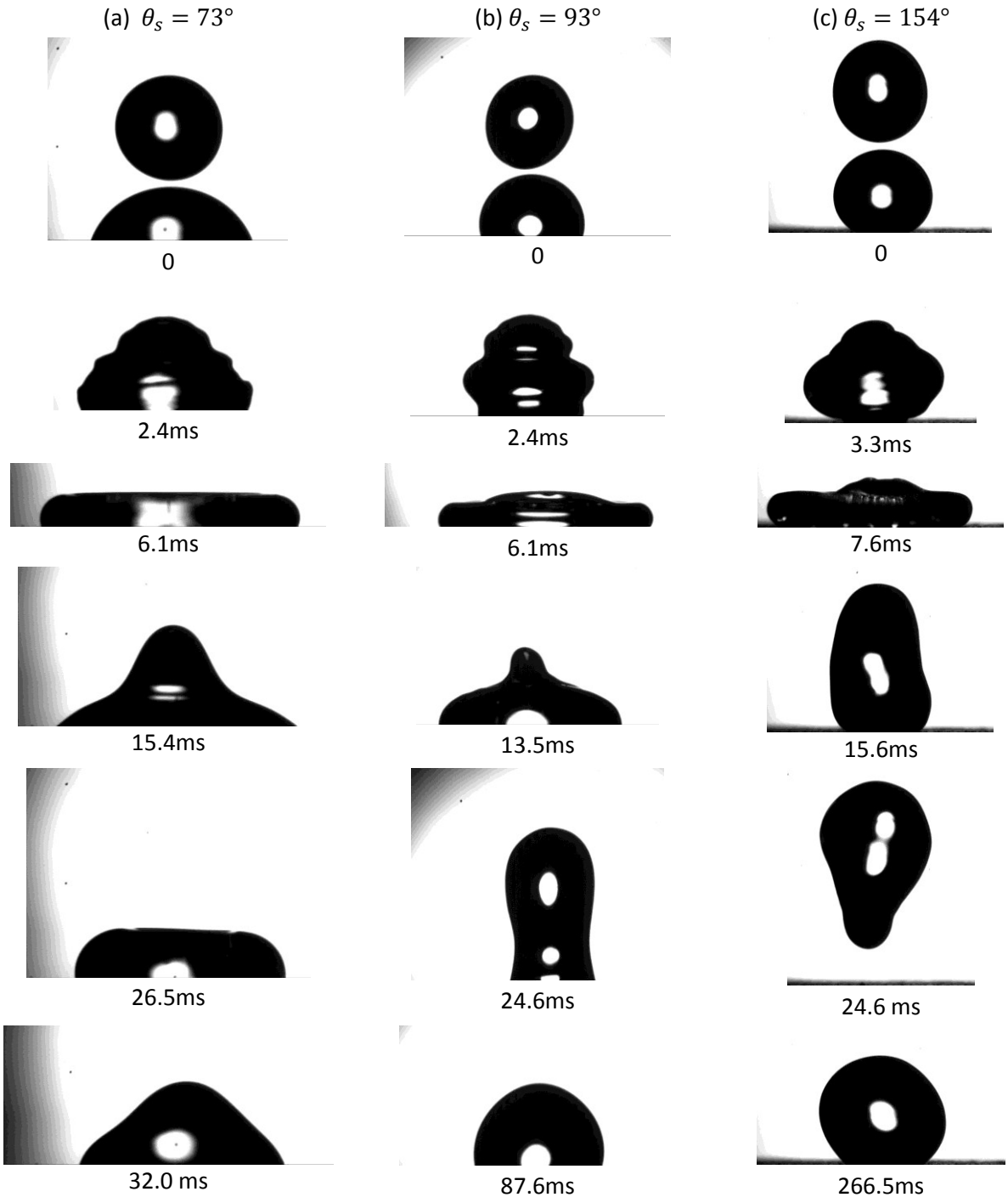

Figure 27: Side view of head-on impact and coalescence with, We = 22 and Re =2020 on (a) aluminum, (b) Fluoropel and (c) WX2100 surfaces.

Figure 28 shows the spreading behaviour of a head-on impact qualitatively. Temporally, it is consistent with the discussion presented regarding kinematic, spreading, receding and equilibrium phases from Rioboo et al. [52]. Firstly, the onset of each impact is similar and the droplet has less spreading for the less wetting cases. With regards to the recoiling, or relaxation phase, as it is referred to in the works of Rioboo et al [52], the five surfaces studied vary substantially. As previously discussed, the recoiling is vastly different. The droplets on Teflon and aluminum recoil to a value similar to their static value, then expand and finally recoil to their static phase. In contrast, Fluoropel and Teflon320 reach a value much less than their static values, then spread and recoil once more until they begin to settle into their static wetted length. Lastly, the superhydrophobic surface and the sanded Teflon do not reach a static spread diameter in the time recorded, as opposed to the aluminum and Teflon which reach a static wetted diameter by 60ms and the Fluoropel in roughly 90ms. Since the droplet on the superhydrophobic surface has detached, it is no longer of interest, since in practical applications it could have been removed from the substrate.

It is important to distinguish between the static wetted length and the static shape. Clearly the droplets which have merged on WX2100 have not reached a static shape by 100ms, as seen by the continued variation in the wetted length. In contrast, the aluminum has reached a constant wetted length by 60ms. The inserts in Figure 28 show the profile of the merged droplet at times of roughly 115 and 130ms; therefore, they have yet to reach an equilibrium shape. The contact angle is seen to change; however, the contact line does not move. The increase in wettability causes the droplet to reach a static wetted length much quicker; however, oscillations in the free surface are still present.

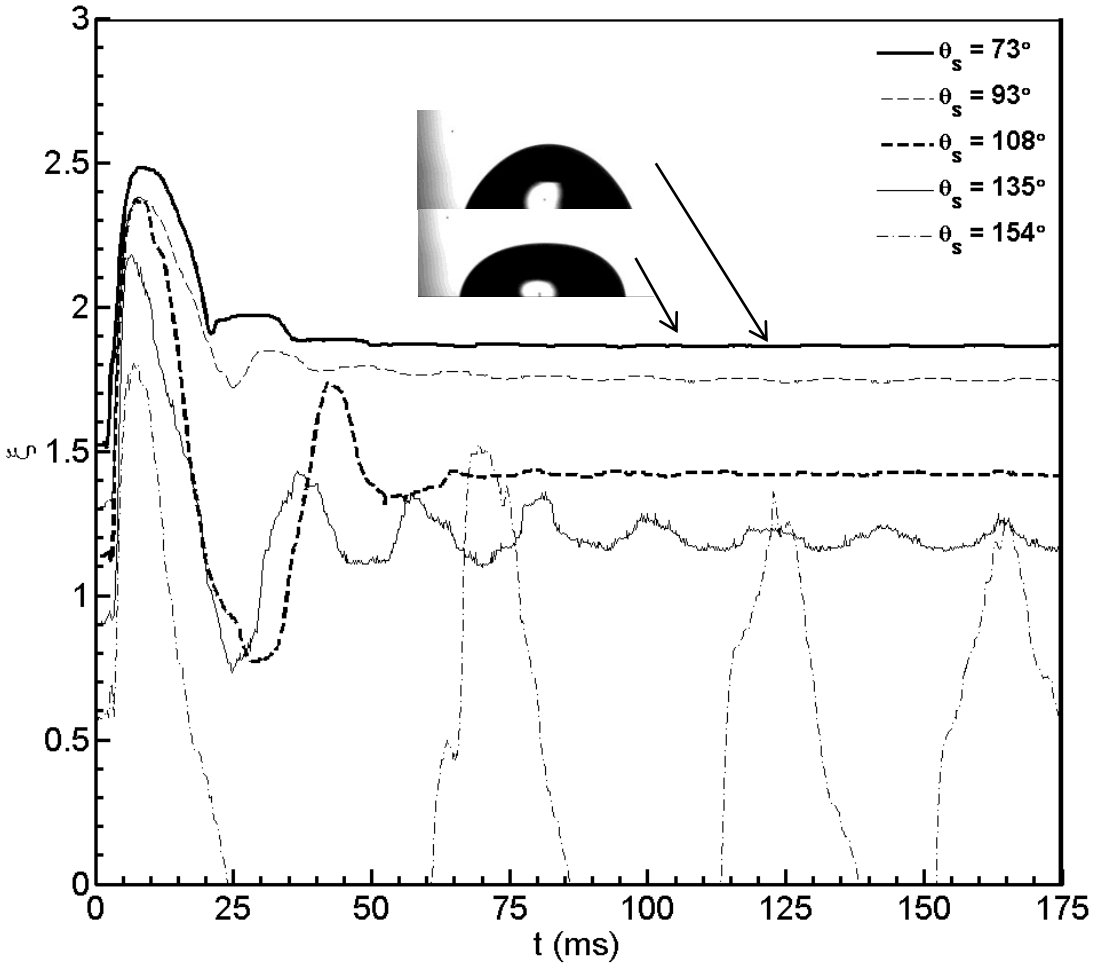

Figure 28: Temporal evolution of spread factor, $\xi = D_y / D_0$, for surfaces of various wettability with an impinging droplet of We = 22, Re = 2020 with head-on impact.

The maximum spreading of the merged droplets is an important parameter since it is of interest to various industrial processes, particularly painting and spray cooling. Figure 29 displays the maximum spread factor, $\xi_{max} = D_{max}/D_0$, as function of Weber number for the five surfaces studied under the head-on impact condition (i.e. $L \approx 0$). Increasing Weber number and wettability both increase the maximum spread length. Amongst the four hydrophobic surfaces, similar behaviour is observed

between Teflon and Fluoropel as well as Teflon320 and WX2100. These pairs of surfaces have similar wettability.

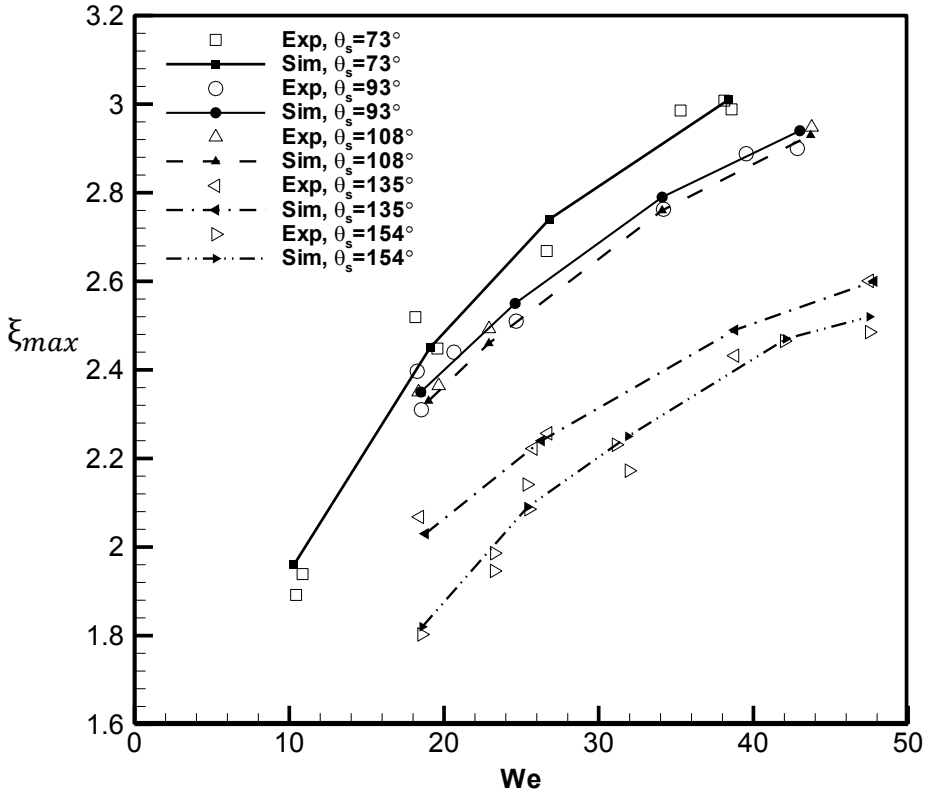

Figure 29: Maximum spread factor, $\xi_{max} = D_{max} / D_0$, for different Weber numbers and surface wettabilities, for $\lambda \approx 0$.

3.2 Analytical model for the prediction of maximum spreading

The proposed axisymmetric model determines the maximum spreading of equal volume coalescing droplets. A conservation of energy approach is used which approximates the viscous dissipation based on a quasi-steady state analysis. Geometry of the initial, final and transient shapes are simplified and the degree to which they capture the phenomena of droplet deformation is validated. The range of Weber numbers studied ranges from 10 to 50.

3.2.1 Approximation of coalescence morphology

The initial state of the system is assumed to be that of a truncated sphere with an angle equivalent to the static contact angle of the droplet on the surface and the final state is that of a cylindrical disk. Both the initially sessile droplet and the flattened disk are assumed to have negligible kinetic energy. The states are depicted in Figure 30.

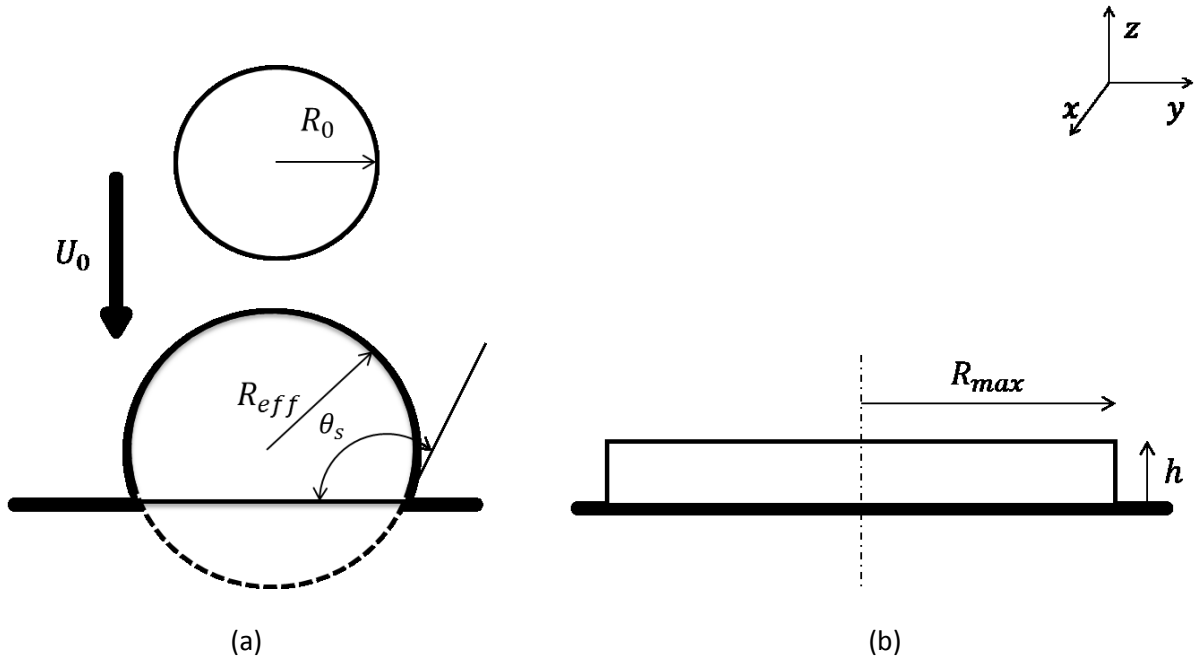

Figure 30: (a) Initial configuration and (b) final state at maximum spreading.

While deforming from the initial state to the final state, the droplets will go through two stages, merging with bulging of the contact region; and spreading along the surface. The merging is shown in Figure 31, during this stage, the droplets merge and a bulge grows radially. Growth of this bulge results in axial momentum being transferred into radial momentum. This bulge continues to grow and the droplet reduces in height until the spreading phase begins. During the spreading phase, the contact line expands

radially and the bulging from the previous phase is not as prominent. Figure 32 depicts the spreading phase, which is assumed to be similar to the spreading phase on the works of Pasandideh-Fard et al. [59]

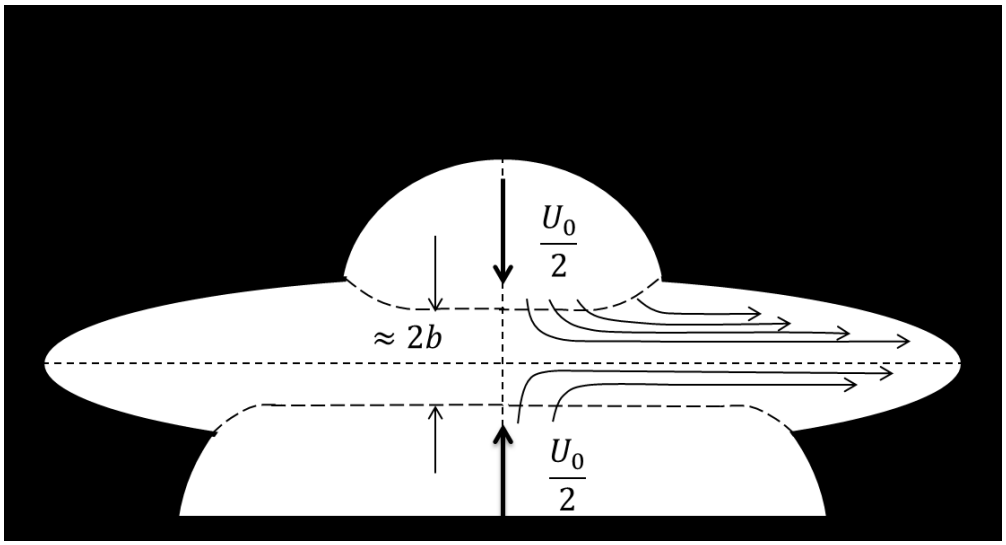

Figure 31: Approximate merging phase of droplets.

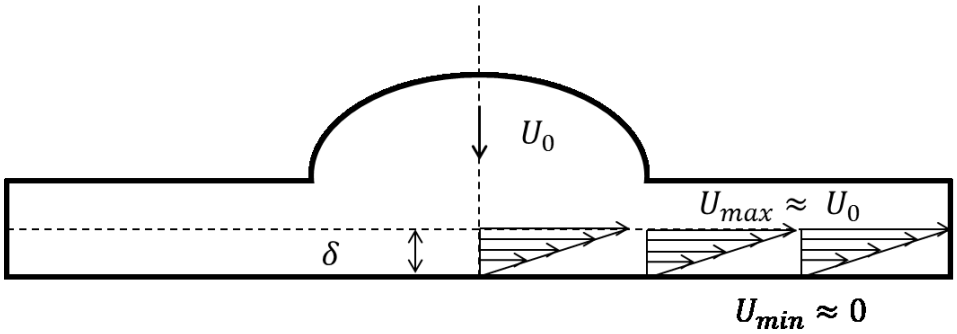

Figure 32: Approximate spreading phase of droplets.

Figure 33 presents the experimental results in the interest of validating the assumed shapes previously presented. In addition, Figure 27 shows a similar behaviour. The three surfaces presented in Figure 33 are aluminum, Teflon and WX2100 with droplet impact conditions of Weber number of 34 and Reynolds number of 2600. By 0.7ms after impact, a discernible bulge is seen which continues to grow up to 1.5ms after impact. This bulge or rim, is highly pronounced in the case of the superhydrophobic surface studied. The similarity of the superhydrophobic case to a case of a droplets merging in a gaseous medium is not surprising, since the sessile droplet closer resembles a sphere due to the high contact angle. By 3ms, the droplet has already begun to spread along the surface and continues to do so until it reaches a shape comparable to a flattened disk near its maximum spreading.

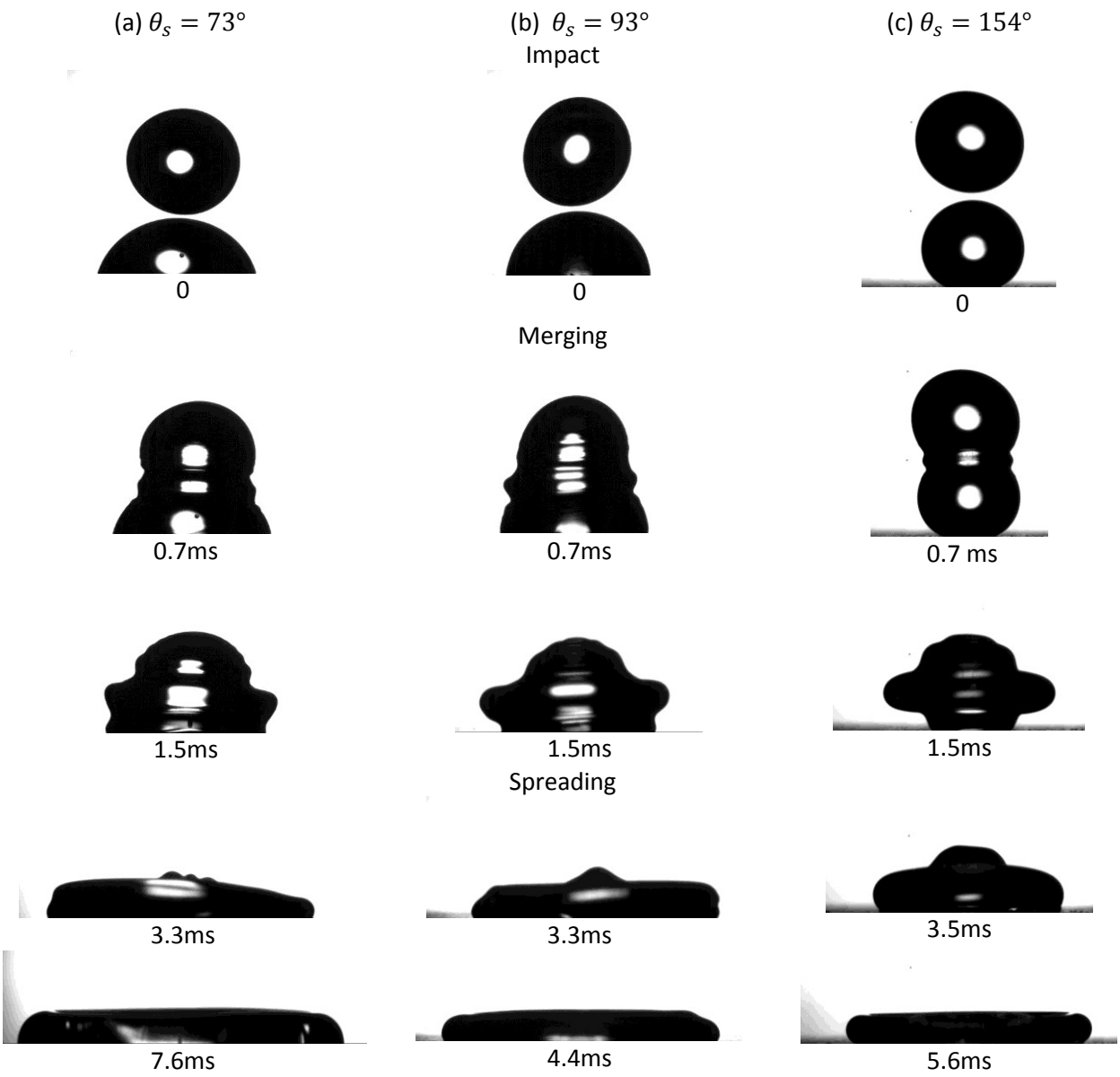

Figure 33: Various phases of droplet coalescence and spreading for We= 34, Re = 2600, for (a) aluminum, (b) Teflon and (c) WX2100

3.2.2 Initial and final states

In order to determine the initial and final surface energies associated with the merging and spreading processes conservation of mass for an incompressible liquid is used. To determine the initial surface area of the sessile droplet an effective radius, R_{eff}, of the truncated sphere which represents the sessile droplet is required. Schematics of the effective radius are shown in Figure 34. The plane of truncation is determined so that the contact angle is equal to the angle between the horizontal and the tangent of

the sphere is equivalent to the static contact angle of the droplet. Derivations of the effective radius and the interfacial areas are presented below.

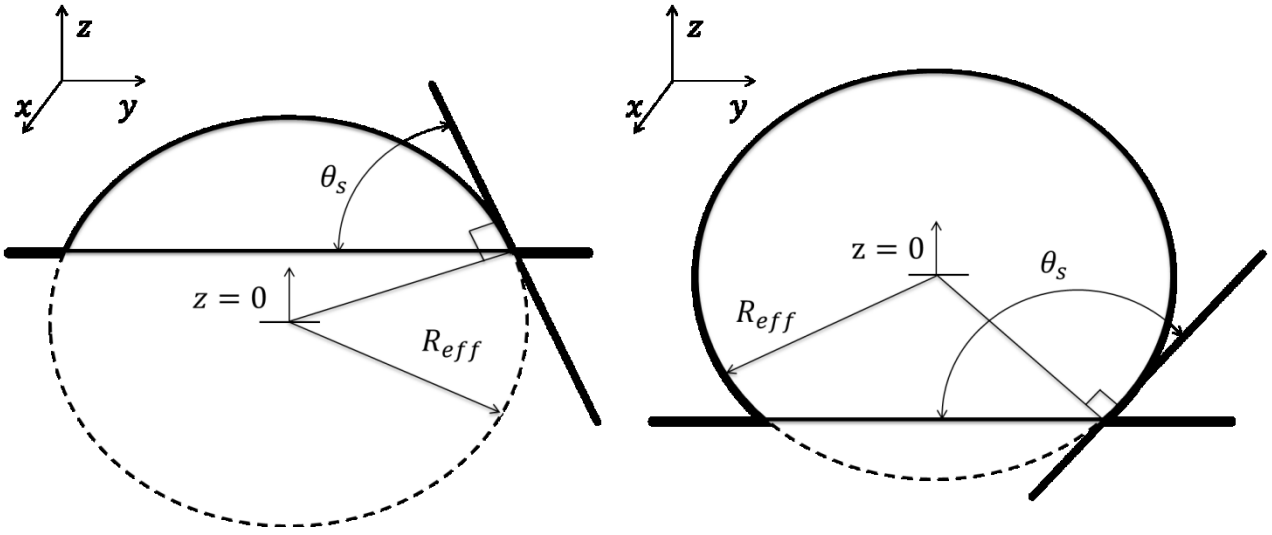

(a) (b)

Figure 34: Approximate shape of a sessile droplet on (a) hydrophilic and (b) hydrophobic.

Hydrophylic

$$\frac{4}{3}\pi R_0^3 = \int_{R_{eff}\sin(90-\theta_s)}^{R_{eff}} \pi\left(R_{eff}^2 - z^2\right)dz \quad (8)$$

Hydrophobic

$$\frac{4}{3}\pi R_0^3 = \int_{-R_{eff}\sin(\theta_s-90)}^{R_{eff}} \pi\left(R_{eff}^2 - y^2\right)dy \quad (9)$$

Results in the following ration between the impinging droplet radius and the effective radius,

$$\frac{R_{eff}}{R_0} = \left(\frac{4}{3}\left(\frac{1}{\frac{2+sin^3(90-\theta_s)}{3} - \sin(90-\theta_s)}\right)\right)^{1/3}$$

$$\frac{R_{eff}}{R_0} = \left(\frac{4}{3}\left(\frac{1}{\frac{2-sin^3(\theta_s-90)}{3} + \sin(\theta_s-90)}\right)\right)^{1/3}$$

Using this ratio we obtain the following initial interfacial area of the liquid-solid (A_{ls}) and liquid-vapour (A_{lv}),

For the hydrophilic case,

$$(A_{ls})_0 = \pi R_{eff}^2 cos^2(90-\theta_s) \quad (10)$$

$$(A_{lv})_0 = 4\pi R_0^2 + \int_{R_{eff}\sin(90-\theta_s)}^{R_{eff}} 2\pi\sqrt{\left(R_{eff}^2 - y^2\right)}dy \quad (11)$$

Which simplifies to,

$$\frac{(A_{lv})_0}{R_0^2} = 4\pi + \frac{\pi^2}{2}\left(\frac{R_{eff}}{R_0}\right)^2 - \pi\left(\frac{R_{eff}}{R_0}\right)^2\left[(\sin(90-\theta_s))(1-\sin^2(90-\theta_s))^{\frac{1}{2}}\right] - \pi\left(\frac{R_{eff}}{R_0}\right)^2 \tan^{-1}\frac{\sin(90-\theta_s)}{\sqrt{1-\sin^2(90-\theta_s)}}$$

For the hydrophobic case,

$$(A_{ls})_0 = \pi R_{eff}^2 cos^2(\theta_s - 90) \tag{12}$$

$$(A_{lv})_0 = 4\pi R_0^2 + \int_{-R_{eff}\sin(\theta_s-90)}^{R_{eff}} 2\pi\sqrt{(R_{eff}^2 - y^2)}dy \tag{13}$$

Which simplifies to,

$$\frac{(A_{lv})_0}{R_0^2} = 4\pi + \frac{\pi^2}{2}\left(\frac{R_{eff}}{R_0}\right)^2 + \pi\left(\frac{R_{eff}}{R_0}\right)^2\left[(\sin(\theta_s - 90))(1-\sin^2(\theta_s - 90))^{\frac{1}{2}}\right] - \pi\left(\frac{R_{eff}}{R_0}\right)^2 \tan^{-1}\frac{-\sin(\theta_s - 90)}{\sqrt{1-\sin^2(\theta_s - 90)}}$$

The final shape is assumed to be a disk with a volume equivalent to twice the volume of either the impinging or sessile droplet; or the sum of the two. The height of this disk is based on the maximum spreading diameter as derived below. Schematically, *h*, the fully spread thickness, is depicted in Figure 30.

$$2\frac{4}{3}\pi R_0^3 = \frac{1}{2}\pi R_{max}^2 h$$

$$h = \frac{16}{3}\frac{R_0^3}{R_{max}^2}$$

Resulting in the following for the liquid-solid and liquid-vapour interfacial areas

$$\frac{(A_{lv})_f}{R_{max}^2} = \pi + \frac{32\pi}{3}\left(\frac{R_0}{R_{max}}\right)^3$$

$$\frac{(A_{ls})_f}{R_{max}^2} = \pi$$

The liquid-solid interfacial energy is calculated based on the contact angle hysteresis using the results of the works of Chibowski. [32],

$$\frac{\gamma_{ls}}{\gamma_{lv}} = \frac{1 + cos^2\theta_A}{2 + cos\theta_R + cos\theta_A} - cos\theta_A \quad (14)$$

The initial potential energy is determined to be the sum of the surface energy of the liquid-vapour interface and liquid-solid interface as seen below.

$$E_{lv0} + E_{ls0} = (A_{lv})_0\gamma_{lv} + (A_{ls})_0\,\gamma_{ls}$$

Kinetic energy is equivalent to the expression below.

$$E_k = \frac{1}{2}\rho\frac{4}{3}\pi R_0^3 V^2$$

At maximum spreading, the kinetic energy is assumed to be negligible and the surface energy comes from the liquid-vapour and liquid-solid interfaces as it does in the initial case. This results in the expression below.

$$E_{lvf} + E_{lsf} = (A_{lv})_f\gamma_{lv} + (A_{ls})_f\,\gamma_{ls}$$

3.2.3 Viscous dissipation

The energy lost during the merging and spreading process is approximated using a quasi-steady state analysis, the simplification for energy lost to viscous dissipation is presented below. The velocity gradient is simplified to a one direction gradient, the time to a characteristic time scale for the event, and the volume to a volume of interest. Using such an approach is common in literature [(14), (17), (53), (55), (63) (64)]. The simplification was first presented in equation (2) and repeated here for convenience.

$$\phi = \int_t \int_V \mu\frac{1}{2}\left[\frac{\partial U_i}{\partial x_j} + \frac{\partial U_j}{\partial x_i}\right]^2 dx^3 dt \approx \mu\Delta t\left(\frac{dU}{dz}\right)^2 V \quad (2)$$

Energy is dissipated during the merging of the two droplets and during the spreading of the resulting mass. During the merging phase, a bulge is formed where the droplets are colliding, while the spread diameter remains constant. The period of time where the droplet has not increased in size is approximated as the merging time, while the total time is labelled as the spreading time. Schematics of the spreading and merging were previously shown in Figure 31 and Figure 32, respectively. It is important to note the bulging disk at the center of the merged droplet and how it compares to that

shape of what is shown in the works of Jiang et al. [14], which motivates the use of a similar approximation for viscous dissipation. The spreading phase is assumed to behave similar to the spreading phase of a single droplet. Experimental results supporting the assumption that the droplet coalescence can be divided into two phases are shown in Figure 33.

The merging and spreading times are approximated based on the droplet size, impact velocity and final wetted diameter. Bulging refers to the phase where the droplets merge and deform without change in the wetted length, whereas the total spreading time includes the time from the contact of the droplets to the time where the droplet is at maximum spreading. From experimental data, the time for the droplet to reach the maximum spreading was found to be constant when normalized with the impact velocity and the final wetted diameter according to equation (15). The accuracy of this relation is shown in Figure 31. This is comparable to what was found for the case of a single droplet in the works of Pasandideh-Fard et al. [55]

$$t_s = D_{max}/U_0 \tag{15}$$

The merging time is approximated as,

$$t_m = R_0/U_0 \tag{16}$$

Figure 36 compares the approximated merging time from equation (16) to the time required for the droplet to begin to increase in spread diameter by two pixels, i.e. one per side. The correlation for total spreading time is more convincing than the approximate assumption for the bulging time. Lastly, it is interesting to note that spreading time is an overestimate, while the merging time is an underestimate.

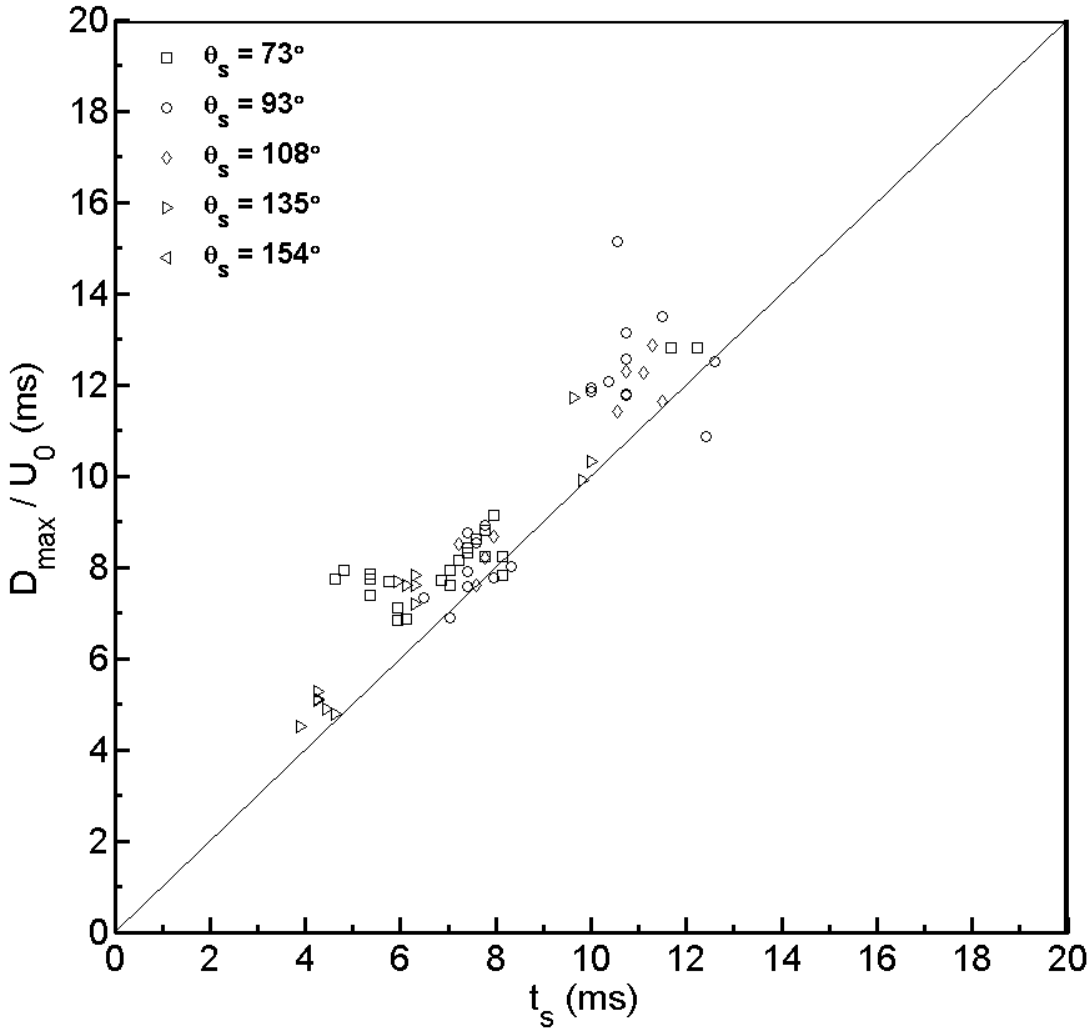

Figure 35: Comparison between the assumed and measured spreading times.

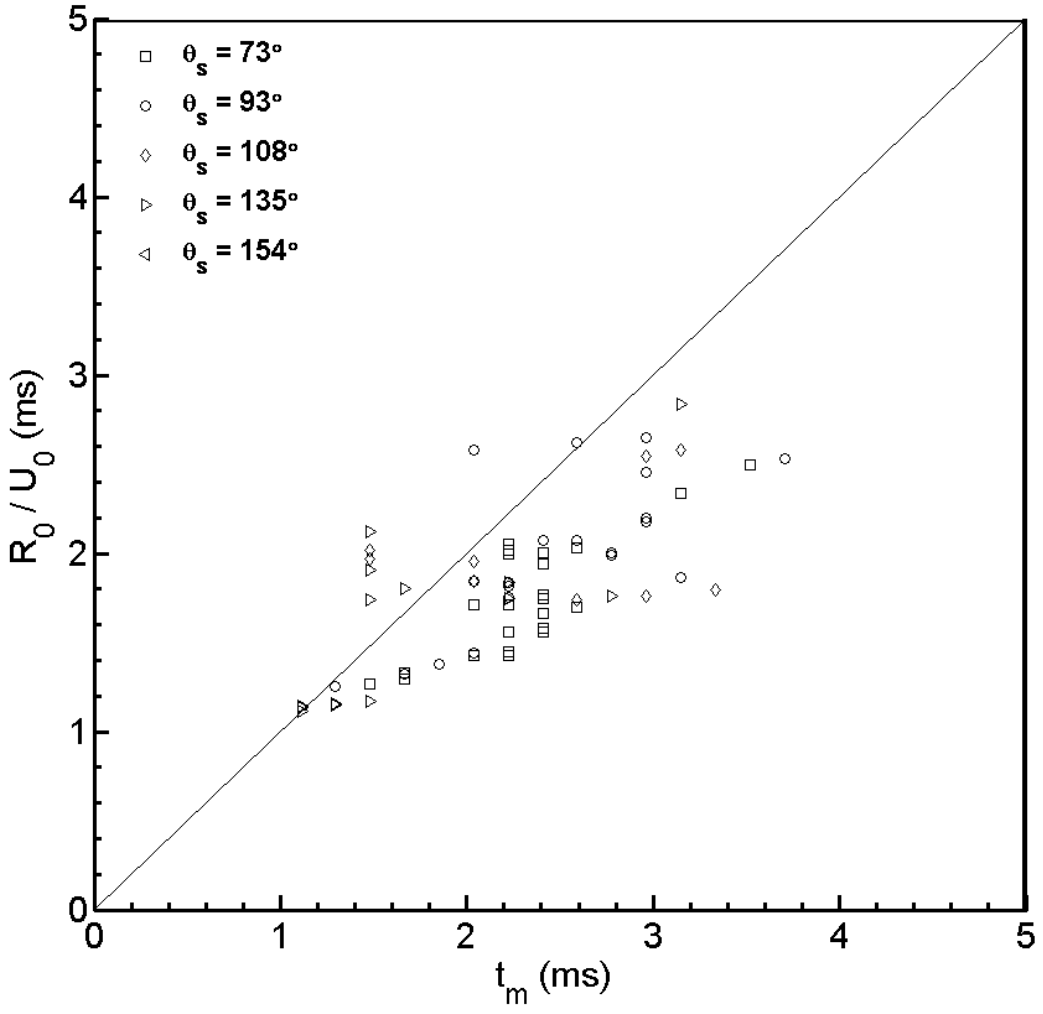

Figure 36: Comparison between the assumed and measured merging times.

3.2.3.1 Dissipation during merging

The viscous dissipation during the merging phase will be similar to the works of Jiang et al. [14], Zhang et al. [15], Qian et al. [17] and Tang et al. [83] where the important dissipation happens in a bulging region. In this region axial momentum is transferred to radial momentum in the form of a growing bulge. The thickness of the dissipation region within the bulge was obtained by Jiang et al. [14] by equating the dynamic pressure to the viscous strain. In the work of Jiang et al. [14], the velocity used is the velocity of each droplet, whereas the current study has one droplet moving and the other resting; therefore, half the velocity is used in the relations from Jiang et al. [14]. The expression is re-derived with the nomenclature used in this thesis.

$$\frac{1}{2}\rho\left(\frac{U_0}{2}\right)^2 \sim \frac{\mu(\frac{U_0}{2})}{b}$$

$$b \sim \frac{4\mu}{\rho U_0}$$

The volume where dissipation occurs is estimated as,

$$V = 2\pi {R_0}^2 b$$

Velocity Gradient during merging can be estimated as,

$$\frac{du}{dz} = \frac{U_0}{2b}$$

Resulting in the following for dissipation due to merging,

$$\phi_m = \mu\left(\frac{U_0}{2b}\right)^2 2\pi {R_0}^2 b\ \frac{R_0}{U_0}$$

$$\phi_m = \mu\left(\frac{U_0}{2\frac{4\mu}{\rho V}}\right)^2 2\pi {R_0}^2 \frac{4\mu}{\rho U_0}\ \frac{R_0}{U_0}$$

$$\phi_m = \frac{\pi}{8}\rho {U_0}^2 {R_0}^3$$

$$\phi_m = \frac{\pi}{16}\left(\rho {U_0}^2 D_0\right){R_0}^2$$

3.2.3.2 Dissipation during spreading

The viscous dissipation during spreading is approximated based on the previously discussed work of Pasanided-Fard et al. [45] The boundary layer thickness is defined as:

$$\delta = \frac{2D_0}{\sqrt{Re}}$$

Time used for dissipation during spreading is the time from the end of bulging to the time the droplet is fully spread. These times were validated previously. The resulting time where dissipation occurs due to spreading is,

$$\Delta t = \frac{D_{max}}{U_0} - \frac{R_0}{U_0}$$

The velocity gradient in the fluid scales with the boundary layer thickness as,

$$\frac{du}{dz} = \frac{U_0}{\delta}$$

Lastly, the volume of dissipation is defined as,

$$V = \pi {R_{max}}^2 \delta$$

Resulting in the following dissipation

$$\phi_s = \mu \frac{{U_0}^2}{\delta^2} \left(\frac{D_{max}}{U_0} - \frac{R_0}{U_0} \right) \pi {R_{max}}^2 \delta$$

$$\phi_s = \mu \frac{U_0}{\delta} \left(D_{max} - R_0 \right) \pi {R_{max}}^2$$

$$\phi_s = \mu \frac{U_0 \sqrt{Re}}{4R_0} \left(2 - \frac{R_0}{R_{max}} \right) \pi {R_{max}}^3$$

$$\phi_s = \frac{\pi}{4} \sqrt{Re} \frac{\mu}{R_0} U_0 \left(2 - \frac{R_0}{R_{max}} \right) {R_{max}}^3$$

3.2.3.3 The total viscous dissipation

The total viscous dissipation is the summation of the dissipation during spreading and merging. This results in the following,

$$\phi = \phi_m + \phi_s$$

$$\phi = \frac{\pi}{16} \left(\rho {U_0}^2 D_0 \right) {R_0}^2 + \frac{\pi}{4} \sqrt{Re} \frac{\mu}{R_0} U_0 \left(2 - \frac{R_0}{R_{max}} \right) {R_{max}}^3$$

By non-dimensionalizing with respect to the surface tension of the liquid and the size of the droplet the following expression is obtained,

$$\frac{\phi}{\gamma_{lv} {R_0}^2} = \frac{\pi}{16} \left(\frac{\rho {U_0}^2 D_0}{\gamma_{lv}} \right) + \frac{\pi}{4} \sqrt{Re} \left(\frac{\mu U_0}{\gamma_{lv}} \right) \left(2 - \frac{R_0}{R_{max}} \right) \frac{{R_{max}}^3}{{R_0}^3}$$

$$\frac{\phi}{\gamma_{lv} {R_0}^2} = \frac{\pi}{16} (We) + \frac{\pi}{4} \sqrt{Re} \left(\frac{We}{Re} \right) \left(2 - \frac{R_0}{R_{max}} \right) \frac{{R_{max}}^3}{{R_0}^3}$$

$$\frac{\phi}{\gamma_{lv} {R_0}^2} = \frac{\pi}{4} We \left[\frac{1}{4} + \frac{1}{\sqrt{Re}} \left(2 - \frac{R_0}{R_{max}} \right) \frac{{R_{max}}^3}{{R_0}^3} \right]$$

The amount of viscous dissipation increases with droplet inertia and total spreading. Should the Reynolds number become sufficiently large, the amount of energy lost due to differences in spreading diameter could become negligible. This change is similar to what is presented by Pasandideh-Fard et al.

[45] where at sufficiently high inertias, the effect of surface wettability has a diminished or insignificant effect on maximum spreading.

3.2.4 Conservation of energy

The conservation of energy for the system results in the following expression

$$E_k + E_{lv0} + E_{ls0} - \phi = E_{lvf} + E_{lsf}$$

Substituting the surface area terms and kinetic energy results in,

$$\frac{1}{2}\rho\frac{4}{3}\pi R_0^3 {U_0}^2 + (A_{lv}\gamma_{lv})_0 + (A_{ls}\gamma_{ls})_0 - \phi = (A_{lv}\gamma_{lv})_f + (A_{ls}\gamma_{ls})_f$$

Non-dimensionalizing the preceding expression with respect to the projected impacting droplet area and surface tension results in the following,

$$\frac{1}{2}\rho\frac{4}{3}\frac{R_0 {U_0}^2}{\gamma_{lv}} + \frac{A_{lv0}}{\pi R_0^2} + \frac{A_{ls0}}{\pi R_0^2}\frac{\gamma_{ls}}{\gamma_{lv}} - \frac{\phi}{\gamma_{lv}\pi R_0^2} = \frac{R_{max}^2}{R_0^2} + \frac{32}{3}\frac{R_0}{R_{max}} + \frac{\gamma_{ls}}{\gamma_{lv}}\frac{R_{max}^2}{{R_0}^2}$$

Which simplifies to equation (17),

$$\frac{We}{2\sqrt{Re}}\frac{{R_{max}}^3}{{R_0}^3} + \left(1 + \frac{\gamma_{ls}}{\gamma_{lv}} - \frac{We}{4\sqrt{Re}}\right)\frac{{R_{max}}^2}{{R_0}^2} + \frac{32}{3}\frac{R_0}{R_{max}} - \left(\frac{13}{48}(We) + \frac{A_{lv0}}{\pi R_0^2} + \frac{A_{ls0}}{\pi R_0^2}\left(\frac{\gamma_{ls}}{\gamma_{lv}}\right)\right) = 0 \qquad (17)$$

3.2.5 Model validation

Since equation (17) is non-linear it is solved using a bracketing method on Matlab with a step size of 5 x 10^{-8} for the cases solved presented in Tables 7 through 11, and are compared graphically to the experimental values in Figure 37. For aluminum, the model consistently over predicts the maximum spread diameter. The hydrophobic surfaces give reasonable results, overall. It is interesting to note how the total spreading time is an overestimate and the bulging time is an underestimate, and how these errors likely balance each other to give a reasonable result.

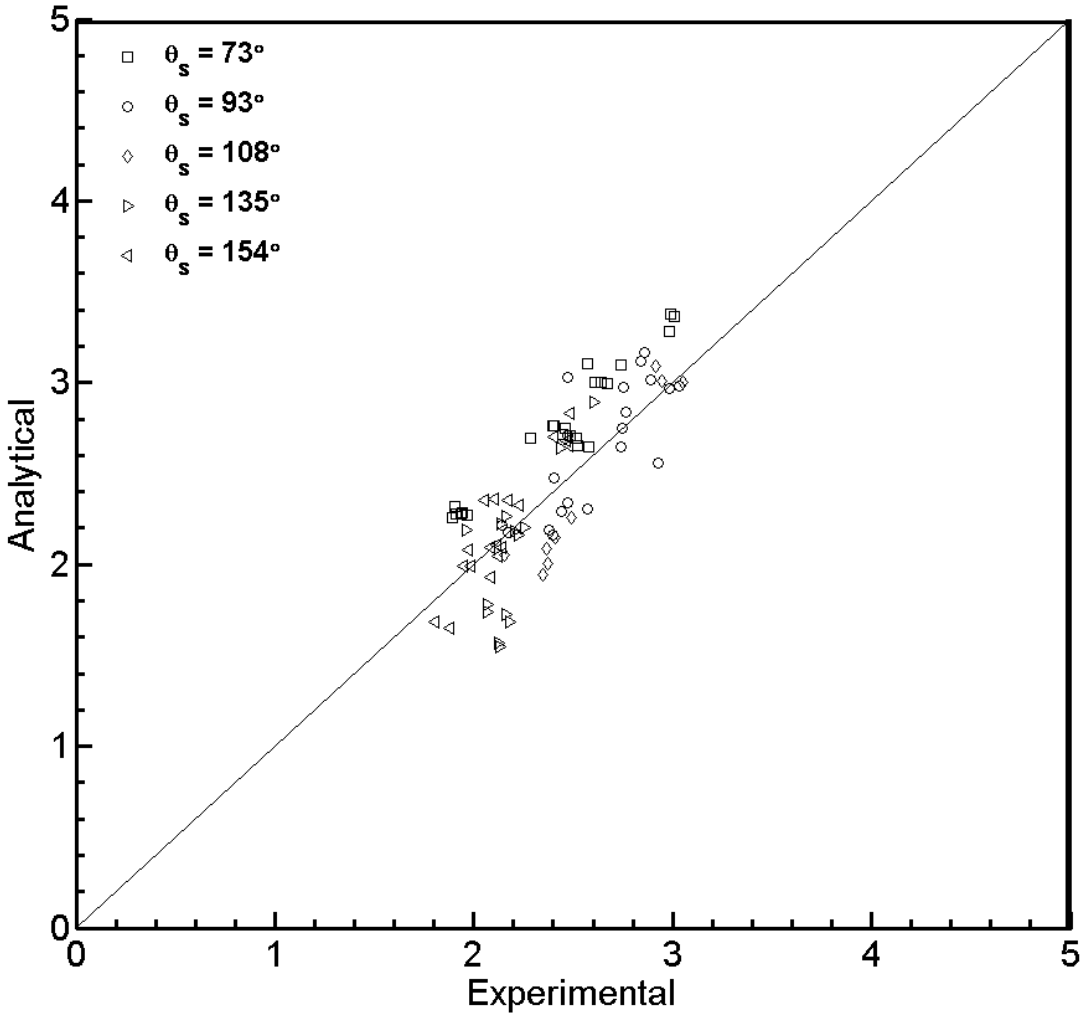

Figure 37: Validation of the proposed analytical model for predicting maximum spread factor.

Table 7: Validation of the proposed analytical model for droplets impinging on aluminum.

Impact Parameters			ξ_{max}		
Diameter (mm)	**Velocity (mm/s)**	λ	**Experimental**	**Analytical**	**%Error**
3.78	758	0.06	2.57	3.11	17
3.61	772	0.08	2.74	3.10	12
2.66	855	0.08	2.67	2.99	11
2.67	858	0.02	2.64	3.00	12
2.69	853	0.01	2.61	3.00	13
2.61	1033	0.06	3.01	3.37	11
2.63	990	0.04	2.99	3.28	9
2.66	1029	0.00	2.99	3.38	12
2.33	584	0.07	1.94	2.29	15
2.36	575	0.10	1.91	2.28	16
2.33	573	0.02	1.89	2.26	16
2.33	599	0.03	1.90	2.32	18
2.33	581	0.01	1.93	2.28	15
2.33	577	0.02	1.96	2.27	14
2.51	754	0.03	2.45	2.72	10
2.54	718	0.03	2.58	2.65	3
2.53	746	0.01	2.48	2.71	8
2.53	724	0.01	2.52	2.66	5
2.53	740	0.07	2.28	2.69	15
2.53	739	0.09	2.52	2.69	6
2.31	810	0.07	2.40	2.76	13
2.32	800	0.02	2.46	2.75	11
2.31	810	0.05	2.40	2.76	13

Table 8: Validation of the proposed analytical model for droplets impinging on Teflon

Impact Parameters			ξ_{max}		
Diameter (mm)	**Velocity (mm/s)**	λ	**Experimental**	**Analytical**	**%Error**
2.65	729	0.09	2.14	2.22	4
2.65	720	0.04	2.38	2.19	9
2.64	755	0.07	2.44	2.29	7
2.64	710	0.03	2.40	2.16	11
2.64	716	0.05	2.17	2.18	0
3.51	716	0.03	2.40	2.48	3
3.54	667	0.03	2.47	2.34	6
3.48	663	0.07	2.57	2.30	12
3.83	873	0.06	2.47	3.03	18
3.84	760	0.02	2.47	2.71	9
3.78	910	0.02	2.84	3.12	9
3.83	922	0.01	2.86	3.17	10
3.79	872	0.04	2.89	3.02	4
3.55	886	0.06	2.98	2.97	0
3.54	890	0.09	3.03	2.98	2
3.72	721	0.08	2.93	2.56	14
2.60	980	0.01	2.76	2.84	3
2.60	943	0.02	2.75	2.75	0
2.60	900	0.06	2.74	2.64	4
2.60	1038	0.04	2.75	2.98	8

Table 9: Validation of the proposed analytical model for droplets impinging on Fluoropel coated aluminum

Impact Parameters			ξ_{max}		
Diameter (mm)	**Velocity (mm/s)**	λ	**Experimental**	**Analytical**	**%Error**
2.59	700	0.08	2.35	1.94	21
2.59	745	0.10	2.36	2.09	13
2.59	720	0.03	2.37	2.01	18
2.59	734	0.06	2.15	2.05	5
3.40	668	0.09	2.41	2.15	12
3.54	687	0.04	2.49	2.26	10
3.68	932	0.07	2.95	3.01	2
3.72	923	0.07	3.05	3.00	2
3.74	955	0.07	2.91	3.09	6

Table 10: Validation of the proposed analytical model for droplets impinging on Teflon320

Impact Parameters			ξ_{max}		
Diameter (mm)	**Velocity (mm/s)**	λ	**Experimental**	**Analytical**	**%Error**
2.16	944	0.10	1.96	2.19	11
2.17	940	0.06	2.20	2.18	1
2.15	962	0.08	2.14	2.23	4
2.15	935	0.04	2.22	2.16	3
2.19	968	0.08	2.16	2.26	4
2.20	942	0.03	2.26	2.20	3
3.71	874	0.01	2.43	2.64	8
3.69	969	0.10	2.60	2.89	10
3.75	618	0.04	2.05	1.83	12
3.55	624	0.05	2.06	1.78	16
2.53	729	0.07	2.07	1.74	19
2.53	700	0.02	2.13	1.57	36
2.51	720	0.01	2.18	1.68	30
2.55	724	0.04	2.16	1.72	26
2.55	694	0.00	2.13	1.55	37

Table 11: Validation of the proposed analytical model for droplets impinging on WX2100

Impact Parameters			ξ_{max}		
Diameter (mm)	**Velocity (mm/s)**	λ	**Experimental**	**Analytical**	**%Error**
2.65	709	0.03	1.88	1.65	14
2.65	715	0.03	1.80	1.68	7
3.96	687	0.03	2.11	2.11	0
3.80	668	0.00	1.95	1.99	2
3.67	663	0.02	2.08	1.93	8
3.74	674	0.02	1.99	1.99	0
2.58	846	0.08	2.14	2.09	2
2.58	831	0.02	2.12	2.05	3
2.61	840	0.01	1.97	2.08	5
2.60	845	0.03	2.09	2.10	0
2.51	962	0.00	2.06	2.35	12
2.55	959	0.05	2.10	2.36	11
2.52	962	0.03	2.17	2.36	8
2.52	949	0.05	2.23	2.33	4
3.54	922	0.03	2.48	2.66	7
3.57	926	0.01	2.47	2.68	8
3.69	920	0.03	2.40	2.70	11
3.67	972	0.08	2.49	2.83	12

4 Effect of offset on coalescing droplets

Even in controlled conditions, a head-on impact is seldom observed; therefore, for practical applications, insight into the effect of spacing is required. This section will discuss the morphology of merging droplets as offset is increased for the five types of surfaces previously discussed. The results of the maximum spreading are unified with a regression model and new Weber number.

Studying the effect of offset between droplets is required since it is highly relevant to the ink-jet industry. In addition, spray cooling and coating are somewhat random; therefore droplet would coalesce in a variety of geometries. The surfaces studied are the same as discussed in the previous section. Images of increasing offset are shown in Figure 38. A near head-on offset could be considered as an axisymmetric case; moderate offsets involve the impinging droplet striking the sessile droplet obliquely; and large offsets are those where the droplet impacts mostly the substrate and merges into the sessile droplet while spreading. As discussed in Section 2.4, the offset is non-dimensionalized by the droplet diameter, $\lambda = L/D_{0,}$ and the wetted length is non-dimensionalized based on the droplet diameter and offset to give $\Psi = D_y/(D_0 + L)$, the spread effectiveness.

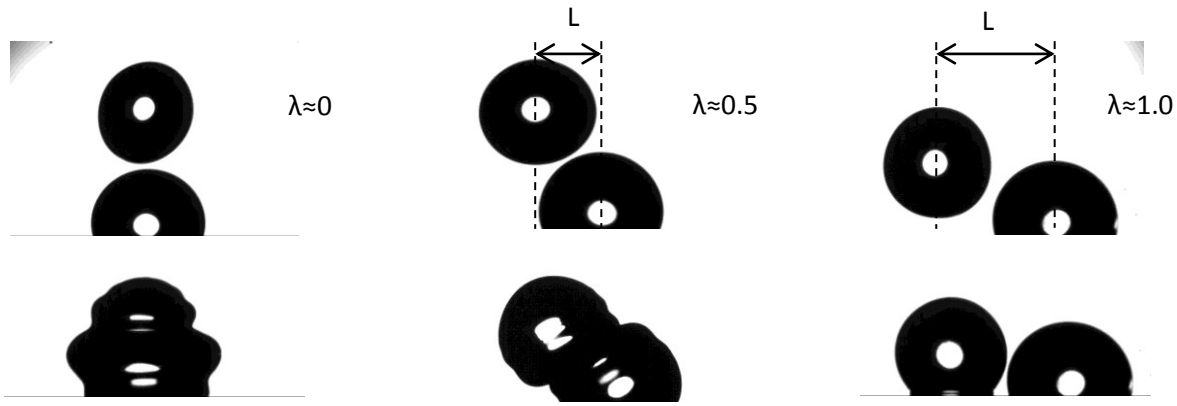

(a) Head-on (b) Moderate (c) Large

Figure 38: Offset coalescence cases (a) Head-on, (b) Moderate and (c) Large.

4.1 Morphology

Figure 39 and Figure 40 present the effect of a moderate offset for the case of 0.55 < λ < 0.63 with a Weber number of 22 and a Reynolds Number of 2020. The effect of offset is compared among all five surfaces. For brevity, the profiles of the coalescence process of aluminum, Teflon and Fluoropel are shown in Figure 39 and the spread factor for all five surfaces studied are shown in Figure 40. The morphology has many common points to the head-on case, where the droplets deform, merge and spread. Furthermore, the recoiling phase is dictated by the receding contact angle, similar to the case of head-on impact.

For all cases presented in Figure 39, inertia from the impinging droplet causes both droplets to deform slightly during the first two milliseconds. As the merging continues, the drop deforms against the substrate as seen at roughly 3.2ms. The leftmost section of the droplet spreads along the surface while the rest of the droplet merges with the sessile droplet and deforms. Within 6-7 ms after impingement,

the drop has reached a fully spread position. It is interesting to note that the sessile droplet is still recognizable, as seen by the round shape on the right side of the fully spread droplet. This implies that most of the deformation has occurred in the fluid from the impinging droplet.

For the case of Fluoropel, the droplet is seen to be able to reach a small spread diameter and substantial height at 25ms, compared to the less hydrophobic cases as seen at 20ms for aluminum and 27ms for Teflon, this small spread diameter is corroborated in Figure 40. By 10ms, all three cases are recoiling. Similar to the head-on case, it is shown that the receding contact angle influences the recoiling shape. Aluminum and Teflon both have receding angles less than 90° and take on wide and flat shapes at 17ms as opposed to Teflon320 which has a large receding angle and takes on a cylindrical shape at 22ms as it recoils.

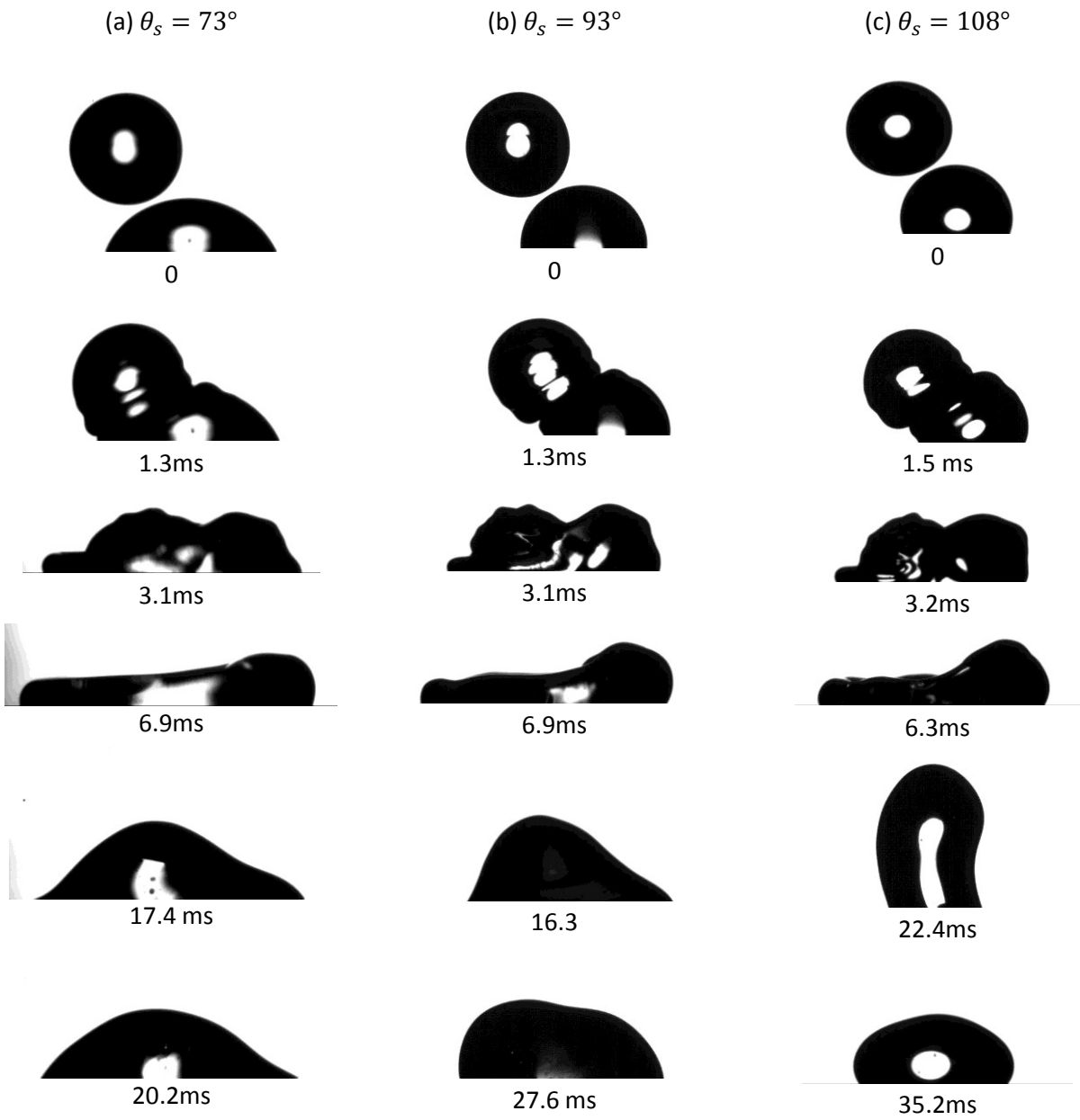

Figure 39: Droplet Impingement comparison at dimensionless offset of 0.55 < λ < 0.63, with Re= 2020 and We = 22, on (a) Aluminum, (b) Teflon and (c) Fluoropel.

More details regarding the spreading are obtained from Figure 40. A substantial decrease in minimum wetted length is observed for Fluoropel, Teflon 320 and WX2100, as opposed to aluminum and Teflon, which is consistent with a change in receding contact angle. The static spread diameter is greater than the minimum spread diameter for the three most hydrophobic surfaces studied, while the smallest spread diameter for aluminum and Teflon is their static spread diameter.

Offset increases the maximum wetted length reached. The maximum spread factor, $\xi_{max} = D_{max}/D_0$, for the head-on cases ranges from 1.7 to 2.5 as was previously shown in Figure 28 on page 47 in section 3.1. Figure 40 shows that the spread effectiveness, $\Psi = D_y / (D_0 + L)$, for the cases of $0.55 < \lambda < 0.63$ ranges from 1.4 to 1.75. These values correspond to spread factors ranging from 2 to 2.6. All cases have comparable Weber and Reynolds numbers. It can be understood that increasing the offset has a more pronounced effect on hydrophobic surfaces then hydrophilic surfaces. Since, the maximum spread factor of aluminum increases from 1.7 to 2.0 but only increases from 2.5 to 2.6 for WX2100.

The offset directly increases the spreading length, but to assess how effectively it does so, the spread effectiveness can be used. By normalizing the wetted length with both the impinging droplet diameter and offset, the effectiveness of offset on spreading can be measured. For the head-on case, spread effectiveness is comparable to spread factor, since it ranges from 1.7 to 2.5. As offset is increased, the spread effectiveness decreases to a range of 1.4 to 1.75 for the moderate offset case shown in Figure 40. This indicates that the coalescence and spreading process is less efficient, likely due to greater deformation. Understanding the effect of wettability on spreading can be obscured if the offsets are not identical. Using spread effectiveness is one solution to alleviate, which is another reason for normalizing spread length with both droplet size and offset.

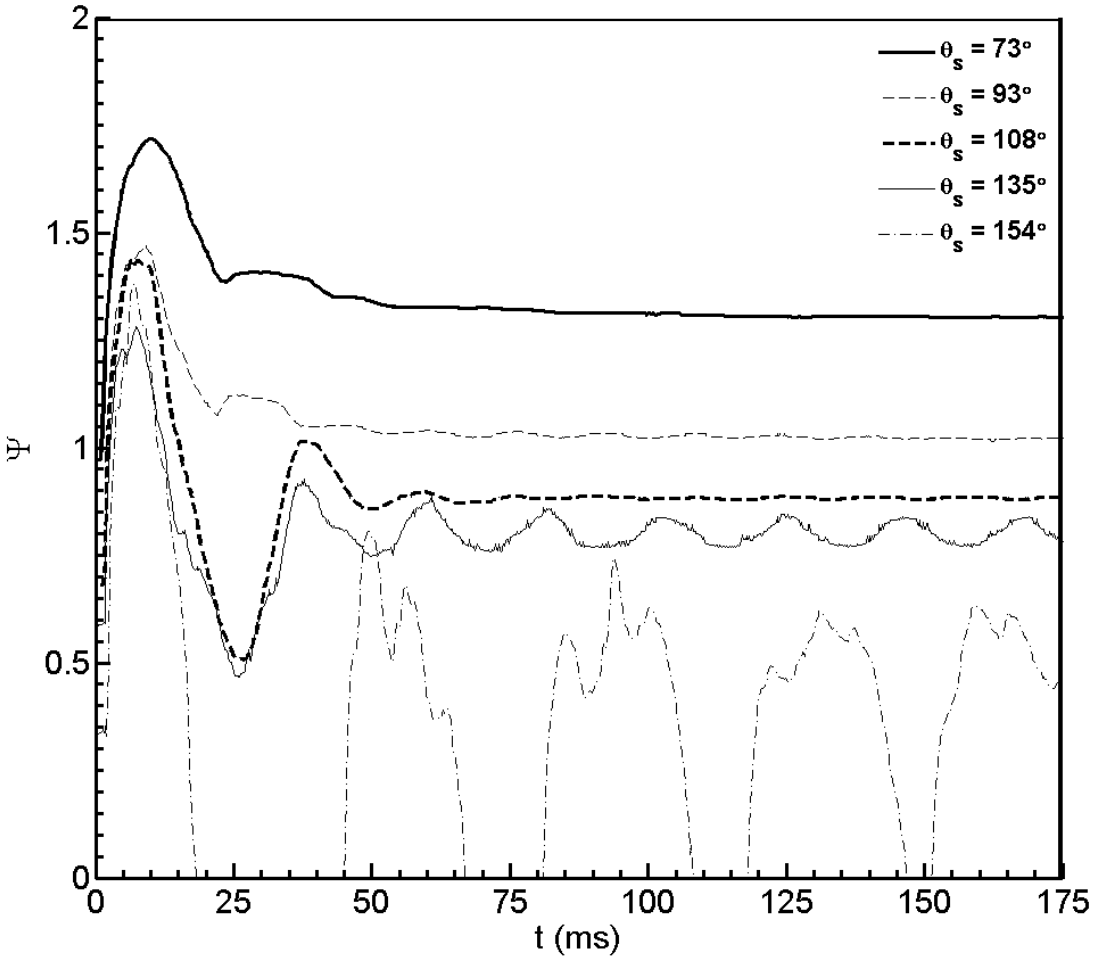

Figure 40: Evolution of spread diameter over time for offset of $0.55 < \lambda < 0.63$, with Re= 2020 and We = 22.

As offset increases, the impinging droplet will impact both the substrate and the sessile droplet at nearly the same moment. Such a case of merging is presented in Figure 41 by the evolution of the profile and in Figure 42 by the spread effectiveness. At an offset of $0.97 < \lambda < 1.04$, the morphology can be understood as a mix of droplets coalescing and droplets impacting a dry surface. The merging droplets could be split into three sections during the early, before 2.2ms, stages of merging shown in Figure 41. The leftmost section of the droplet resembles the impingement of a single droplet, a merging region in the middle and a sessile droplet on the far right. As the spreading continues the merged droplets takes on a shape similar to that discussed in the previous section at maximum spreading; a flattened disk and a bump at

roughly 5.5ms. This bump corresponds to the sessile droplet and is more pronounced than the previous case of $0.55 < \lambda < 0.63$, shown in Figure 39. The qualitative understanding of spreading in response to offset and wettability is continued in Figure 42. The difference between the maximum spread effectiveness is comparable to the static spread effectiveness when the impingement occurs on aluminum and Teflon. Consistent with the previous cases as the offset is increased the maximum spread effectiveness decreases.

As seen in Figure 42, Fluoropel, Teflon320 and WX2100 recoil much sooner and for a longer period of time when compared to aluminum and Teflon. From Figure 41, the profiles of the droplet on the two more wettable surfaces both resemble a semi ellipse after having recoiled, as seen at 11ms. In contrast, the impinging droplet on the Teflon320 has reached a substantial height at 11.3ms. The impinging droplet recoils readily on Teflon320, due to its higher receding contact angle. By 17ms, the impinging droplet has recoiled and pulled the sessile droplet along with it. Similarly, the droplet on Fluoropel has become non-symmetric, unlike the more wettable surfaces. Lastly, the equilibrium spread lengths are seen to be much greater for aluminum and Teflon than the other three surfaces.

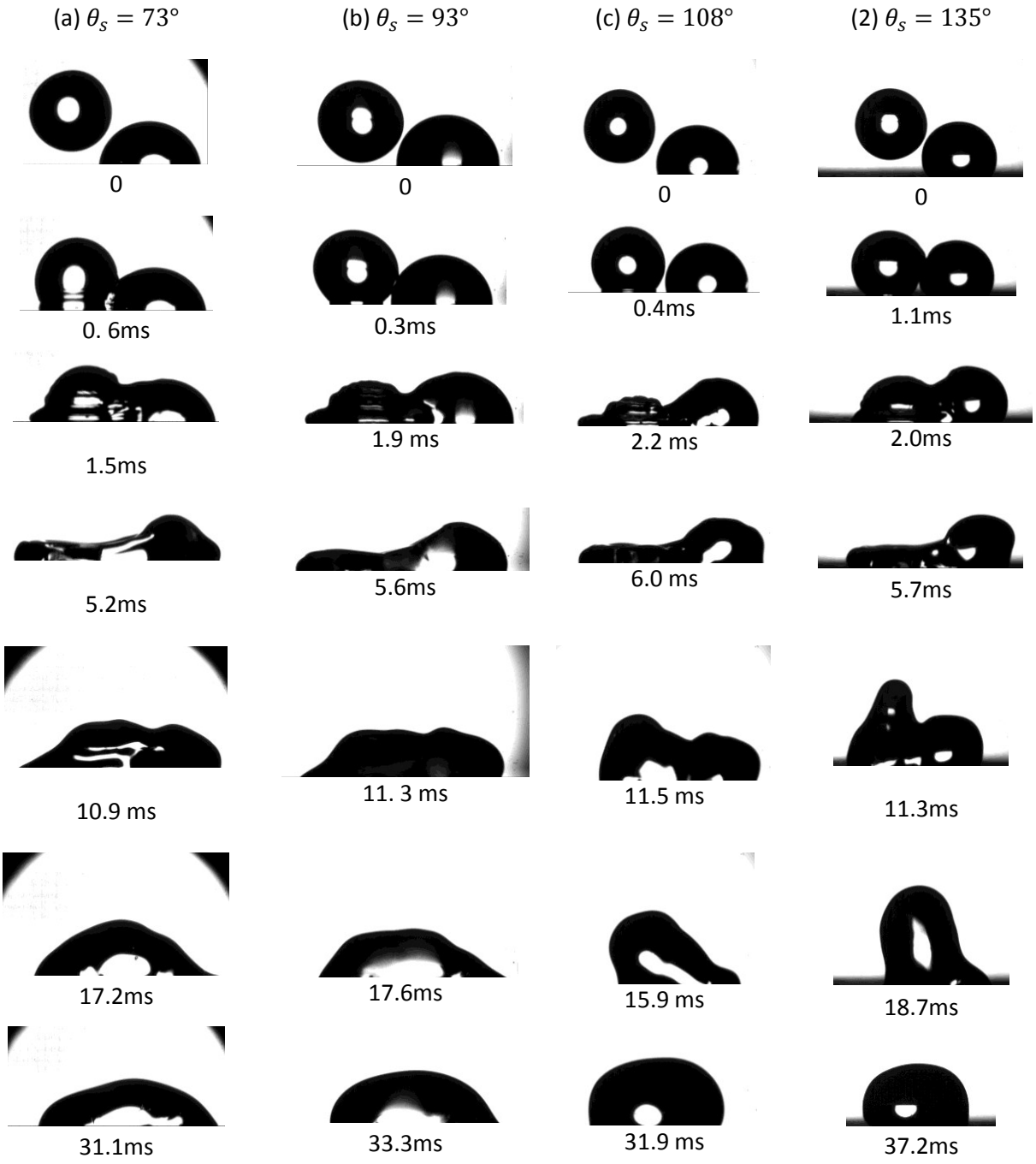

Figure 41: Merging at an offset of 0.97 < λ < 1.04 with Re= 2020 and We = 22 on surfaces of (a) aluminum, (b) Teflon, (c), Fluoropel and (d) Teflon320.

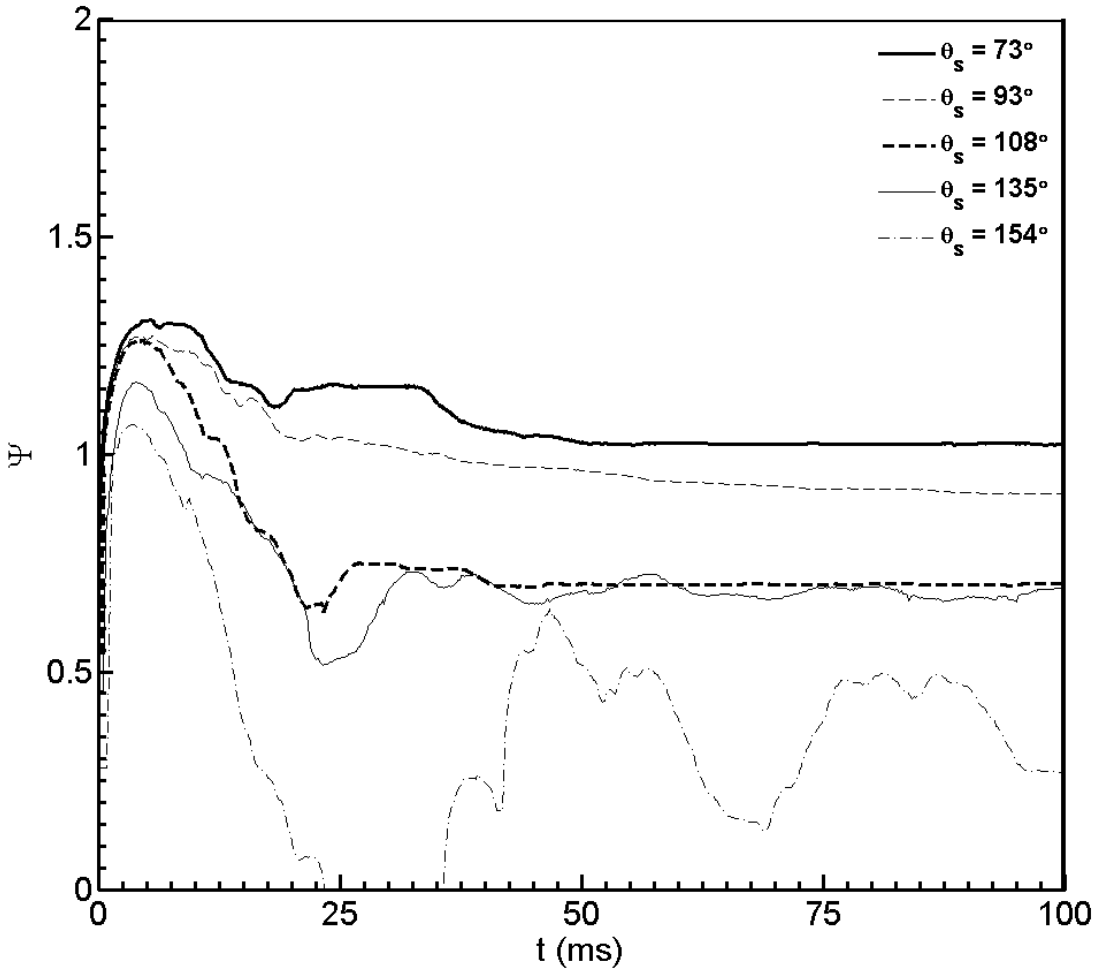

Figure 42: Spread Effectiveness for an offset of 0.97 < λ < 1.04, with Re= 2020 and We = 22.

Variations of maximum spread effectiveness in response to offset for all five surfaces is shown in Figure 43. To express how efficiently increasing offset increases the spreading, the spread effectiveness was used. A decrease in Ψ_{max} implies that offset is less effective at increasing the spread length, but does not mean the actual spread length decreases with offset. The maximum spread effectiveness decreases by increasing the offset ratio and surface hydrophobicity, as seen in the Figure 43. At large offset cases, surface wettability has two effects, it impedes the spreading of the droplet prior to merging and impedes the spreading of the droplets once they merged. In contrast, droplets at small offsets merge then spread; hence, wettability only comes into play on the later stage.

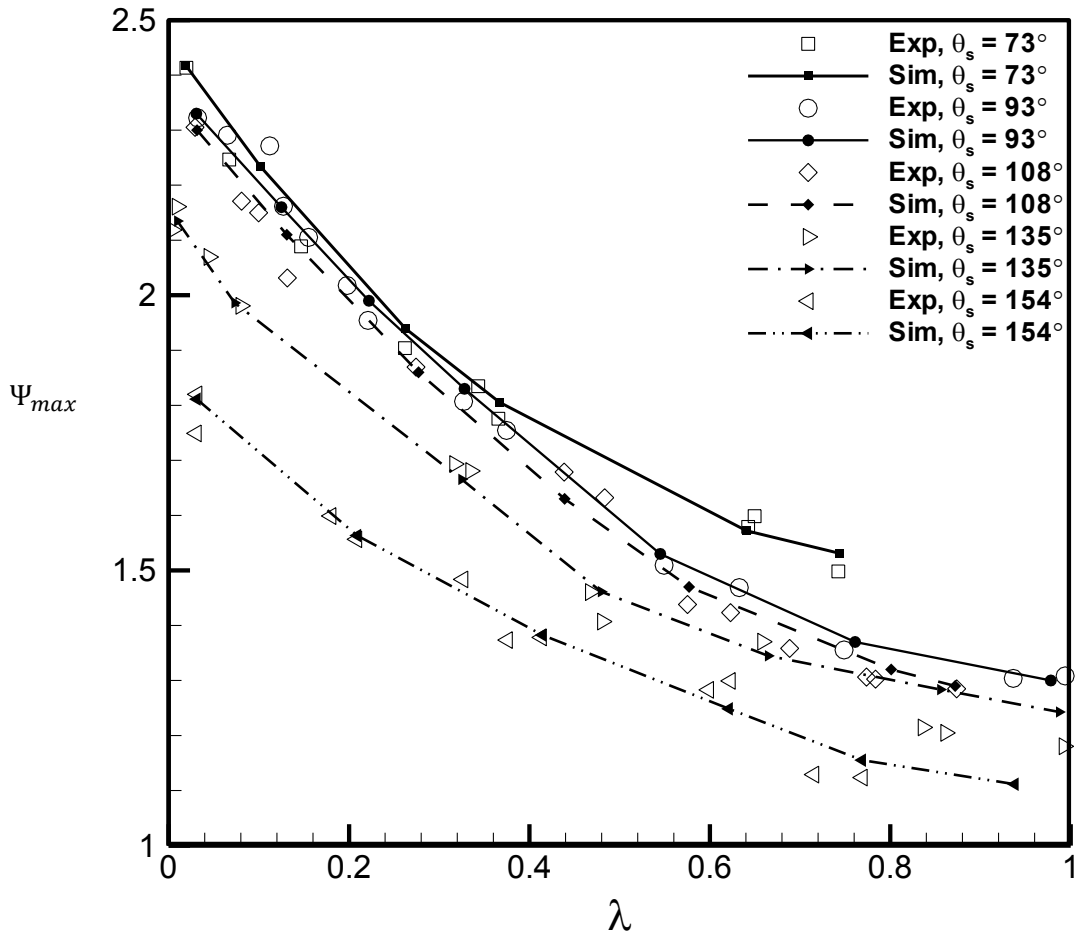

Figure 43: The effect of offset and surface wettability on the maximum spread effectiveness as a function of offset ratio for We ≈ 20.

4.2 Regression model

A regression analysis is performed to unify the effect of droplet inertia, droplet offset and substrate wettability. The maximum spreading length for each droplet size, impinging velocity, spacing and surface is summarized with one empirical correlation. In order to unify the effect of all five surfaces (from hydrophilic to superhydrophobic) a new Weber number is defined as,

$$We_{sl} = \frac{\rho {U_0}^2 D_0}{\gamma_{sl}}$$

This surface Weber number is the ratio between droplet inertia and liquid-solid interfacial energy, or the ratio between incoming inertial energy and the ability of the surface to store energy. It is defined based on the works of Chibowski, [32] who defined the liquid-solid surface energy based on the contact angle

hysteresis, as seen in equation (14). Performing a least squared fitting of the natural logarithms of Ψ_{max}, λ and We_{sl}, similar to the works of Li et al., [8] yields the expression seen in equation (18). The correlation coefficient is 0.8795, which indicates a coherent trend. In contrast to the work of Li et al. [8], this work did not study different liquids, only the inertia was varied for different offsets and surfaces; therefore, it would be misleading to include either Ohnesorge number or Reynolds number, since those numbers include the effect of viscosity. The resulting regression model is compared graphically to experimental and numerical results in Figure 44.

$$\frac{\gamma_{ls}}{\gamma_{lv}} = \frac{1 + \cos^2\theta_A}{2 + \cos\theta_R + \cos\theta_A} \tag{14}$$

$$\Psi_{max} = 0.9759(1 + \lambda)^{-0.7594} {We_{sl}}^{0.2283}, R^2 = 0.8795 \tag{18}$$

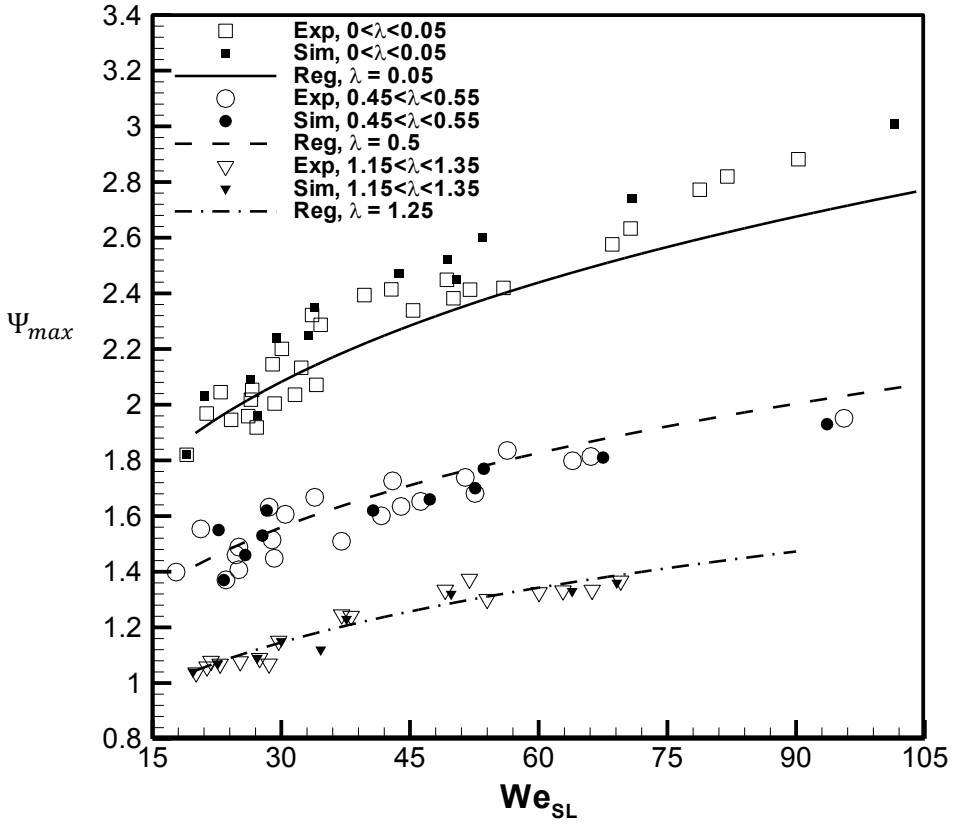

Figure 44: Comparison of equation (18) to experimental and numerical results.

5 Induced detachment of coalescing droplets on superhydrophobic surfaces

As discussed in the introduction, superhydrophobic surfaces have the unique ability to repel water extremely proficiently. This chapter will discuss the water repellency of superhydrophobic surfaces with respect to coalescing droplets. It was found that as long as droplets coalesced, the entire merged mass of water could be removed. The readers are encouraged to review "Induced detachment of Coalescing Droplets on a Superhydrophobic Surface" [(85)] *, which is a joint numerical and experimental study, for more information.*

Throughout chapters 3 and 4, the effect of both repellency and mobility were presented on the general morphology of coalescing droplets. It was noted that surfaces with small hysteresis and large receding contact angles are capable of recoiling substantially. Superhydrophobic surfaces were seen to allow the droplet to recoil until the point of detachment. This is an important phenomenon when considering water accumulation, since adding more droplets to the system may remove the original accumulated liquid.

5.1 Head-on impact

Firstly, Figure 45 presents an isometric view of a head-on impact with a Weber number of 22 and Reynolds number of 2020. The droplets have begun to deform and merge at 2ms, as seen by the ripples on the surface. As the merging continues, the droplet spreads along the surface until it reaches a maximum spread diameter at roughly 7ms. At this state it is relatively smooth but with some waves on its surface. Since it is fairly transparent, it is likely mostly horizontal. At 14.5ms, the droplet has begun to recoil and by 19.5ms a pronounced jet is formed in the center. This jet drives the droplet's detachment from the substrate. The detachment is forceful enough to allow the droplet to remain in the air even at 34.5ms.

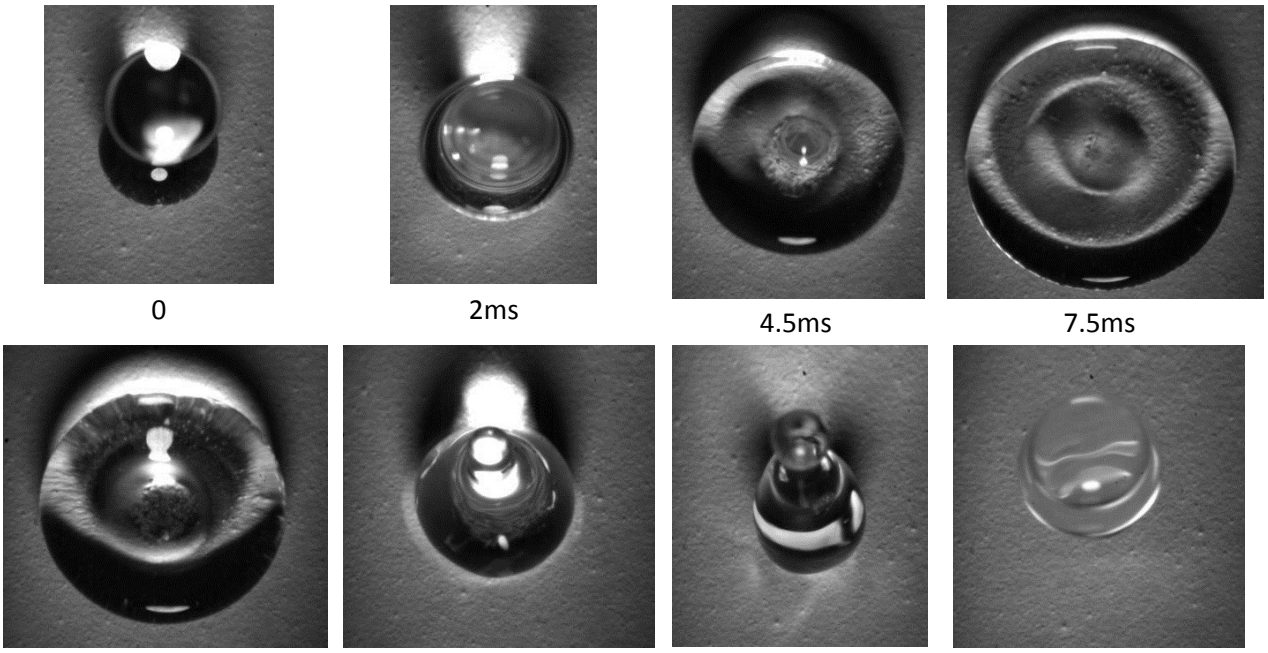

Figure 45: Top View of the head-on impact with We≈ 20 and Re ≈2020 on a superhydrophobic surface.

In order to understand the effect of Weber number on the detachment for a head-on case, Figure 46 shows the 2D profile of droplets coalescing for two different scenarios (a) Weber of 19, Reynolds of 2020 and (b) Weber of 26, Reynolds 3040. These two conditions demonstrate the effect of droplet size on the detachment behaviour of coalescing droplets by comparing a 2.6 mm to a 3.6mm droplet at a speed of roughly 700mm/s. Both droplets bulge during merging, spread into a disk like shape, then recoil and detach, similar to the discussion in the previous section, where the large receding contact angle dictates the recoiling behaviour. The difference between these cases is the manner in which they detach. For the larger droplet, the contact point detaches while the top section of the droplet is descending, as opposed to the smaller droplet, which detaches while the droplet is ascending. These discrepancies in detachment are observed in superimposed images in Figure 46, which correspond to times of 20-25.6ms for the case of the 2.65mm droplet and times of 40-45.6ms for the 3.96mm. In the superimposed images, the boundary of the droplet at the first instance is shown as a gray dashed line; the final shape as the actual droplet image; and the images in between are superimposed to create a gray streak effect. The upward momentum of the smaller droplet is sufficiently large such that the droplet continues to ascend after detachment, as seen at 25.6ms and 36.7ms, as opposed to the larger droplet which falls to the surface after having detached. The less potent detachment of the large droplet can be attributed to more deformation which in turn causes more dissipation. The smaller droplet will continue to bounce several times, until resting.

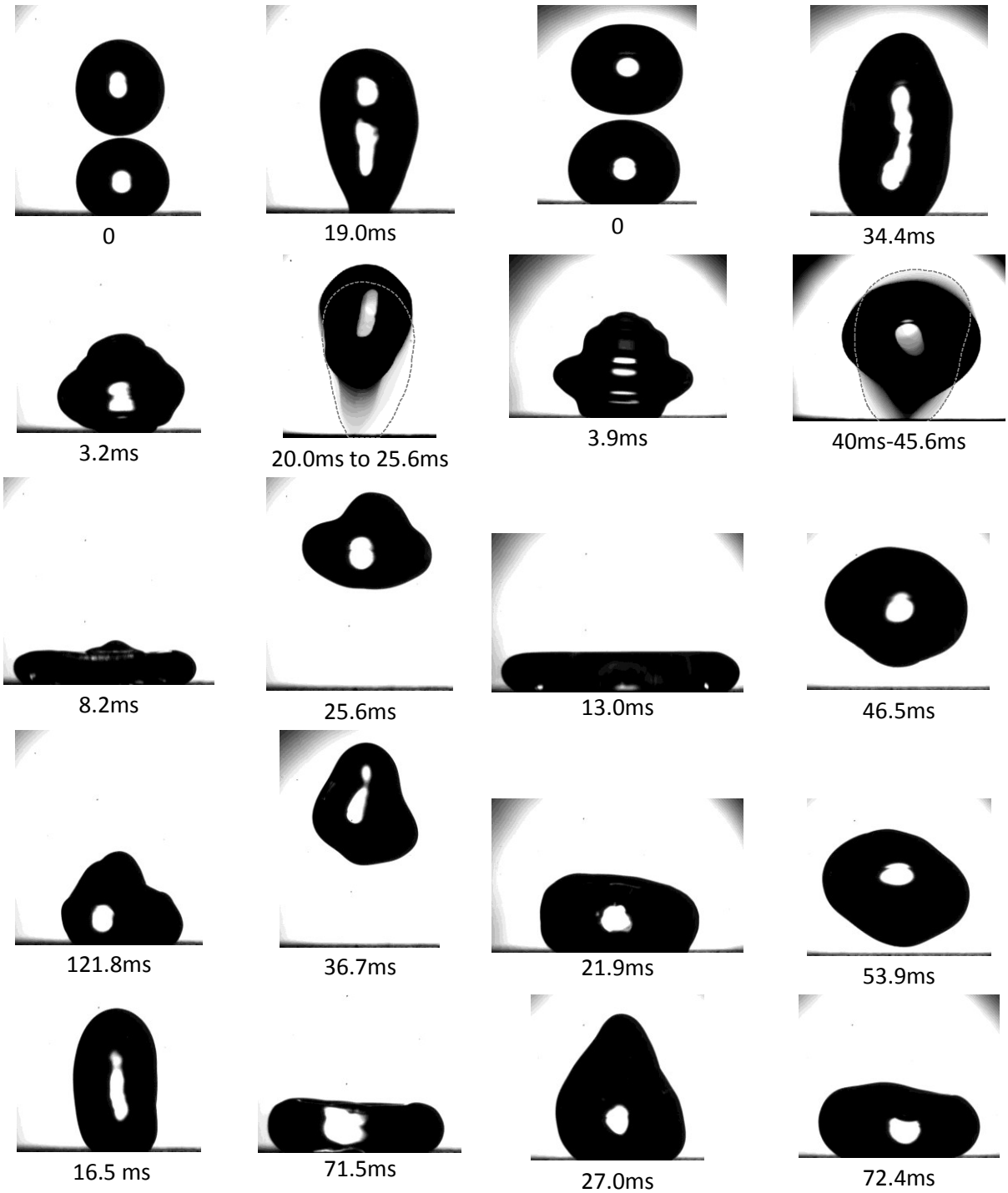

Figure 46: Head-on impact of a droplet on a superhydrophobic surface for (a) 2.65 mm droplet and (b) a 3.96 mm droplet, with similar velocity, U_0=700 ± 15 mm/s.

Figure 47 shows the non-dimensional spreading evolution over time. Since a comparison of only offset is required, the spread factor, $\xi = D_y/D_0$, will be used instead of a spread length, $\Psi = D_y/D_0 + L$. As previously discussed, the droplets are seen to detach, or bounce, from the surface. While a droplet is detached its spread diameter is zero. For the smaller droplet, multiple bounces are observed, as opposed to the large droplet which detaches merely once. The small droplet is detached from 23-57ms, 85-110ms and 138-149ms; in contrast, the large droplet is detached only from 42-51ms. In addition to the duration and frequency of the detachments, the recoiling rate leading up to the first detachment also differs. From 5.7 to 23.5ms, the smaller droplet recoils at a relatively constant rate; in contrast, the recoiling rate of the larger droplet decreases at 23.7ms. This discrepancy is consistent with the discussion related to detachment being either violently upwards, or detachment while part of the droplet has begun to descend, since the large droplet has a slower recoiling rate which corresponds to the moments leading up to detachment. In terms of energy dissipation, the larger droplet undergoes more shape changes; therefore, it dissipates more energy leading to only one detachment, which is not as prominent as the detachment for the case of the small droplet. An interesting commonality is the frequency and value of maximum spreading reached over time. The spread length peaks at similar instances and has similar values for both droplet sizes.

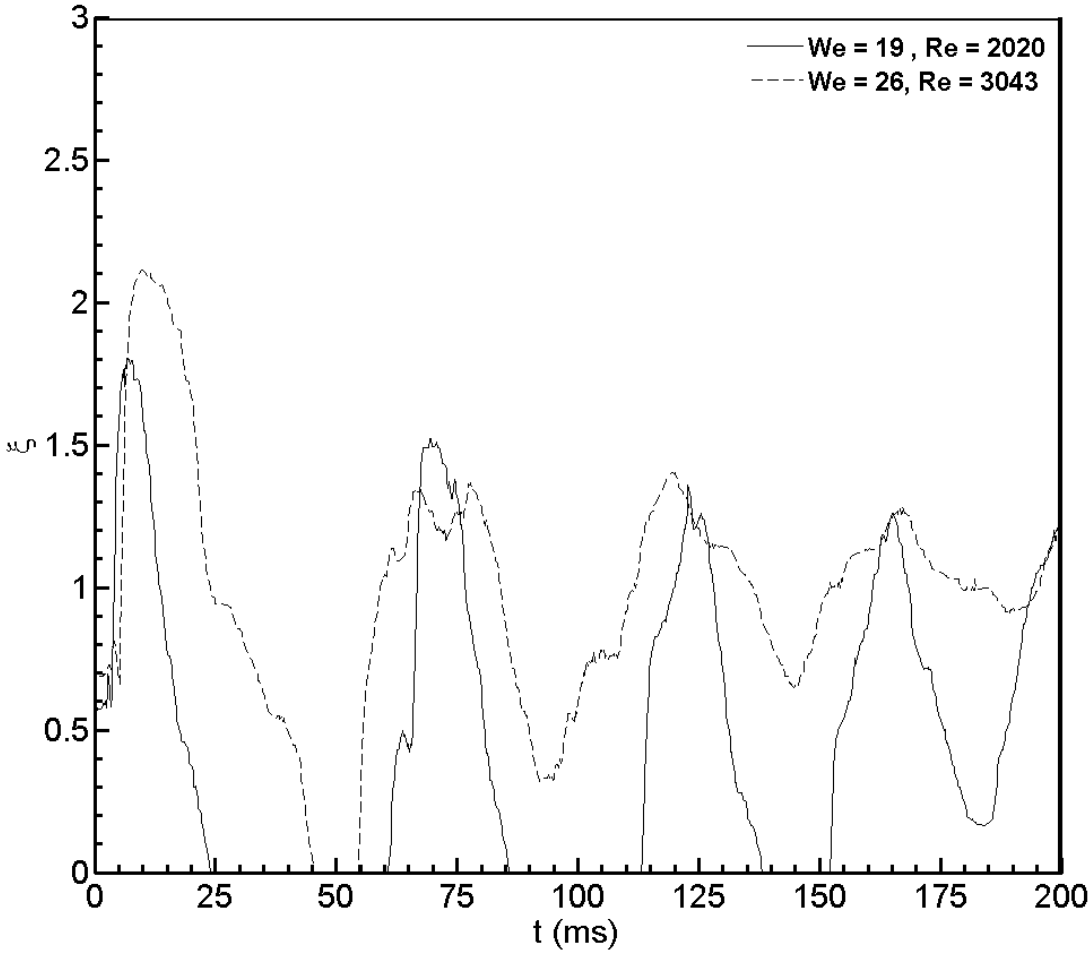

Figure 47: Temporal evolution of spread factor, $\xi = D_y / D_{0,}$ for head-on droplet coalescence on a superhydrophobic surface.

5.2 Effect of offset

This section presents three figures to interpret the effect of offset between the sessile droplet and the impinging droplet on detachment on superhydrophobic surfaces. Figure 48 shows the profile of the induced detachment for three cases: a slight offset (λ = 0.41) a moderate offset (λ = 0.77) and a large offset (λ = 1.04). The first case has an offset slight enough for the droplets to merge then spread; in contrast the large offset where the offset is large enough so that the impinging droplet impacts the surface and the droplets merge while spreading. Lastly, the second case shows behaviour in between

the two. An isometric view of offset corresponding to dimensionless offsets of 0.4 and 0.8 is shown in Figure 49 to enrich the discussion. All three offsets result in a similar spread shape, which resembles the shapes discussed in chapters 3 and 4. Lastly, the spread factor over time of the three cases presented here and the previous head-on case are shown in Figure 50.

The receding phase begins to offer some insight into the effect of offset not discussed in the previous chapter, since it pertains to superhydrophobic surfaces. As offset is increased, the merged droplet detaches in a more rotational manner. The recoiling is seen to be less symmetrical as offset is increased by comparing the slight offset case at 15.2ms; the moderate offset at 14.1ms and the large offset at 9.8ms. This asymmetric behavior causes a rotation of the detached droplet. The rationality of the detaching droplet is depicted through the superposition of various images, as done in Figure 46, for the head-on case. For the slight offset case, minor rotation is observed during detachment. Rotation is seen in the moderate case for instances 17.6ms through 21.5ms as seen by the superimposed images. In these superimposed images, the portion of the droplet originally on the surface has displaced substantially to the left of the image. Rotation continues as the droplet is in the air, as seen by the bulge on the lower left hand side of the droplet at 24.3ms. For the largest offset, the liquid of the initially sessile droplet is not displaced until the portion of the merged droplet from the impinging droplet has already reached a substantial height at roughly 15.4ms. The initially sessile liquid is then pulled laterally along the surface and then detaches, resulting in substantial rotation of the droplet.

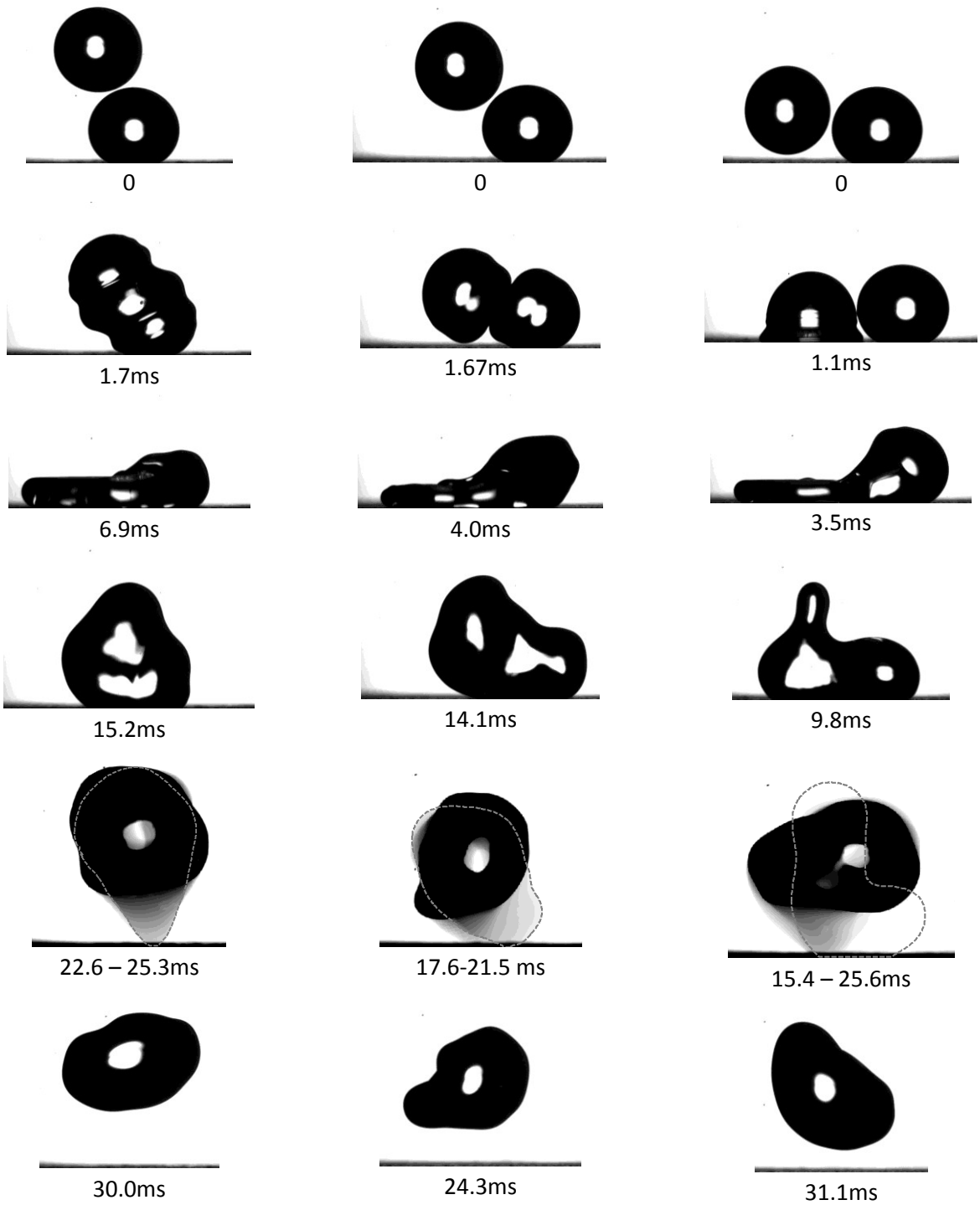

Figure 48: Profiles of droplets detaching off of superhydrophobic surfaces for offsets of (a) λ = 0.41, (b) λ = 0.77 and (c) λ = 1.04 with We = 19 and Re = 2020.

A top view of the nearly fully spread state for dimensionless offsets of 0.4 and 0.8 is shown in Figure 49. At the moderate dimensionless offset of 0.8, the footprint of the merged droplet while recoiling is remarkably non-symmetric, as seen at times of 6 and 12ms. In contrast, the slight offset case resembles a circle or ellipse at 7 and 10ms. In the moments leading up to detachment, a substantial portion of the droplet has yet to be displaced for the moderate offset of 0.8, as seen in both Figure 48 (b) at 14ms Figure 49 (b) at 12ms. This delay in displacing the sessile droplet can be interpreted as the cause of more rotation in the detached droplet as offset is increased. By the sessile droplet being accelerated later in the recoiling phase, it is pulled along the surface more abruptly in comparison to a less offset scenario. The section of the merged mass from the impinging droplet is capable or recoiling more before the sessile droplet is displaced as offset is increased. More insight into this phenomenon is presented in the works of Farhangi et al. [88] where the internal velocity fields are validated based on the comparison between experimental and numerical spread diameters and free surfaces. These velocity fields show the sessile droplet begins to move later in the recoiling phase and to have a larger horizontal component as offset was increased.

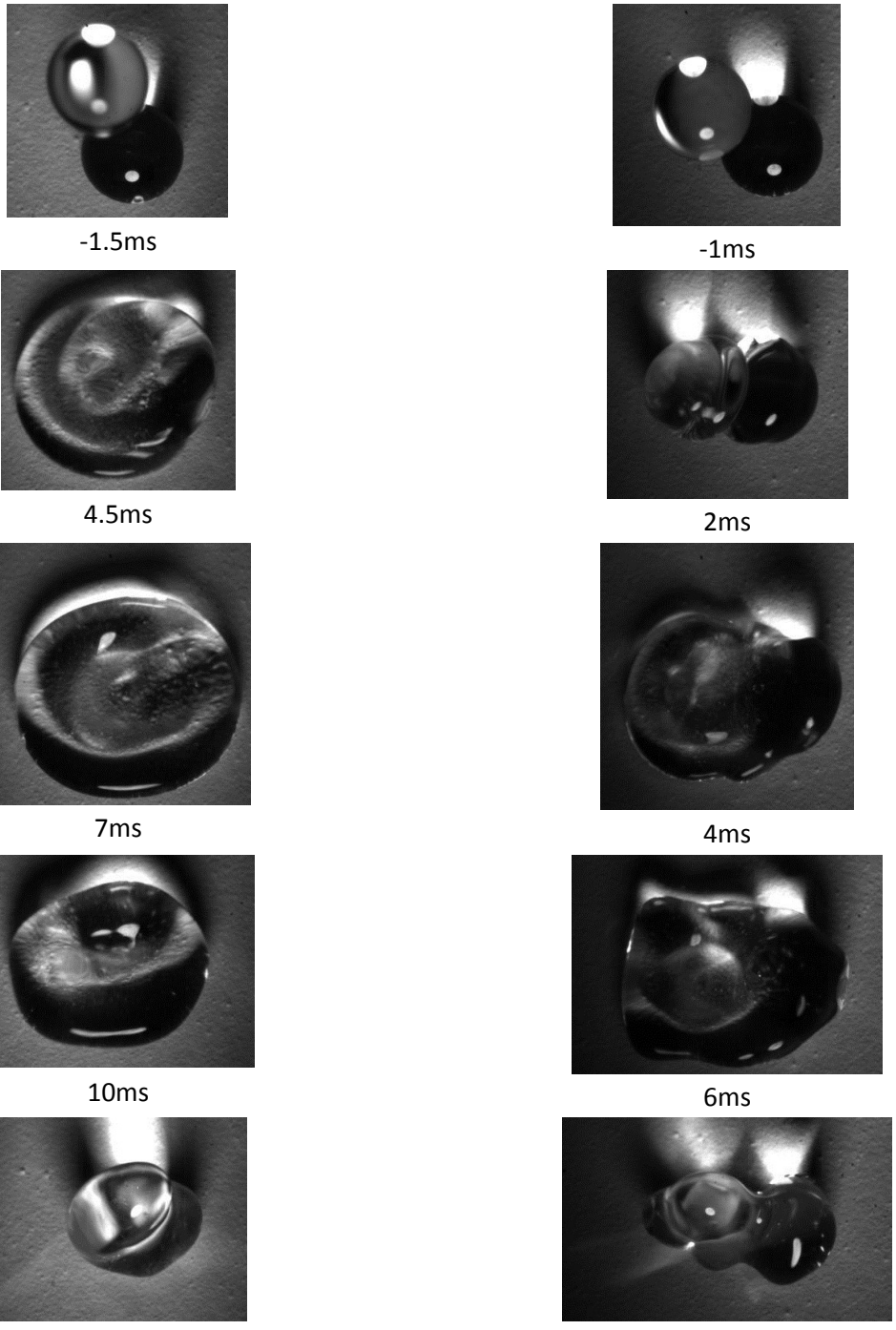

Figure 49: Top/Isometric view of offset detachment Re = 2020, We ≈ 20, (a) λ ≈ 0.4 and (b) λ ≈ 0.8.

Further interpretation of the effect of offset for droplet coalescence and detachment is seen in Figure 50, which depicts the evolution of the spread factor over time for a droplet of Weber number of 19 and Reynolds of 2020 for a head-on, slight offset, moderate offset and large offset, which were already previously presented. Since this section discusses only the effect of offset for superhydrophobic surfaces, non-dimensionalizing spread diameter with both offset and droplet diameter is not needed. As discussed in the previous chapter, Ψ is used to asses the effectiveness of offset and ease comparison between spreading on various surfaces. The first difference to note is the maximum spread diameter is larger for the offset case then the other three, while the slight and moderate offsets (0.41 and 0.77) have a similar maximum spread diameter, which is larger than the maximum spread diameter for the head-on case. After having spread, the droplets then recoil until they detach from the surface. A larger offset is seen to result in a shorter bounce or hanging time, as seen in Figure 50. The largest offset case lands at roughly 35ms, which is only 10ms after detachment. In contrast, the smaller offsets land at 40, 50 and 60ms. The differences between the spreading behaviour of the droplets decreases as time progresses. As was previously discussed, the droplet detaches in a more rotational manner for increasing offset. Since the more offset cases are rotating more, they do not reach the same height as a small offset case; therefore they return to the surface sooner. The large offset has decreased in oscillations substantially when compared to the three less offset cases, which could be attributed to a greater dissipation due to the more elaborate deformations associated with merging while spreading.

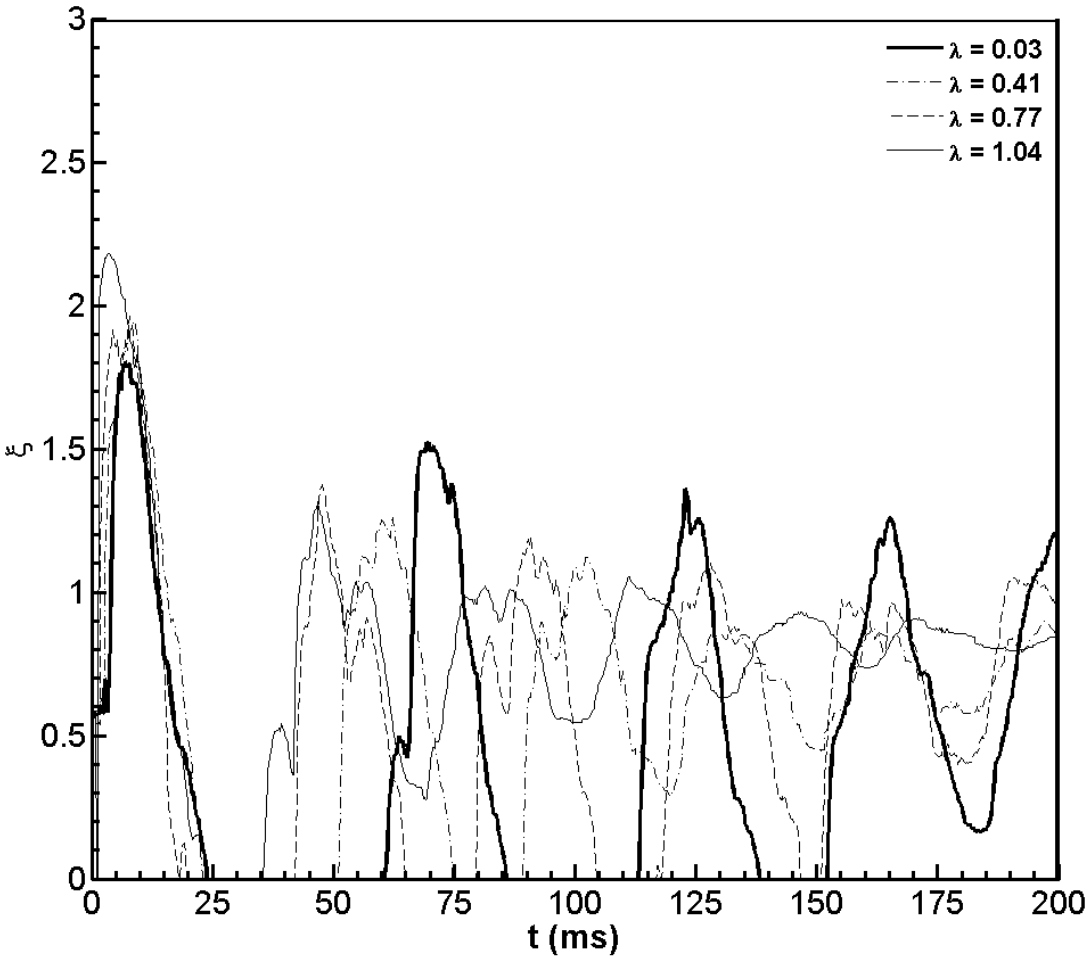

Figure 50: Effect of offset on the spread factor, $\xi = D_y / D_0$, for We = 19, Re = 2020 on superhydrophobic surfaces.

5.3 Restitution coefficient and contact time

In order to quantify the potency of the induced detachment mechanism for various boundary conditions, the contact time and restitution coefficient are measured. The contact time is the time required for the impinging droplet to remove the sessile droplet and the restitution coefficient is the ratio between the vertical component of detached velocity and the impinging droplet's velocity. Similar parameters were used in the works of Chen et al [28]. In light of the discussion in the previous sections of this chapter, the trends observed for contact time and restitution coefficient will be discussed. Figures presented in this section are from the joint numerical and experimental study by Farhangi et al. [94], which is why they include simulation results.

5.3.1 Contact time

The effect of droplet size, impact velocity, and offset between droplets on the contact time is shown in Figure 51 and Figure 52, which show the effect of velocity and offset, respectively. It is noteworthy that the contact time remains mostly constant in response to both velocity and offset. Figure 51 shows the variation of contact time for three distinct droplet sizes (2.3mm, 2.6mm and 3.4mm) for velocities ranging from 600mm/s to 1000mm/s. The graph shows that the droplet velocity has no noticeable effect on the contact time and the dictating parameter is the size of the droplet, i.e. compared to smaller droplets, large droplets require more time to spread and recoil before detaching. This is similar to a harmonic spring, where the natural frequency of the droplet depends on its size and surface tension and not any imposed initial conditions. In such a comparison, the droplet diameter is analogous to the spring itself and the velocity is analogous to the initial conditions imposed. A non-dimensional representation of the effect of offset ratio on contact time is shown in Figure 52. Increasing the separation between the centers of the droplets does not change the dimensionless contact time. In contrast, increasing the Weber number increases the contact time.

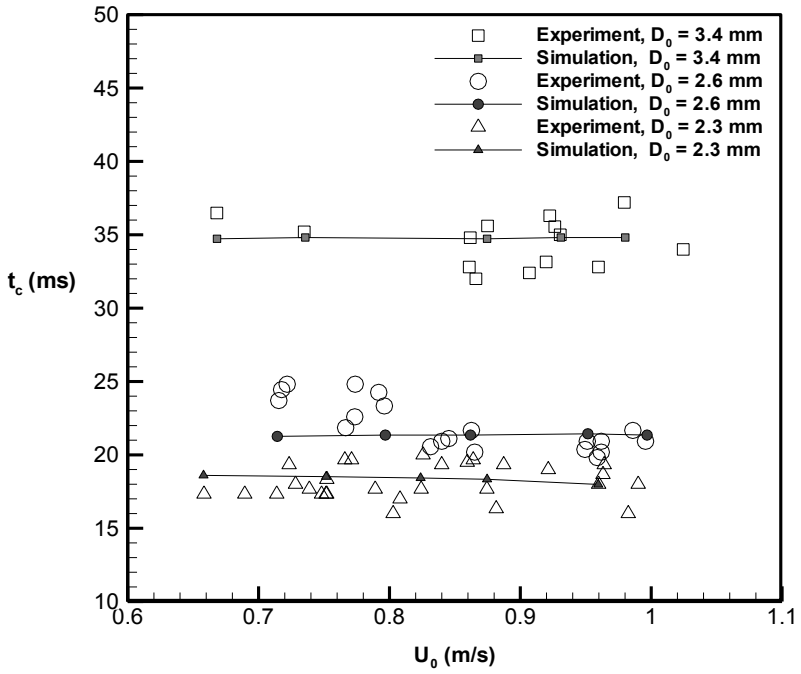

Figure 51. Effect of droplet size and velocity on the contact time, t_c.[(95)].

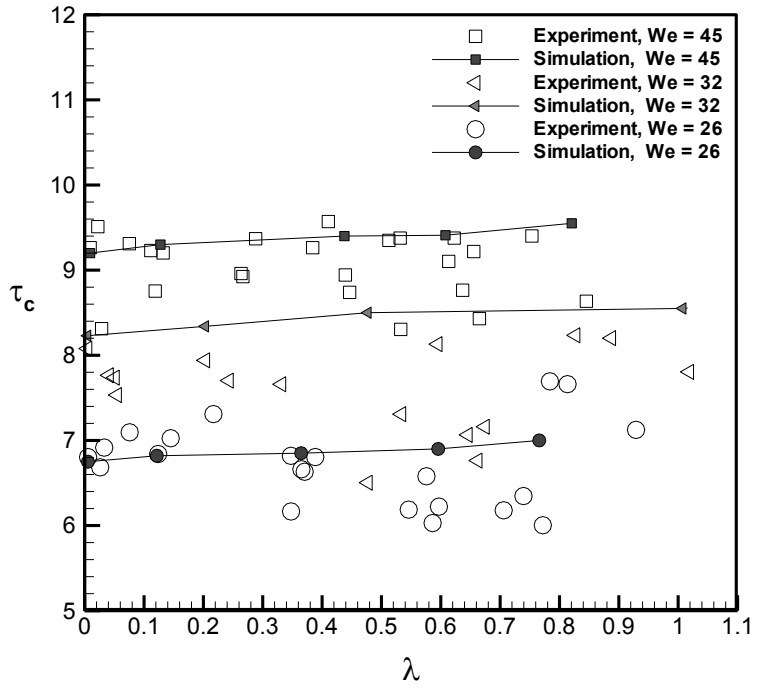

Figure 52. Effect of offset and Weber number on the dimensionless contact time, $\tau_c = (t_c U_0)/D_0$ [(95)].

5.3.2 Restitution coefficient

The restitution coefficient was studied by Chen et al. [28] for the case of a single droplet impinging on a lotus leaf and on an artificially prepared surface, no mention into how the detaching velocity is obtained is present in their works. It is easier to determine the restitution coefficient for the case of a single droplet than for a merging droplet, because there is less deformation of the droplet while it is detaching. Four different methods of determining the detaching velocity were compared. Each of the methods involved tracking a certain point on the droplet, then using linear regression analysis of twenty to thirty frames to determine the detaching velocities of the points of interests. The points studied for each method are: (a) studying the geometric center of the 2D side view; (b) studying the average of the top and bottom velocities of the droplet; (c) inferring a 3D geometry based on the 2D profile and tracking the centroid; and (d) assuming a velocity profile based on the top and bottom and taking a weighted average based on the inferred 3D geometry used when tracking the centroid. The fourth option was found to give the most consistent results. A result was deemed invalid if the standard deviation of the inferred volume was more than 15% of the mean inferred volume.

Similar to the contact time, the restitution coefficient is plotted as a function of impact velocities ranging from 600mm/s to 1000mm/s for 2.3mm, 2.6mm and 3.4mm size droplets in Figure 53. In addition, the effect of offset was presented for three Weber numbers, 19, 26 and 32 for offsets ranging from near head-on to merging by spreading in Figure 53. Increasing either the size or the velocity of the droplets decreases the restitution coefficient. This is attributed to an increase in energy dissipation, which is caused by a greater degree of droplet deformation during the merging spreading and recoiling phase. More deformation is present for larger droplets with higher speeds, as seen throughout this thesis. Similarly, Figure 54 shows that increasing the Weber number decreases the restitution coefficient across all offsets studied. As the overlap ratio increases, the restitution coefficient decreases for the range of Weber numbers studied. Two factors decrease the restitution coefficient; an increase in deformation of the droplet and more rotation of the droplet. The rotation caused by an offset is discussed in Section 5.2.

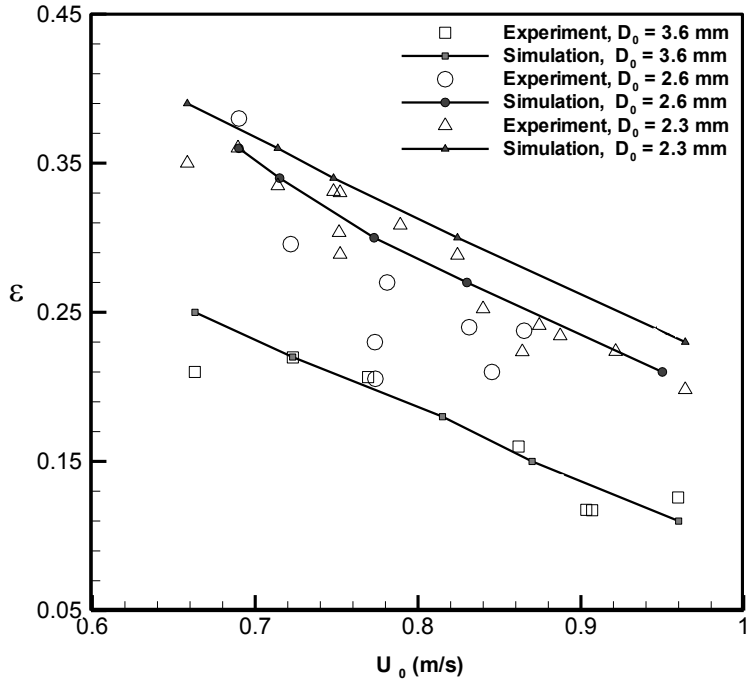

Figure 53: Effect of droplet size and velocity on the restitution coefficient, $\varepsilon = U_d/U_0$ [(94)].

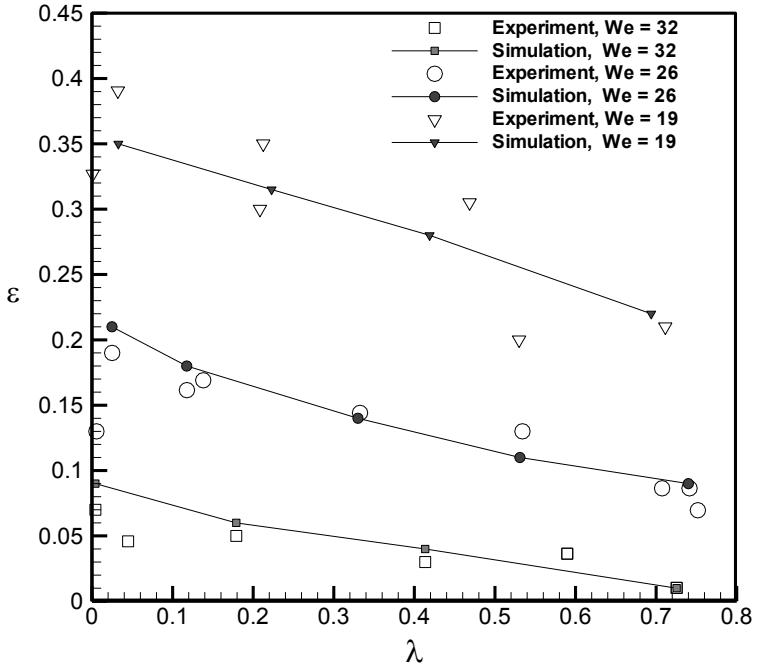

Figure 54. Effect of offset, $\lambda = L/D_0$, and Weber number on the restitution coefficient, $\varepsilon = U_d/U_0$ [(94)].

6 Delayed merging of low weber droplets

The following chapter presents low inertia coalescence, which is characterized by bouncing of the impinging droplet off of the sessile droplet.

As discussed in the introduction, at low Weber numbers, it is possible that droplets do not merge, but appear to bounce off each other, the cause of which is the presence of a layer of air trapped in between the droplets [14), 15)] . Many fascinating works have been done related to droplets bouncing on liquid pools, particularly by Gilet and Bush [78] who observed a droplet bouncing on a soap film similar to an individual jumping on a trampoline. Potentially, these effects may be relevant to air bubble entrapment during coalescence and microfluidic mixing. Such an intervening air layer has a substantial effect on droplet merging dynamics, even if the droplets do not merge, as will be discussed throughout this section. It is important to note that capturing these results with VOF modelling has proven quite difficult due to the small scale of the phenomena.

6.1 Head-on case

For the head-on case, three morphologies are presented, bouncing, merging during recoiling and merging during spreading. The effect of this intervening air layer is seen in Figure 55, which three different Weber numbers, 2, 12 and 19. for a near head-on collision. Droplets are deemed to have merged based on the change in angle between them as seen in instances 9.6ms - 9.8ms for Weber of 12 and 1.7ms – 1.9ms for Weber number of 19, a similar approach was used by Pan et al. [68]

In the case of bouncing (Weber of 2, Figure 55: a), the kinetic energy of the impinging droplet is used to deform both droplets without depleting the intervening air layer. The kinetic energy is transferred to surface tension of the liquid by deviating the shape of both droplets away from their equilibrium shapes. As the droplets deform and spread, which takes roughly 9.4ms, energy is lost due to viscous dissipation and surface tension forces strengthen, since the droplets have deviated from their equilibrium shapes (a spherical droplet and a droplet resting on the surface). Once the inertia has been transferred to surface energy, the droplets begin to recoil in order to return to their original equilibrium shape. Leftover kinetic energy exists in the form of oscillations in the sessile droplet and an upward velocity of the impinging droplet, similar to a spring having been suddenly deformed. The impinging droplet does not return to its original height due to energy lost through viscous dissipation and energy transferred to the sessile droplet. Energy transferred to the sessile droplet is seen in the form of oscillations.

Should the inertia be sufficiently high, the droplets merge while spreading, as seen in Figure 55 (c). The delay in merging is due to the ability of the droplet to force out the intervening air layer. This conclusion is based on the literature studied. The morphology is similar to the discussion present in chapters 3 and 4. In the event that the droplet's oncoming inertia exists between the two previously discussed cases, a delayed merging is possible. The 2nd time series of images in Figure 55 show an intermediate case, with a

Weber number of 12, where the droplets merge during the receding phase. Inertia is transferred to both the surface energy of the liquid and to the solid by causing the spread diameter to increase until surface tension forces cause recoiling of the droplets. As the droplets recoil, the concavity between droplets switches indicating that they have merged at 9.6ms - 9.8ms. The merged droplet then rapidly reaches a substantial height, as seen at 15.6ms and 18.3ms. This large height reached by the droplet can be attributed to potential energy stored by the droplets being in close contact, but not actually merged. Once the air film is sufficiently thin, a neck rapidly grows in between the two droplets, driven by the desire to minimize the surface area to volume ratio.

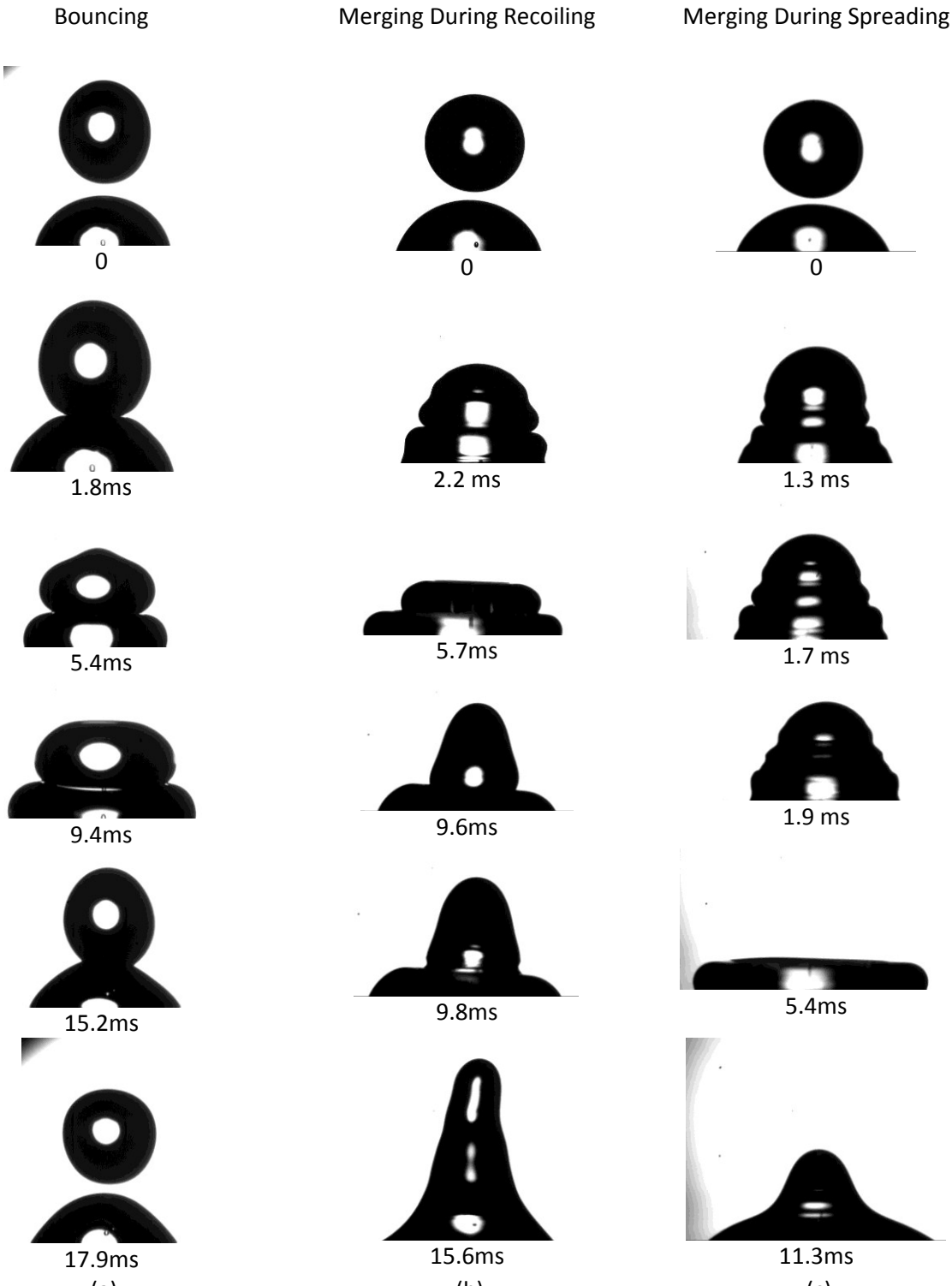

Figure 55: Low Weber number behaviour of head-on impact (a) bouncing for We = 2, (b) merging during recoiling for We = 12 and (c) merging during expansion for We = 19

The temporal evolution of spread diameter, presented in Figure 56, yields more insight into the morphology of the droplets and the dynamics associated with the delayed merging. Chapter 3 discusses the spread diameter for a sufficiently high inertia case, and the temporal evolution of spread factor is repeated in Figure 56 for the reader's convenience. The bouncing case, Weber number of 2, shows a slight increase in spread diameter, then decreases to something comparable to the equilibrium state, the slight increase in spread diameter implies that the potential energy stored is mostly stored as shape change of the droplet rather than an increase in wetted length. Two peaks are shown in the delayed merging case (Weber of 12), one due to the spreading, at 5ms, and a second due to the actual merging, at 27ms, the merged lump then eventually reaches an equilibrium comparable to the high inertia case.

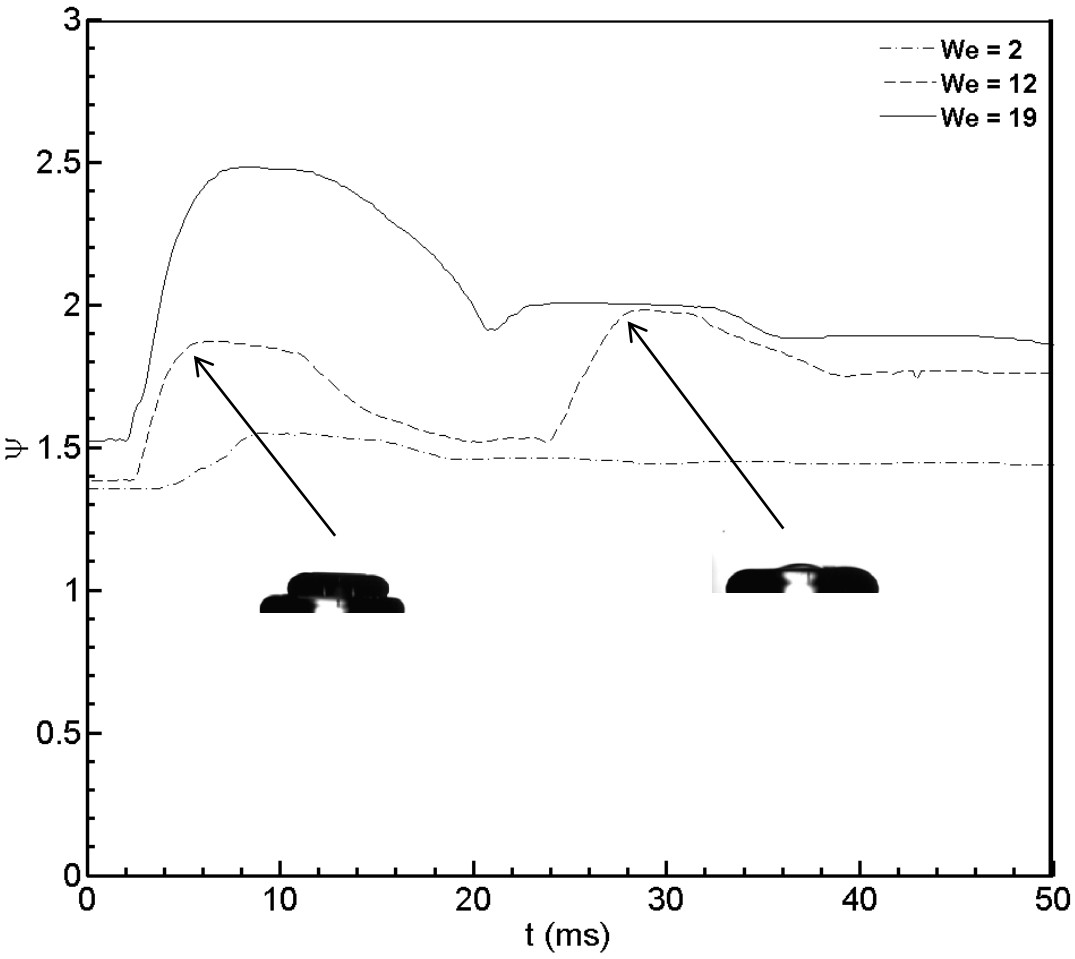

Figure 56: Spread effectiveness, for bouncing, merging during recoiling and merging

The trend for delayed merging is summarized in Figure 57 by presenting the time in which the droplets are in contact without being merged into a single droplet, for merging cases on aluminum. As Weber number increases, dimensionless touching time decreases drastically. This observation implies that a faster droplet is capable of inducing greater airflow speeds around it so that the layer of air can be drained out faster. It is important to note that a precise value at higher Weber numbers would require a much faster recording rate.

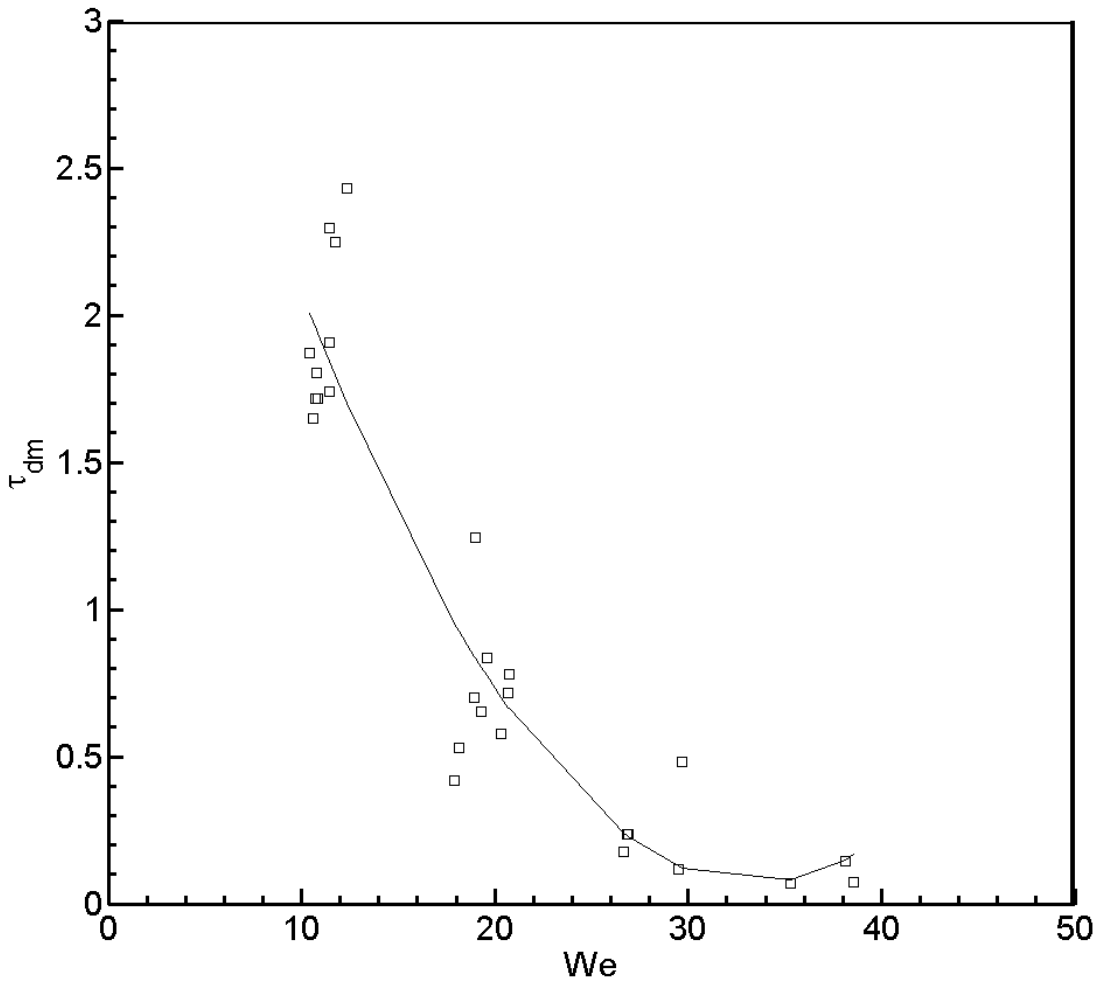

Figure 57: The effect of Weber number on dimensionless delayed merging time, $\tau_{dm} = (t_{dm} D_0)/ U_{0,}$ on a hydrophilic surface

6.2 Effect of offset

Bouncing of water droplets at an dimensionless offsets of 0.1 and 0.4 are presented in Figure 58. The case with the slight offset of 0.1, is similar to the case of head-on merging: the impinging droplet impacts the sessile droplet and its inertia causes both droplet to flatten at 8.5ms. However, the offset causes the impinging droplet to bounce partially laterally as oppose to upwards, as seen at 17.2 ms and 33.3 ms. A larger offsets, of 0.4, results in more horizontal velocity of the droplet once is has bounced, as seen at 15.9ms and 21.7ms. The deformation of the sessile droplet is much more non-symmetric than the case of the smaller offset at 8.2ms; in fact, the impinging droplet has nearly reached the surface. A larger offset causes a less symmetrical deformation, which in turn causes the droplet to bounce sideways as opposed to upwards.

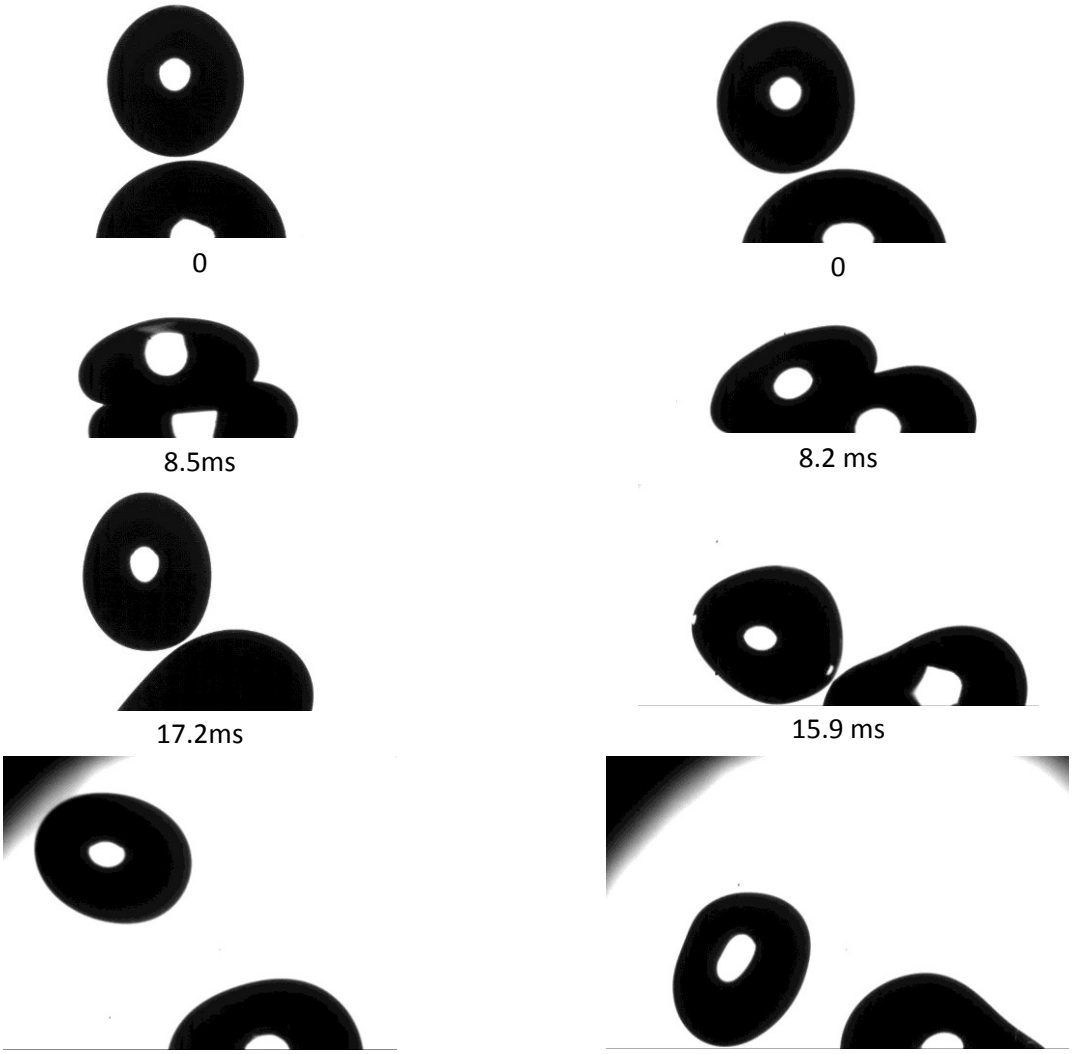

Figure 58: Bouncing Trajectory changes for increasing offsets of (a) λ = 0.1 (b) λ = 0.4, with We = 2.

For an increased offset, the morphology of delayed merging will deviate from what is presented in Figure 55 and Figure 58, as seen in Figure 59. Figure 59 depicts a similar trio of Weber numbers, yet at an offset of roughly one millimeter, in dimensionless terms, 0.4. At this offset, the droplet lands near the contact line. Such a spacing can be seen as the threshold for bouncing, when comparing Figure 59 and Figure 58, which both show a low Weber number collision with a similar offset, since Figure 58 shows bouncing while Figure 59 does not.

The high inertia cases in both Figure 55 and Figure 59 are similar with respect to the discussion related to delayed merging of the current section. For both cases the impinging droplet deforms the sessile droplet and then merges with it. However, the cases of Weber number of 2 and Weber number of 12 present a very different behaviour. For the case of Weber number of 2, the droplet impacts the sessile droplet causing deformation. While deforming, the intervening air layer allows the impacting droplet to slide laterally, until it impacts the substrate at 9.8ms. Shortly after the impinging droplet impacts the substrate, the droplets begin to merge. Once merged, the contact region between the droplets rapidly grows, similar to the case of Weber number of 12 with a head-on impact as seen in Figure 55. The result of the rapid neck growth is seen at 14.4ms, by the protrusion to the left of the droplet.

Intermediate (Weber number of 12) and high (Weber number of 19) inertia cases closely resemble each other. Some sliding is observed, though not as prominent as the case of Weber number of 2. As opposed to the head-on case, a non-dimensional offset of 0.4 causes the droplets merge during spreading as opposed to recoiling, as seen at 5ms. For both Weber number of 12 and Weber number of 20, after merging, a jet is formed at roughly 7.5ms in the center of the impinging droplet. For sufficiently high inertias, Weber number of 19, this jet can cause the ejection of a satellite droplet, seen at 9.26ms, with a velocity much higher than the initial droplet velocity.

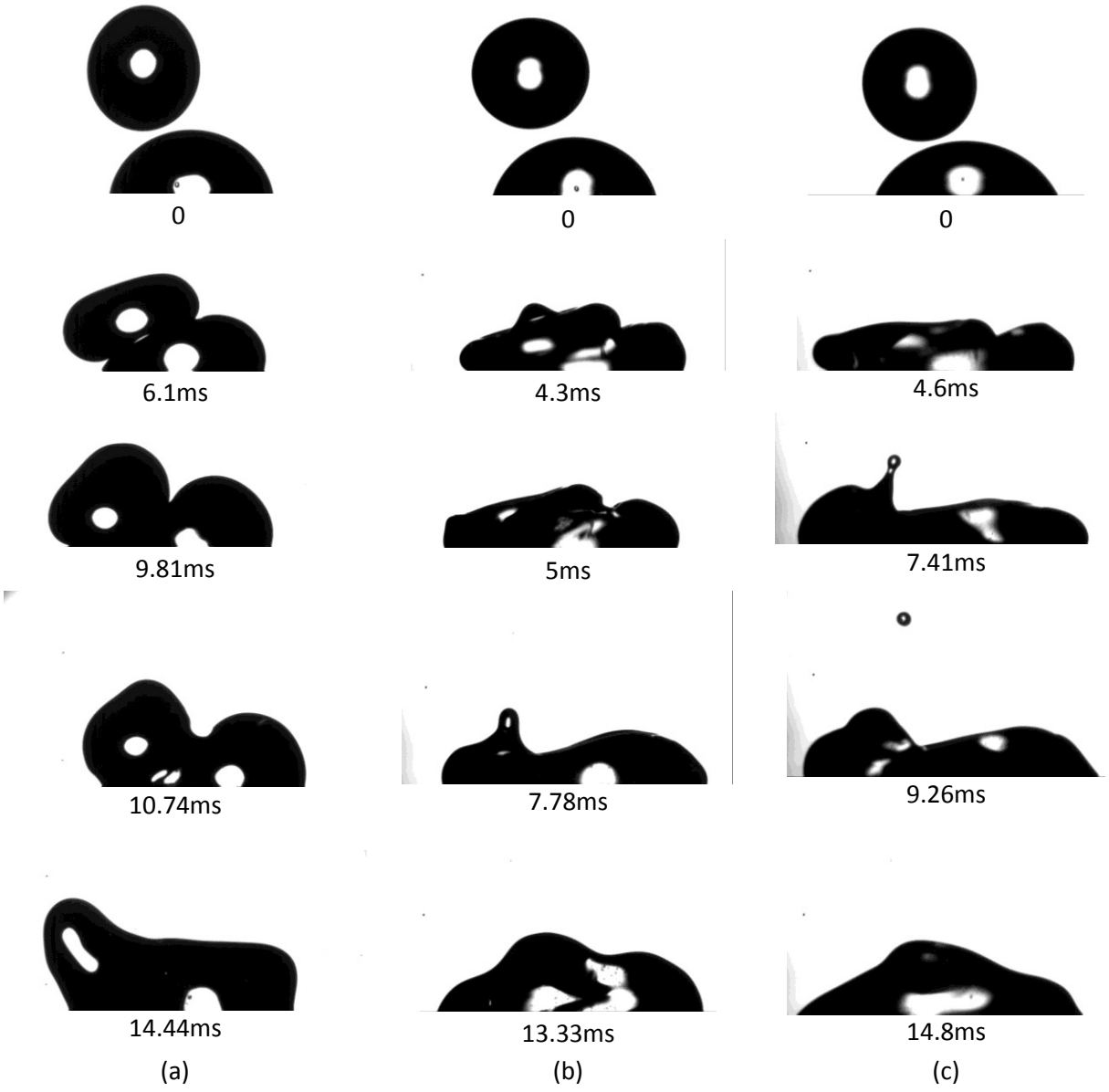

Figure 59: Low Weber number merging for an offset of λ = 0.4,
(a) We = 2, (b) We = 10, (c), We = 20.

More insight into the merging dynamics is supplied by Figure 60, a plot of the wetted length over time. First of all, the three cases more closely resemble each other, as opposed to the trios presented in Figure 55 and Figure 56, which is reasonable since there is no bouncing or merging during recoiling observed. For the lowest Weber number presented, there is a substantial difference between the two higher velocity cases. The difference is caused by the impinging droplet being able to slide along the

sessile droplet and merge into the surface. An abrupt increase in spread diameter is observed at 6.8ms. This sudden change corresponds to the moment where the impinging droplet begins to make contact with the substrate. An abrupt but brief rapid increase is observed for the spread diameter for We = 2 at roughly 7ms in Figure 60. This abrupt increase corresponds to the moment where the sessile droplet has begun to impact the surface, as seen by the leaflet in Figure 60. After the droplets merge at 10ms, the spreading is driven by the neck growth, which can be seen by the leaflets in Figure 60 which correspond to 16 and 18ms. The bulge to the left of the droplet moves to the left and falls, which increases the wetted length.

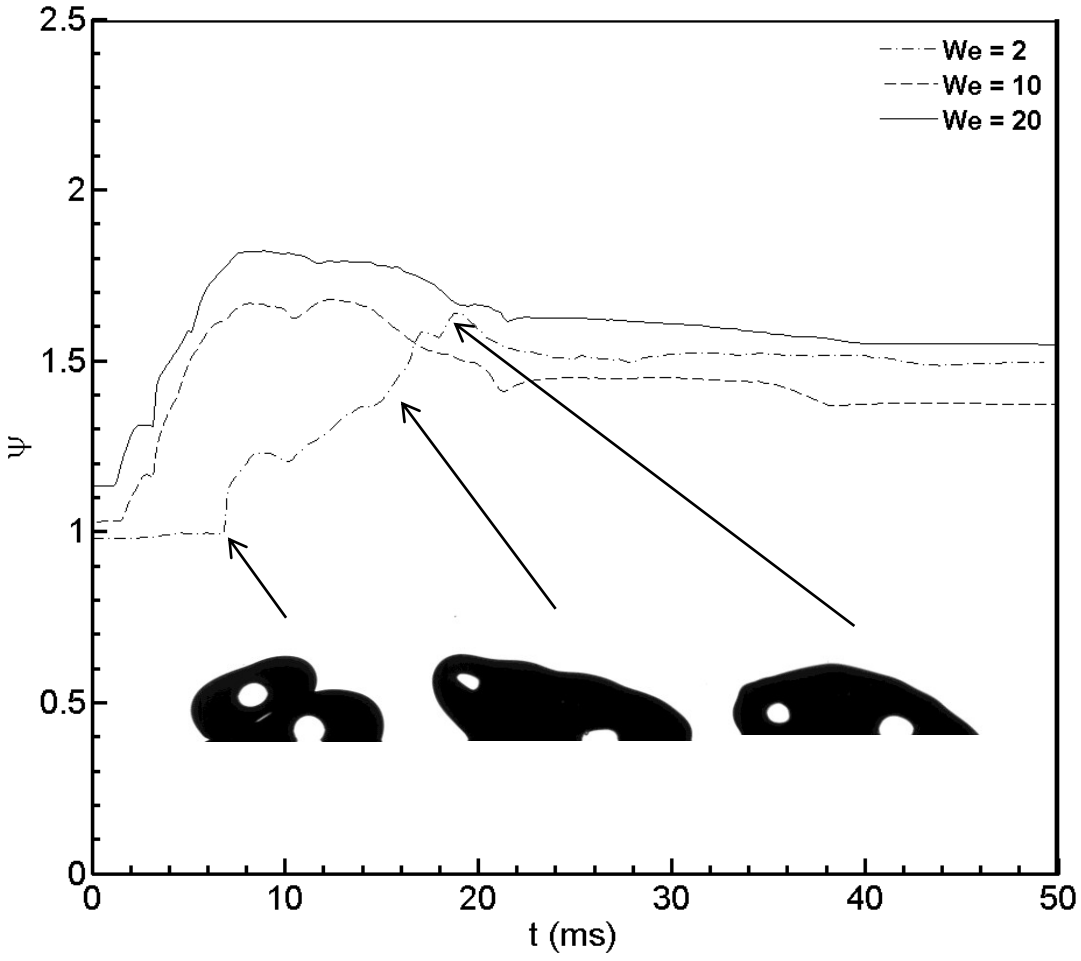

Figure 60: Spread Effectiveness for an offset case of λ = 0.4 on a hydrophilic surface

7 Summary and Conclusions

This work studied the dynamics of droplet coalescence on surfaces wettabilities ranging from hydrophilic, to hydrophobic to superhydrophobic. Motivation for this study is aimed at assessing the effect of substrate wettability on water and ice accumulation, particularly on superhydrophobic surfaces. In literature, a large amount of work has been dedicated to the understanding of a droplet impinging on either a dry substrate or a pool of water. To enhance the understanding supplied by works detailing single droplet impingement, coalescence dynamics were studied. The study of coalescence serves as a building block to improve the understating of droplet sliding, rivulet formation, and film formation. In addition to liquid accumulation issues, coalescence dynamics are encountered in fields such as painting, spray coating, ink-jet printing, spray cooling, to name a few.

- To study the effect of wettability on the coalescence mechanics, five types of surfaces were used. These surfaces include; aluminum which is the standard aerospace building material; Teflon which is a standard commercial hydrophobic material, aluminum coated by a hydrophobic liquid, rough Teflon, and aluminum coated with a superhydrophobic spray. These surfaces had different degrees of mobility and repellency. An experimental rig was designed and manufactured to study the coalescing droplets. This rig has two major components; a droplet generator and a high speed camera. The resulting images were studied using image processing.

- The axisymmetric case of head-on impact was studied. It was found that, increasing wettability and inertia increase the maximum spreading of the coalesced droplets. By studying experimental results, head-on impact can be divided into two phases, a bulging phase and a spreading phase. The bulging time period was roughly R_0/U_0 and the total time scaled universally with maximum spread diameter and velocity. An analytical model was developed, by taking advantage of the commonality noticed. This model was based on conservation of energy and, despite its simplicity, captured the maximum spread diameter with a good degree of accuracy (≈ 20 %).

- Due to the increased complexity associated with offset impact, a regression model which captures the effect of wettability, offset, droplet size and droplet speed was developed based on all experimental data. The novel feature of this model is the use of a proposed surface Weber number, which is the ratio between inertia and substrate wettability.

- By thoroughly examining the time evolution of coalescing droplets on the five surfaces of distinct wettability, it was found that the receding contact angle dictates the recoiling process. As the receding angle increases, the shape reached during the receding changes drastically and the minimum spreading length decreases and the height reached by the droplet increase substantially. Droplets on surfaces with a receding angle greater than 90° recoiled much more easily than aluminum and Teflon, especially at large offsets.

- In the event that a droplet is resting on a superhydrophobic surface, a surface with a large receding angle, it is possible for the sessile droplet to be removed by an incoming droplet even at large offsets. Such a potent mechanism to inhibit water accumulation was not observed for the other surfaces, even for the very hydrophobic surfaces, with contact angles up to 135°. Understanding of this mechanism is important since it contributes to the understanding of how superhydrophobic surfaces are highly water repellant, particularly when being exposed to clouds or sprays. In a cloud or spray, droplets which may have adhered to the surface, could be removed by other droplets.

- The effectiveness of the droplet being removed was studied based on the contact time and restitution coefficient. It was found that the time required to remove the droplet is independent of spacing and velocity, but dependent on diameter. The restitution coefficient was found to decrease as offset, velocity and droplet size are increased. This decrease was attributed to two causes, more dissipation due to more deformation; and an increase in angular momentum at the expense of linear momentum of the detached droplet.

- Due to this detachment, the formation of films and rivulets is highly unlikely, or at least greatly impeded. Furthermore, coating, painting and ink-jet printing are nearly impossible when a surface has a high mobility.

- As impact velocity is decreased, an air film remains between droplets; causing merging during recoiling or bouncing. This interference in coalescence can impact the evolution of spread length substantially.

8 Potential future works

Should the reader be interested in future experimentation and study of coalescing droplets there are a variety of manner they can do so. The simple next step would be repeating the experiments with different water-glycerin mixtures in order to determine the effect of viscosity. Another similar step would be studying oleophilic and oleophobic surfaces and deposit various hydrocarbons. Such a study may be interesting for combustion applications. The analytical model may be improved by refining the merging and spreading time. In addition, one could study the critical spacing for merging and induced bouncing, as will be discussed in detail.

8.1 Critical spacing for merging

At substantially large offsets, droplets may or may not merge. Intuitively, the threshold for the droplets to merge depends on the maximum spreading diameter of the impinging droplet. At such a threshold, the velocity of the contact line is low and surface forces can play a substantial role. Figure 61, shows three cases of a droplet with Weber number of 19 and Reynolds number of 2200 impinging at an offset corresponding to $\lambda = 1.7$, which is the critical spacing for merging. Three distinct behaviours are noticed, a direct merge, and indirect merge and no merge. For all cases, the droplets interact with each other, as see at 0.7ms. The slightly difference offsets or velocities cause the growth of the neck to behave substantially differently. For the two cases of merging the neck may grow rapidly or slowly, as seen by the images from 0.7ms to 2.6ms. The intermediate merging case shows a decrease in neck height, and begins to recoil at 2.04ms, before a rapid increase in neck height at 2.6ms. In contrast the neck height grows from 0.7ms to 2.6ms as the droplets merged, for the case of direct merging. The differences in neck growth cause a vastly different profile, as seen at 8.9ms. At 3.5ms, the case of non-merging, the neck has begun to shrink until it is broken at 4.4ms. The air flow induced by the droplets can be a potential cause of this phenomenon.

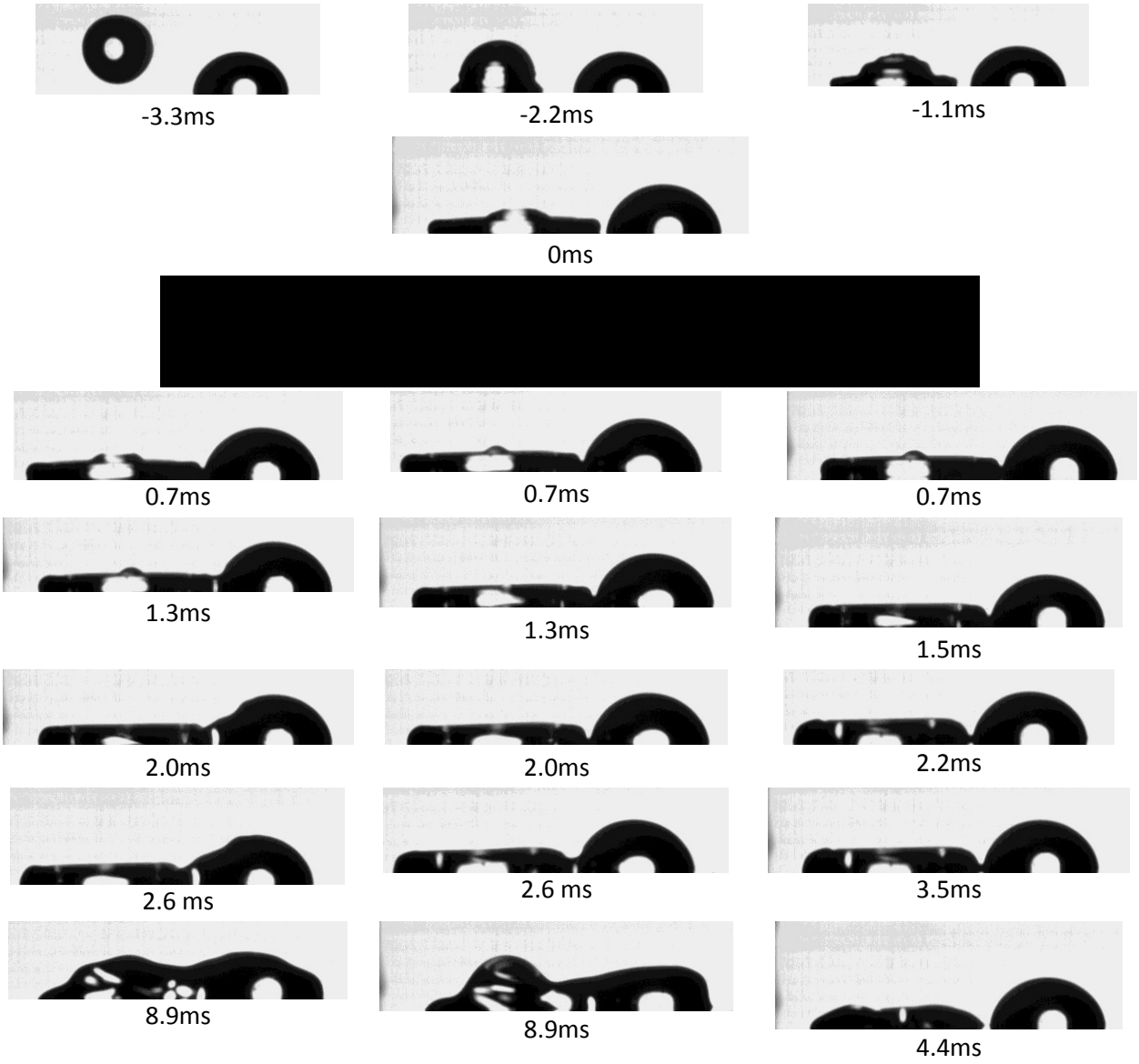

Figure 61: Behaviour at critical offset for merging (a) Direct Merge, (b) Delayed Merge, (c) No Merge

8.2 Behaviours induced during non-coalescence of droplets on superhydrophobic surfaces

Cases of non-coalescence on superhydrophobic surfaces can arise due to low impact velocity as discussed in Chapter 4 or due to offset as discussed in the Section 8.1. In terms of low impact inertia, bouncing can be induced in the sessile droplet. Figure 62 shows induced bouncing for a head-on case and an offset case ($\lambda \approx 0.20$) for Weber number of 3. The offset is seen to cause the droplets to bounce

horizontally as opposed to mostly vertically as seen at times 23.1ms for the head on case and 18.5ms for the offset case. During the merging, both droplets take on flattened independent shapes at 3.7ms, similar to what was shown in Chapter 4 in Figure 55 and Figure 58. The difference among the cases is the non-symmetrical shape taken by the offset case. Figure 63 shows a case of induced oscillations: a droplet impacts the surface, spreads into the droplet and does not merge with it, then bounces off of the surface, as a results of the impact the sessile droplet oscillates on the surface.

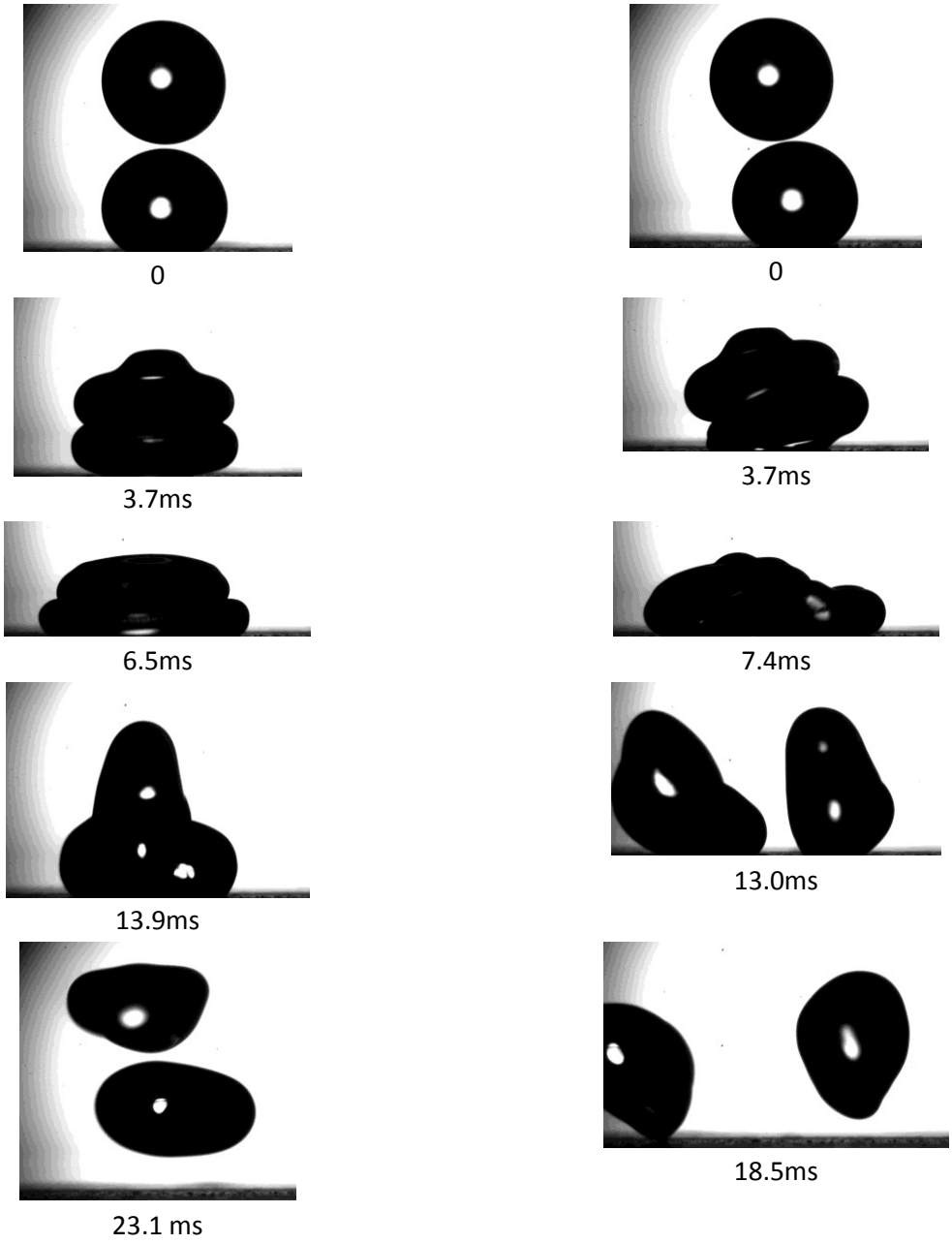

Figure 62: Induced Bouncing on superhydrophobic surfaces, with We ≈ 3

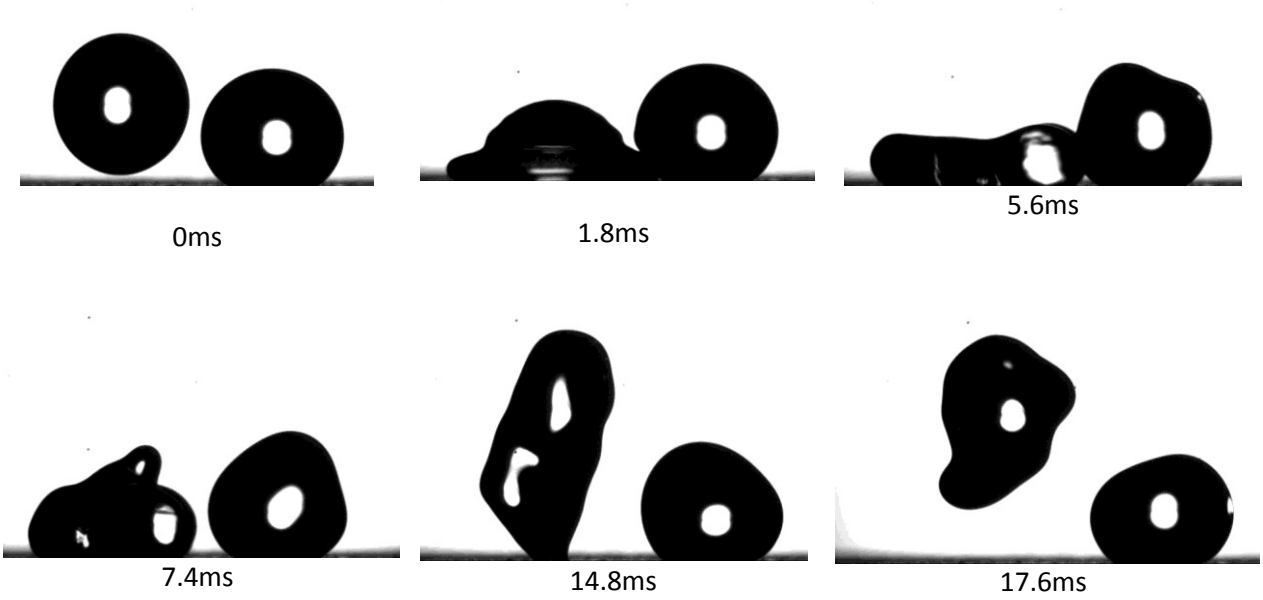

Figure 63: Induced Oscillations of the sessile droplet, Re = 2020, We = 19 and λ = 1.1

9 Works Cited

1. **Worthington, Arthur Mason.** *The Splash of A Drop.* London : Society for promoting christian knowledge, 1895.

2. **Worthington.** *A study of Splashed.* Davenport : The Royal Naval Engineering College, 1908.

3. *Droplet Splashing by a Slingshot Mechanism.* **Thoroddsen, S. T., et al., et al.** s.l. : Physical Review Letter, 2011.

4. *On the errors associated with the use of hourly data in wind-driven rain calculations on building fascades.* **Blocken, Bert and Carmeliet, Jan.** Leuven : Elsevier, 2006.

5. *The kinetic energy of rain measured with an optical disdrometer: An application to splash erosion.* **Fernandez-Raga, Maria, et al., et al.** s.l. : Atmoshperic Research, 2010.

6. *Limits to the feature size and resolution in ink jet printing.* **Derby, B. and Stringer, J.** s.l. : Journal of the European Ceramic Society, 2009.

7. *Inkjet-Printed Line Morphologies and Temperature Control of the Coffee Ring Effect.* **Soltman, Dan and Subramanian, Vivek.** s.l. : Langmuir, 2008, Vol. 24.

8. *Coalescing of two droplets impacting a solid surface.* **Li, Ri, et al., et al.** s.l. : Experiments in fluids, 2010.

9. *Drawback During Depostion of Overlapping Molten Wax Droplets.* **Li, Ri, et al., et al.** s.l. : Journal of Manufacturing Science and Engineering, 2008, Vol. 130.

10. *Freezing-induced splashing during impact of molten metal droplets with high Weber numbers.* **Dhiman, Rajeev and Chandra, Sanjeev.** Toronto, Ontario : International Journal of Heat and Mass Transfer, 2005, Vol. 48.

11. *Splashing of molten tin droplets on a rough steel surface.* **Shakeri, Saeid and Chandra, Sanjeev.** Toronto, Ontario : International Journal of Heat and Mass Transfer, 2002, Vol. 45.

12. *Spreading and solidification of a moleten metal droplet impinging on a heated surface.* **Sivakumar, D and Nishiyama, H,.** Sendai, Japan : International Jounral of Heat and Mass Transfer, 2004, Vol. 47.

13. *Impact, recoiling and splashing of molten metal droplets.* **Aziz, Shiraz D. and Chandra, Sanjeev.** Toronto, Ontario : International Journal of Heat and Mass transfer, 1999.

14. *An experimental investigation on the collion behavoiur of hydrocarbons.* **Jiang, Y. J., Umemura, A. and Law, C. K.** Princeton, New Jersey : Journal of Fluid Mechanics, 1992.

15. *An analysis of head-on droplet collision with a large deformation in gaseous medium.* **Zhang and Law.** Princeton, New Jersey : Physics of Fluids, 2011.

16. *Experimental investigation of dynamic binary collision of ethanol droplets - a model for droplet coalescence and bouncing.* **Estrade, J.P., et al., et al.** s.l. : International Journal of Heat and Fluid Flow, 1999, Vol. 20.

17. *Regimes of coalescence and separation in droplet collision.* **Qian, J. and Law, C. K.** Princeton, New jersey : Journal of Fluid Mechanics, 1997, Vol. 331.

18. *Single droplet impacts onto deposited drops. Numerical analysis and comparaison.* **Nikopolous, Nikos, et al., et al.** s.l. : Atomization and Sprays, 2010, Vol. 20.

19. **Dolatabadi, Ali, et al., et al.** *Ice-phobic evaluation of super-hydrophobic coatings for aircaft icing protection.* Montreal : PWC, 2010.

20. **Czernkovich, Nick.** *Understand In-Flight Icing.* s.l. : Transport Canada Aviation Safety Seminar , 2004.

21. *Inflight Icing* . **Weener, Earl F.** Montreal : National Transport Safety Board, 2011.

22. *Dynamic Wetting on superhydrophobic surfaces: Droplet Impact and wetting hysteresis.* **Smyth, Katherine, et al., et al.** Cambridge, Massachusetts : IEEE, 2010.

23. *Model and experimental studies for contact angles of surfactant solutions on rough and smooth hydrophobic surfaces.* **Amirfazli, A, Milne and Elliot.** s.l. : Physical Chemistry, 2011.

24. *Understaing of sliding and contact angle results in tilted plate experiments.* **Pierce, E, carmona, F J and Amirfazli, A.** s.l. : Colloids, 2008.

25. *Surfaces with self-repairable ultrahydrophobicity based on self-organizing freely floating colloidal particles.* **Puretskiy, Nikolay, et al., et al.** s.l. : Langmuir, 2012.

26. [Online] Cytonix. [Cited: May 30, 2012.] http:/www.cytonix.com/classic/fluorothane.html.

27. **Toto.** Super-hydrophylic Photocatalysts and its applications. [Online] [Cited: May 1, 2012.] http://www.toto.co.jp/hydro_e/hydro_e2.htm.

28. *A comparative study of droplet impact dynamics on a dual-scaled superhydrophobic surface and lotus leafe.* **Chen, Longquan, et al., et al.** Hong Kong : Applied Surface Science, 2011.

29. *Surface Phenomena: Contact Time of a Bouncing Drop.* **Richard, D, Clanet, C and Quéré.** s.l. : Nature, 2002.

30. *Bouncing Water Drops.* **Richard, D and Quéré, D.** s.l. : Europhysics Letters, 2000.

31. *Bouncing transistion on Micrtextured Materials.* **Reyssat, M, et al., et al.** s.l. : Europhysics Letters, 2006.

32. *Surface free energy of a solid from contact angle hysteresis.* **Chibowski, Emil.** s.l. : Advances in Colloid and Interface sciences, 2003.

33. *Rough Ideas on Wetting.* **Quéré, D.** s.l. : Physica A, 2002.

34. *An Essay on the Cohesion of Fluids.* **Young.** s.l. : Transaction of the Royal Society of London, 1805.

35. *Superhydrophobic Polyolefin Surfaces: Controlled Micro- and NanoStrucytes.* **Puukilainen, Esa, et al., et al.** Joensuu, Finland : Langmuir, 2007.

36. *Impact of chaing length, temperature, and humidity of the growth of long alkylthichlorosilane self-assembled monolayers.* **Desbief, S, et al., et al.** s.l. : Physical Chemistry, 2011.

37. *The impact of Solution Agglomeration on the Dropsition of Welf-Assemlbed Monolayers.* **Burker, et al., et al.** Albuquerque, New Mexico : Langmuir, 2000.

38. *How Cassie and Wenzel were Wrong.* **Gao and McCarthy.** Amherst, Massachusets : Langmuir, 2007.

39. *The Cassie Equation: How it is meant to be used.* **Milne and Amirfazli.** s.l. : Advances in Colloids and Interface Science, 2012.

40. *The rigorous derivation of Young, Cassie-Baxter and Wenzel Equations and the analysis of the contact angle hysteresis pehnomenon.* **Whynman, G., Bormaschenko, E. and Stein, T.** s.l. : Chemical Physics Letters, 2008.

41. *Wetting Transition Characteristics on Microstructured Hydrohpobic Surfaces.* **Lee, Jae Bong, et al., et al.** 9, Seoul, Korea : Materials Transactions, 2010, Vol. 51.

42. *Contact angle, wettability and adhesion.* **Johnson, R E and Dettre, R. H.** s.l. : Advanced Chemistry, 1964.

43. *Evaporation-Triggered Wetting transition for Water Droplets upon Hydrophobic Microstructures.* **Tsai, Peichun, et al., et al.**

44. *Transition between Superhydrophobic States on Rough Surfaces.* **Patankar, Neelesh A.** Evanston, Illinois : Langmuir, 2004.

45. *Wetting transition of water droplets on superhydrohpboc patterned surfaces.* **Jung, Yong chae and Bhushan, Bhara.** Columbus, Ohio : Elsevier, 2007.

46. *Natural and bimomimetic artifical surfaces for superhydrophobicity, self-cleaning, low adhesion and drag reduction.* **Bhushan, Bharat and Jung, Yong Chae.** Columbus, Ohio : Progress in Materials Science, 2008.

47. *Interfacial propulsion by directional adhsesion.* **Prakash, M. and Bush, J.** s.l. : International Jounral of Non-Linear Mechanics, 2011, Vol. 46.

48. *Mimicking the Lotus Effect: Influence of Double Roughness Structures and slender Pillars.* **Patankar, Neelesh A.** Evanston, Illinois : s.n.

49. *Drop Impact Dynamics: Splashing, Spreading, Receding, Bouncing ...* **Yarin, A. L.** Haifa, Israel : The Annual Review of Fluid Mechanics, 2006.

50. *Outcomes from a Drop Impact on Solid Surfaces.* **Rioboo, R, Tropea, C. and Mareng, M.** s.l. : Atomization and Sprays, 2011.

51. *Time evolution of liquid drop impact onto solid dry surfaces.* **Rioboo, R., Marengo, M. and Tropea, C.** s.l. : Experiments in fluids, 2002.

52. *High-speed photography of surface geometry effects in liquid/solid impact.* **Dear, J. P. and Field, J. E.** 1987.

53. *On the Collision of a Droplet with a Solid Surface.* **Chandra, Sanjeev and Avedisian, C.T.** s.l. : The Royal Society, 1991.

54. *Normal impact of a liquid drop on a dry surface: model for spreading and receding.* **Roisman, Ilia, Rioboo, Romain and Tropea, Cameron.** s.l. : The Royal Society, 2002.

55. *Capillary effects during droplet impact on a solid surface.* **Pasandideh-Fard, M., et al., et al.** Toronto, Ontario : American Institute of Physcics, 1996.

56. *Energy transition in superhydrophobicity: low adehesion, easy flow and bouncing.* **Nosonovksy, Michael and Bhusan, Bharat.** s.l. : Jounral of Physics: Condensed Matter, 2008.

57. *Generation and breakup of Worthington jets after cavity collpase. part1. jet formation.* **Gekle, Stephan and Gordillo, J. M.** s.l. : Journal of Fluid Mechanics, 2010.

58. *Nonwetting of impinging droplets on textured surfaces.* **Deng, Tao, et al., et al.** Cambridge, Massachussets : Applied Physics Letters, 2009.

59. *Cassie-Wenzel and Wenzel-Cassie transition on immeresed superhydrophobic surfaces under hydrostatic pressure.* **Forsberg, Pontus, Nikolajeff, Fredrik and Karlsson, Mikael.** s.l. : Soft Matter, 2011.

60. *Characterization of ultrhydrophobic hierachical surfaces fabricated using a single-step fabrication methodolody.* **Dash, S., Kumari, N. and Garimella, S. V.** s.l. : Journal of Micromechanics and Microengineering, 2011.

61. *Dynamic contact angle of spreading dropelts: Experiments and simulations.* **Sikalo, S, et al., et al.** s.l. : Physics of Fluids, 2005.

62. *The recoling of liquid droplets upon collision with solid surfaces.* **Kim and Chum.** s.l. : Physics of Fluids, 2001.

63. *On The Maximum Spreading Diameter of Impacting Droplets on Well-Prepared Solid Surfaces.* **Ukiwe, Chijoke and Kwok, Daniel Y.** s.l. : Langmuir, 2005.

64. *Dynamic contact angle effects onto the maximum drop impact spreading on solid surfaces.* **Vadillo, D. C., et al., et al.** s.l. : Physics of Fluids, 2009.

65. *Maximal deformation of an impacting drop.* **Clanet, Christophe, et al., et al.** s.l. : Journal of Fluid Mechanics, 2004, Vol. 517.

66. *Dynamics of Intertia Dominated Binary Drop Collisions.* **Roismann, I.** s.l. : Physics of Fluids, 2004.

67. *The stability of ink-jet printed lines of liquid with zero receding contact angle on a homogeneous substrate.* **Duineveld, P. C.** s.l. : Journal of Fluid Mechanics, 2003.

68. *Experimental and mechanistic description of merging and bouncing in head-on binary droplet collision.* **Pan, Kuo-lang, Law, Chung K. and Zhou, Biao.** s.l. : Journal of applied physics, 2008.

69. *Lifetime of a bouncing droplet.* **Terwagne, D., Vandewalle, N and Dorbolo, S.** s.l. : Physical Review, 2007.

70. *From Bouncing to Floating: Noncoalescence of Drops on a Fluid Bath.* **Counder, Y., et al., et al.** s.l. : Physical Review Letters, 2005.

71. *Modeling the coalescence of sessile droplet.* **Sellier, M. and Trelluyer, E.** s.l. : Biomicrofluidics, 2009.

72. *Morphology and dynamics of droplet coalescnce on a surface.* **Kapur, N. and Gaskell, P. H.** s.l. : Physical review, 2007.

73. *Coalescnce of liquid drops by surface tension.* **Menchaca-Rocha, A., et al., et al.** s.l. : Physical Review, 2001.

74. *The coalescence speed of a pendant and a sessile drop.* **Thoroddsen, S. T., Takehara, K. and Etoh, T. G.** s.l. : Journal of Fluid Mechanics, 2005.

75. *Coalescnce of Spreading Droplets on a Wettable Substrate.* **Ristenpart, W. D., et al., et al.** s.l. : Physical Review Letter, 2006.

76. *Self-Propelled Dropwise Condensate on Superhydrophobic Surfaces.* **Boreyko, J. B, and Chen, C. H.** s.l. : Physical Review Letter, 2009.

77. *Precise deposition of molten micrdrops: the physics of digital microfabrication.* **Gao, F. and Sonin, A. A.** s.l. : Royal Society of London, 1994.

78. *The fluid trampoline: droplets bouncing on a soap film.* **Gilet, Tristan and Bush, John.** s.l. : Journal of Fluid Mechanics, 2009, Vol. 625.

79. *Metastable bouncing droplets.* **Terwagne, D, et al., et al.** s.l. : Physics of Fluids, 2009.

80. *Air cushioning in droplet impacts with liquid layers and other droplets.* **Hicks, Peter D. and Purvis, Richard.** s.l. : Physics of Fluids, 2011, Vol. 23.

81. *The head-on colliding process of binary liquid droplets at low velocity: High-speed photography experiments and modeling.* **Wang, Feng-Chao, Feng, Jiang-Tao and Zhao, Ya-Pu.** Beijing : Journal of Colloid and Interface Science, 2008, Vol. 326.

82. *Multiple Drop Impact onto a Dry Solid Substrate.* **Roisman, et al., et al.** s.l. : Journal of Colloids, 2002.

83. *Bouncing, Coalescwnce and Separation in Head-on Collision of Unequal-size Droplets.* **Tang, Zhang and Law.** s.l. : US National Combustion Meeting, 2011.

84. *FASTCAM SA1.1 Hardware Manual.* Tokyo, Japan : Photron Limited, 2007. E0706013518U.

85. **Navitar.** *Zoom 6000, High Mag Zoom Lens.* Meudon, France : Laser Components.

86. F-Number. [Online] [Cited: July 12, 2012.] http://www.photography.com/articles/basic-concepts/f-number/.

87. Nikon Miscroscopy. *Numerical Aperture.* [Online] [Cited: July 11, 2012.] http://www.microscopyu.com/articles/formulas/formulasna.html.

88. **Schott Norht America.** *LLS - LED Light Source.* Southbridge, USA : s.n., 2009.

89. **Faulkner, Mike.** Email Correspondance. s.l. : Bock Optronics, 2011.

90. **Mcmaster Carr.** Technical Help Correspondance, Email, June 11 2012.

91. **Jensen, Cecil, Helsel, Jay and Short, Dennis.** Surface Texture. *Engineering Drawing adn Design, Sixth Edition.* Peoria, Illinois : McGraw-Hill, 2002.

92. *A novel and inexpensive technique for creating superhydrophobic surfaes using Teflon and sandpaper.* **Nilsson, Michael A, Daniello, Robert J and Rothstein, Jonathan P.** Amherst, Massachusetts : Journal of Physics D: Applied Physics, 2010, Vol. 43.

93. *Transition of super-hydrophobic states on droplet on rough surface.* **Xia, Ye, et al., et al.** s.l. : Jounral of Central South University, 2010.

94. *Induced Detachment of Coalescing Droplet on Superhydrophobic Surfaces.* **Farhangi, M. Mehran, et al., et al.** Montreal, Qc : Langmuir, 2012.

95. *Dynamics of droplet coalescence in response to increasing hydrophobicity.* **Farhangi, Mehran M., Graham, Percival J. and Dolatabadi, Ali.** Montreal : Submitted to Physics of Fluids, 2012.

96. *Superhydrophobicity of Natural and Artificial Surfaces Under Controled Condensation Conditions.* **Yin, L, et al., et al.** s.l. : ACS Apllied Material Interfaces, 2011, Vol. 4.

97. *Superhydrophobicity of Biological and Technical Surfaces Under Moisture Condenstion: Stability in Relation to Surface Structure.* **Mockenhaupt, B., et al., et al.** s.l. : Langmuir, 2008, Vol. 24.

98. *Sessile-Water-Droplet Contact Angle Dependence on Adsoption at the Solid-Liquid Interface.* **Ghasemi, H and Ward, Charles A.** Toronto, Ontario : Journal of Physical Chemistry, 2010, Vol. 114.